Non-linear sensitivity of a CubeSat's orbital motion to an asteroid's rotational state uncertainties using Non-Intrusive Polynomial Chaos

Maarten van Nistelrooij

Technische Universiteit Delft - University of Strathclyde Glasgow

TU Delft

University of Strathclyde Glasgow

Non-linear sensitivity of a CubeSat's orbital motion to an asteroid's rotational state uncertainties using Non-Intrusive Polynomial Chaos

by

Maarten van Nistelrooij

in partial fulfilment of the requirements to obtain the

Master of Science in Aerospace Engineering

at Delft University of Technology

Student number:	4548671	
Project duration:	July 2022 - June 2023	
Thesis committee:	Dr. ir. E. Mooij	Committee chair
	Dr. ir. D. Dirkx	TU Delft daily supervisor
	Dr. J. Feng	University of Strathclyde daily supervisor
	Dr. A. Menicucci	External examinator
	Ir. M.S. Fayolle	Additional examinator

The cover picture is an artist impression of a CubeSat near a small solar system body. Image credit: European Space Agency

Preface

This M.Sc. thesis concludes the past seven years that I have studied at Delft University of Technology. It was an extraordinary experience and I want to thank everyone who made it possible!

Specifically, I want to thank Dominic, for your guidance throughout this project. Thank you for your constructive criticisms, useful suggestions and for always being positive in life!

I also want to thank Jinglang and Iosto, for having me over in Glasgow to work on this project with you. You taught me the ins and outs of small body missions and uncertainty analysis, which has really helped me shape this research. Also thank you to the ACE community, for making me feel at home and making it a fun time in Glasgow!

Finally, I want to thank my family and friends for their unconditional support!

Maarten van Nistelrooij
Delft, May 2023

Abstract / Summary

Small solar system bodies have received increasing scientific attention over the past decades. Studying their primitive origins can reveal important insights on the formation of planets, as well as the general evolution of the Solar System. Also their potential threat to life on Earth upon collision and their potential to act as stepping stones for deep space exploration make these bodies interesting to explore. Especially CubeSats, being small and lightweight, are promising candidates for such missions.

To facilitate the design of small body missions, this research investigates the non-linear effects of uncertainties in an asteroid's environment on the orbital motion of a CubeSat. Uncertainties in the asteroid's mass, irregular gravity field and solar radiation pressure have been studied prior. Rotational state uncertainties have not been researched, but do affect the CubeSat's motion indirectly through the orientation of the irregular gravity field. These are therefore selected as the subject of this work. This aids in identifying orbits that are robust against these uncertainties, thereby minimizing the required fuel for trajectory corrections and maximizing the mass for science instruments or increasing the mission duration.

The study of the non-linear effects of rotational state uncertainties requires the application of non-linear uncertainty propagation methods. Non-Intrusive Polynomial Chaos was selected for its ease of implementation, promising computational efficiency and ability to provide statistical information directly. In this method, a set of samples from the uncertain domain are propagated to a desired time according to the black-box dynamics that govern the orbital motion. Subsequently, a polynomial approximation, a so-called Polynomial Chaos Expansion, is constructed for these final states as a function of the uncertain variables. This then allows for finding the final states for all possible characterisations of these uncertain variables, in a Monte Carlo like fashion, without further numerical integrations. Above that, the Polynomial Chaos Expansion terms can be used to compute statistics, such as the mean and covariance, analytically. In this work, different initial conditions are propagated and the states at various times are approximated by Polynomial Chaos Expansions. All Polynomial Chaos Expansions were verified by comparison with Monte Carlo simulations.

A study on the settings of Non-Intrusive Polynomial Chaos was conducted. It showed that the required settings, such as polynomial order, number of samples and method of solving for the coefficients can vary significantly, depending on the studied case. In addition, limitations in the application of this method to Kepler elements were encountered for orbits that approach the singularities in this element set.

In general, the results show an increase in the trajectory dispersions and non-linearities encountered with an increase in propagation times and with a decrease in orbital altitude. However, exceptions to this trend were encountered. In the case of a retrograde equatorial orbit, the inclination was found to reach its maximum dispersion already within 5 days and stagnates thereafter. This is a result of the accelerations exerted by the asteroid's gravitational bulges in its equatorial plane, which varies in space along with changes in the rotation pole under these uncertainties.

A comparison to uncertainties in the asteroid's mass revealed that the effects of rotational state uncertainties are relatively small, especially considering the small uncertainty in mass that was used. However, again an exception was encountered. The right ascension of the ascending node of a polar orbit at 5 km was found more sensitive to changes in the asteroid's rotation pole than in its mass. Thus, depending on the objective of an analysis, mission designers could be required to include rotational state uncertainties in their analyses.

Finally, a broader study of different initial orbital geometries revealed that retrograde orbits are more stable against rotational state uncertainties. However, depending on the exact initial orbital geometry, in terms of inclination and right ascension of the ascending node, prograde orbits can be just as stable. Also here it was found, though, that the inclination is more stable for polar orbits than for inclined and equatorial orbits.

In conclusion, the finding that retrograde orbits are more stable against rotational state uncertainties helps mission designers to select promising orbits for actual missions. As these orbits are also beneficial for geodetic parameter estimation, they both minimise the required fuel for trajectory corrections and maximise the scientific return. Nonetheless, a wide variety of non-linear effects due to rotational state uncertainties can be encountered in the asteroid's environment. Therefore, their influence should always be checked in mission design studies, even though in general their effects are relatively small.

Contents

List of Figures

List of Tables

Symbols

Abbreviations

ABM	Adams-Bashforth-Moulton integrator
BS	Bulirsch-Stoer integrator
CoF	Center of Figure
CT	Cross-Truncation
EoM	Equation of Motion
MC	Monte Carlo
MEE	Mean Equinoctial Elements
NEO	Near-Earth Object
NIPC	Non-Intrusive Polynomial Chaos
PC	Polynomial Chaos
PCE	Polynomial Chaos Expansion
PCQ	Point Collocation method with Quadrature sampling
PCR	Point Collocation method with quasi-Random sampling
PDF	Probability Density Function
PM	Point Mass
PSP	Pseudo-Spectral Projection method
RK	Runge-Kutta integrator
RKF	Runge-Kutta-Fehlberg integrator
RKDP	Runge-Kutta-Dormand-Prince integrator
RMSE	Root-Mean-Squared Error
SH	Spherical Harmonics
SRP	Solar Radiation Pressure
STT	State Transition Tensor
TudatPy	TU Delft Astrodynamics Toolbox (Python-interfaced)
UT	Unscented Transform

Latin symbols

$\boldsymbol{a}$	Acceleration
a	Semi-major axis
$\bar{C}$	Normalised spherical harmonic cosine coefficient
C_R	CubeSat's radiation pressure coefficient
$\boldsymbol{c}$	Polynomial coefficients
c	Speed of light
d	Distance
E	Expectation
e	Eccentricity
F_{ast}	Asteroid-fixed reference frame of initial epoch
F_{in}	Inertial reference frame in ECLIPJ2000
i	Inclination
L	True longitude
M	Asteroid's mass
m	CubeSat's mass
N	Number of samples/quadrature nodes
n	Number of uncertain variables
$\boldsymbol{P}$	Covariance matrix
$\bar{P}$	Normalised Legendre Polynomial

P	Power output
	Number of polynomial coefficients minus 1
p	Polynomial order
q	Number of state variables
	Quadrature order
$\boldsymbol{r}$	Position
R	Reference radius
r	Radial distance (body-fixed spherical coordinate)
S	Sum of polynomial coefficients of a specific order
s	Sobol' index
$\bar{S}$	Normalised spherical harmonic sine coefficient
S_{ref}	CubeSat's reference area
T_{ast}	Asteroid rotation period
T	Orbit period
t	Time
U	Gravitational potential
$\boldsymbol{v}$	Velocity
w	Quadrature weight
$\boldsymbol{x}$	State vector

Greek symbols

α	Diffusion coefficient
β	Rotation pole ecliptic latitude
Δ	Indicating a step or difference
ϵ_{max}	Maximum error
ζ_{RMSE}	Performance measure for RMSE
ζ_{max}	Performance measure for maximum error
θ	True anomaly
λ	Rotation pole ecliptic longitude
μ	Gravitational parameter
$\boldsymbol{\xi}$	Standard uncertain variables
ρ	Probability Density Function
	Pearson's correlation coefficient
σ	Standard deviation
τ	Longitude (body-fixed spherical coordinate)
$\boldsymbol{\Phi}$	State Transition Matrix
ϕ	Latitude (body-fixed spherical coordinate)
$\boldsymbol{\Psi}$	Multidimensional orthogonal polynomials
ψ	Univariate polynomial
Ω	Right ascension of the ascending node
ω	Argument of periapsis

Sub- and superscripts

$_{ast}$	Relating to the asteroid
$_{CS}$	Relating to the CubeSat
$_{grav}$	Gravitational
$_{i_{...}}$	Uncertain variable indicator
$_{j}$	Polynomial term indicator
$_{k}$	Quadrature node indicator
$_{l}$	General counter/indicator
$_{m}$	Spherical harmonic coefficient order
$_{n}$	Spherical harmonic coefficient degree
$_{pm}$	Point mass
$\boldsymbol{\kappa}$	Indicating a subset of a vector
$_{0}$	Initial
$_{\odot}$	Relating to the Sun

1 Introduction

The space industry has been and will continue growing rapidly [1]. The need to map the current state of climates worldwide [2], to forecast the weather[3] and to have reliable internet access and communication capabilities at remote locations [4] have inspired a wide variety of satellite missions around Earth. This large increase in space missions has been enabled by a reduction in the cost of launches [5] and the emergence of small satellite systems, such as CubeSats [6]. The exploration of space beyond Earth orbit has also received more interest recently. For example, the JUpiter ICy moons Explorer (JUICE), launched in April 2023, will characterise the ocean layers on Ganymede [7], while the James Webb Space Telescope [8], launched in December 2021, will study light emitted by galaxies in the distant past.

The scientific community has also increasingly focused on the smaller celestial bodies within the Solar System [9]. These bodies are considered to be the most ancient remnants from different stages of the Solar System's evolution [10]. Their diverse characteristics, in terms of their constituent elements and internal structure, serve as indicators of these different stages [11], while their orbital characteristics and rotational states provide information on the physical processes they have undergone [12]. Exploring the features of these small objects can therefore offer valuable information about the formation, growth and evolution of planets and the Solar System as a whole. A subset of these bodies, known as near-Earth objects (NEOs), approach or intersect Earth's orbit. Having the potential to collide with Earth, these small bodies pose a threat to life, and civilization, on Earth, sparking the need for small body space missions to avoid such events. Although many large NEOs have been identified already, large efforts are ongoing to detect a vaster majority of them and the smaller ones [13]. The testing of deflection techniques has also been initiated with the kinetic impact of DART on Dimorphos [14]. Lastly, the exploration of small bodies is motivated by the potential for mining materials scarce on Earth [15].

Numerous space missions committed to exploring the large variety of comets and asteroids have been motivated by these interests [16]. NEAR-Shoemaker has orbited Eros [17], Rosetta visited 67P/Churyumov-Gerasimenko [18], OSIRIS-REx took a sample from Bennu [19] and DART impacted Dimorphos [20, 14]. Planned missions include OSIRIS-APEX visiting Apophis during its close approach to Earth [21], HERA studying the aftermath of the DART impact [22] and Psyche exploring a metallic asteroid to learn about the origin of planetary cores [23].

Unlike planets, the mass of small bodies is insufficient to force them to spherical shapes. The resulting irregular gravity field in combination with the solar radiation pressure (SRP) perturbation, which is significant due to the weak gravity, cause high non-linearities in the dynamical environment and thereby complicate the design and execution of missions to small bodies. There is a high risk of colliding with or rapidly departing from the vicinity of the body after only a cursory period of observation. This work contributes to the large efforts required to carefully plan small body missions, by studying the dynamical environment of such a body. Previously, research has focused on general considerations [24], the motion around oblate bodies [25, 26] and contact binaries [27] and uncertainties in mass, SRP [28], irregular gravity [29, 30] and initial states [31]. The influence of uncertainties in the possibly complex rotational state of the asteroid [24] on the orbital motion has not been studied, while they indirectly affect the orbital motion, through the orientation of the asteroid's irregular gravity field and the changes therein. Rotational state uncertainties are therefore selected as the subject of this work.

The highly non-linear dynamical environment of small bodies necessitate the application of non-linear uncertainty propagation methods to study uncertainties. In this work, the effects of uncertainties in a small body's rotational state are studied using Non-Intrusive Polynomial Chaos (NIPC). This sample based methods considers the orbital motion as a black-box function and approximates the states at given times by Polynomial Chaos Expansions (PCE), as a function of the uncertain parameters. This method was selected over Monte Carlo (MC) methods [32], Differential Algebra [33], the Unscented Transform (UT) [34], the State Transition Tensor (STT) [35] and intrusive Polynomial Chaos (PC) [36] due to its ease of implementation, its promising computational efficiency and its ability to analytically compute statistical information from the PCE.

In this thesis work, the uncertainties in the rotational state parameters are studied for a particular case study object. Oblate near-Earth asteroid 2000 ET70, of which Earth-based radar observations are available, was selected for its representative size, shape and rotation period [24, 37]. The largest gravity perturbations, based on its shape, are those described by the Spherical Harmonic (SH) $\bar{C}_{20}$ and $\bar{C}_{22}$ terms, which define its oblateness and equatorial elongation, respectively. Uncertainties related to both a pre-mission scenario and a post early-characterisation phase are studied, because these different uncertainty magnitudes are expected to result in different degrees of non-linearity and dispersion and are representative of different mission phases. A CubeSat is employed to orbit this asteroid, because they have been proven to be promising candidates for space exploration. For example, the HERA mission, planned for launch in 2024, utilises two CubeSats, Juventas and Milani, for characterising the DART impact on Dimorphos [38]. CubeSats have the advantages of being smaller, lighter and faster to develop than their larger counterparts [39]. Although this is accompanied with limits in their operational and scientific capabilities, research efforts are focused on increasing the autonomous capabilities of CubeSats [40]. Nonetheless, it could still be required to employ them alongside a larger spacecraft or with several CubeSats in a real mission.

1.1. Research question

The main objective of this research, as just introduced, is thus to study the non-linear effects of an asteroid's rotational state uncertainties on a CubeSats orbital motion. To guide the research effort into a more precise direction, the main research question, based on this objective, is formulated as:

What are the non-linear effects of an asteroid's rotational state uncertainties on the orbital motion of a CubeSat?

To structure the research effort into clearer sub-directions, the main question was divided into sub-questions:

- What are the capabilities of Non-Intrusive Polynomial Chaos and what challenges are encountered in its application to orbital motion around asteroids?
- What orbital aspects are affected the most by rotational state uncertainties?
- Do particular interactions between rotational state parameters and irregular gravity field components contribute relatively more to the dispersion of orbits than others?
- Should rotational state uncertainties be considered in mission design studies and operational procedures?

1.2. Report structure

The main part of this research has been documented as a journal paper article in chapter 2. chapter 3 summarises the conclusions drawn in the research by answering the research question and provides recommendations for future research. The journal paper contents are complemented by the appendices of this report. Appendix A presents the design of the nominal orbits, while Appendix B provides an analysis of the required propagation settings for sufficient accuracy and efficiency. The performance of NIPC is studied in Appendix C, the conclusions of which formed guidelines in determining the settings used for the analyses performed in this work. The methodology described in Appendix D is used to filter discontinuities in the Kepler elements, so that they can be properly analysed. Finally, Appendix E presents additional results on the initial orbital geometry grid analysis and provides a more elaborate discussion for the analysis that studies interactions of rotational parameters with the irregular gravity field in terms of the degree 2 spherical harmonic coefficients.

2
Journal paper

Non-linear sensitivity of a CubeSat's orbital motion to an asteroid's rotational state uncertainties using Non-Intrusive Polynomial Chaos

Maarten van Nistelrooij ⋆

Delft University of Technology, the Netherlands

24 May 2023

ABSTRACT

Context Small solar system bodies have received increasing scientific attention, because of their primitive origins and potential threat to life on Earth. Studying them with small and lightweight CubeSats can reveal important insights in the evolution of the solar system.

Aims To facilitate the design of small body missions, this work investigates the non-linear effects of uncertainties in an asteroid's rotational state on the orbital motion of a CubeSat.

Methods Non-Intrusive Polynomial Chaos is employed for the non-linear, yet efficient, propagation of these uncertainties in the highly non-linear dynamical environment of the asteroid. Different initial conditions are propagated and the states at various times are approximated by Polynomial Chaos Expansions, from which statistical information of the dispersion of the trajectories can be computed analytically.

Results In general the effects are smaller compared to those due to uncertainties in mass. However, the rotational state parameters can in particular cases affect the angular Kepler elements more, e.g. the right ascension of the ascending node of a polar orbit. In addition, retrograde orbits are found to be more stable against rotational state uncertainties than prograde orbits. Depending on the exact initial orbital geometry, also prograde orbits can be stable, though. Again, different results were also obtained, such as the inclination being more stable for polar orbits than for retrograde orbits. Finally, limitations in the application of NIPC to Kepler elements were encountered for orbits that approach the singularities in this element set.

Conclusions In conclusion, a wide variety of effects due to rotational state uncertainties can be encountered, because of the highly non-linear dynamical environment. Therefore, their influence should always be checked in mission design studies, even though in general their effects are relatively small.

Keywords: Non-intrusive Polynomial Chaos, asteroid, non-linear sensitivity analysis, rotational state

1 Introduction

The large variety of small solar system bodies has received increasing attention over the past decades (Hestroffer et al., 2019). Being believed to be the most primitive celestial bodies, they could be remnants from the formation of the Solar System and its different evolutionary stages (Bottke Jr. et al., 2002). Their composition and internal structure are records of the conditions within the young Solar System. (DeMeo and Carry, 2014). Observing and characterising these bodies may therefore reveal key insights into the early development of planets, prior to their interior differentiation, as well as the Solar System in general. Similarly, their orbital and rotational states characterise their dynamical evolution (Morbidelli et al., 2005). Also the threat to life, and civilization, on Earth upon collision and the potential for mining materials scarce on Earth motivate the exploration of small solar system bodies (Swindle et al., 2017).

These various interests have inspired numerous space missions committed to exploring a variety of comets and asteroids (Barucci et al., 2011). NEAR-Shoemaker orbiting Eros (Miller et al., 2002), Rosetta visiting 67P/Churyumov-Gerasimenko (Lhotka et al., 2016), OSIRIS-REx returning a sample from Bennu (Lauretta et al., 2017) and DART impacting Dimorphos (Cheng et al., 2018) are some examples. Currently planned missions include OSIRIS-APEX visiting Apophis during its close approach to Earth (Benson et al., 2023), HERA studying the DART impact (Madeira et al., 2023) and Psyche exploring the same name bearing metallic asteroid in an effort to uncover the origin of planetary cores (Zuber et al., 2022).

The small mass of asteroids is insufficient to force them to spherical shapes. The resulting weak and irregular gravity fields cause high non-linearities to be encountered in a spacecraft's or-

⋆ E-mail: m.j.m.vannistelrooij@student.tudelft.nl

bital motion around them (Feng et al., 2019a), which is directly impacted by the body's rotation. This is further complicated by solar radiation pressure (SRP), which forms a significant perturbation already over short time periods. The design and execution of such missions is therefore difficult, but has been facilitated by studies of the highly perturbed and uncertain dynamical environment of small bodies. The implications and general considerations are described extensively by Scheeres (2012). Takahashi and Scheeres (2020) investigate the effects of J_2 and J_3 on frozen terminator orbits and Feng and Hou (2018) derive a semi-analytical method for propagating orbital motion around oblate asteroids. The sensitivity of orbits to uncertainties in the asteroids mass and SRP (Feng et al., 2022), the irregular gravity field (Melman et al., 2013; Feng et al., 2021) and the initial state within, and the mass of, a binary system (Fodde et al., 2022) have also been researched extensively. Uncertainties in the possibly complex rotational state of small bodies indirectly affect a spacecraft's orbital motion, through the orientation of the small body and the changes therein. The influence of the possibly complex rotational state of a small body (Scheeres, 2012; Feng et al., 2019b) on this motion has not been studied and is the subject of this work.

Where linear uncertainty propagation methods can be applied in situations that are nearly linear in order to study the sensitivity of the orbital motion to specific parameters, the characteristics of the asteroid's environment necessitate the application of non-linear uncertainty propagation methods. Monte Carlo (MC) methods (Maybeck, 1982) have been employed in these problems (Melman et al., 2013), as they are easily implemented, yet they are also most inefficient. Differential Algebra (DA) (Armellin et al., 2010; Feng et al., 2021; 2022) and polynomial algebra (Fodde et al., 2021; 2022) have been researched extensively in this field as well. Although other non-linear uncertainty propagation methods, such as the Unscented Transform (UT) (Julier et al., 2000), the State Transition Tensor (STT) (Park and Scheeres, 2006) and Polynomial Chaos (PC) (Wiener, 1938), have been applied in astrodynamics problems, they are yet untouched in asteroid applications. In this work, the non-intrusive variant of polynomial chaos is employed, which approximates the output of a black-box function through a Polynomial Chaos Expansion (PCE). This method was selected for its ease of implementation, its promising efficiency and its ability to compute statistical moments and Sobol' indices analytically from the PCE.

The uncertainties in rotational state parameters are studied for oblate near-Earth asteroid 2000 ET70, of which Earth-based radar observations are available and which has a representative size and rotation period (Naidu et al., 2013). In addition, a CubeSat is used as the spacecraft that orbits the asteroid. CubeSats have been proven to be promising candidates for deep space exploration and have the advantage of being smaller, lighter and faster to develop than their larger counterparts (Poghosyan, 2017). This is, however, also accompanied with limits in their capabilities, both operational and scientific.

This work is structured as follows. First, section 2 presents the general dynamical framework used in this work. Subsequently, section 3 presents the Non-Intrusive Polynomial Chaos (NIPC) method and elaborates on the considerations that must be made with regard to its use. In addition, the statistical information that can be obtained with this method and the uncertainty indicators used for the analyses are presented in this section. Section 4 ties together the foregoing sections by presenting the characteristics of asteroid 2000 ET70, the uncertainties studied, the orbits considered and the specific dynamical model settings applied. Then, section 5 dives into the performance of NIPC and provides some general guidelines that were found when testing the settings available in this method. It also provides an overview of the NIPC settings used in this work. The results of the various sensitivity analyses are presented and discussed extensively in section 6. Finally, section 7 summarises the conclusions and recommendations of this work.

2 Dynamical model

The CubeSat's orbital motion around the asteroid, in Cartesian coordinates $\boldsymbol{r} = [x\ y\ z]^{\mathrm{T}}$, is defined in an inertial reference frame, $\mathcal{F}_{in}$. This frame is centered at the asteroid's Center of Figure (CoF), its x-axis oriented towards vernal equinox at J2000, its z-axis oriented perpendicular to the North of the ecliptic and the y-axis complementing the right handed frame. The orbital motion is governed by the Equation of Motion (EoM):

$$\ddot{\boldsymbol{r}}(t) = \boldsymbol{a}_{grav} + \boldsymbol{a}_{srp} + \boldsymbol{a}_{\odot,pm} \tag{1}$$

where $\boldsymbol{a}_{grav}$ is the gravitational acceleration exerted by the asteroid, $\boldsymbol{a}_{srp}$ is the acceleration due to SRP and $\boldsymbol{a}_{\odot,pm}$ is the Sun's third body point mass (PM) acceleration. The EoM is used to propagate the state, $\boldsymbol{x}(t) = [\boldsymbol{r}(t)\ \dot{\boldsymbol{r}}(t)]^{\mathrm{T}}$ in $\mathcal{F}_{in}$, to various times t, subject to an initial state $\boldsymbol{x}(t_0)$.

The asteroid's gravitational acceleration is modelled using the Spherical Harmonics (SH) model, commonly truncated for degree n and order m (Montenbruck and Gill, 2000):

$$\begin{aligned}\boldsymbol{a}_{grav} &= \mathcal{R}_z(-\lambda)\mathcal{R}_y(\beta - \tfrac{\pi}{2})\cdot \\ &\qquad \mathcal{R}_z(-\tfrac{2\pi}{T_{ast}}(t-t_0))\boldsymbol{\nabla}U(r,\phi,\tau) \\ U(r,\phi,\tau) &= \frac{\mu}{r}\sum_{n=0}^{\infty}\sum_{m=0}^{n}\Bigg[\left(\frac{R}{r}\right)^n\cdot \\ &\qquad \bar{P}_{nm}(\sin\phi)\left(\bar{C}_{nm}\cos m\tau + \bar{S}_{nm}\sin m\tau\right)\Bigg]\end{aligned} \tag{2}$$

Here, U is the gravitational potential defined in the co-rotating asteroid-centered reference frame, such that r, ϕ and τ are the radius, latitude and longitude with respect to the asteroid. μ is the asteroid's gravitational parameter, R its reference radius, $\bar{P}_{nm}$ are the normalised Associated Legendre Polynomials and $\bar{C}_{nm}$ and $\bar{S}_{nm}$ are the normalised SH coefficients. The gravitational acceleration in the asteroid-fixed reference frame is transformed to $\mathcal{F}_{in}$ through three rotations, $\mathcal{R}$. The first rotation is

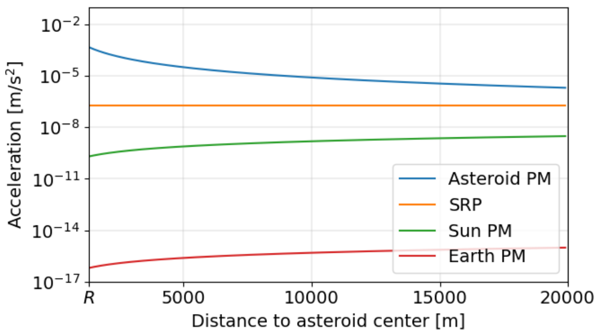

Fig. 1. Magnitudes of accelerations with respect to asteroid 2000 ET70 ($a = 0.947$ AU, $e = 0.124$, $i = 22.3°$)

around the asteroid's rotation pole with a magnitude inversely proportional to the asteroid's rotation period T_{ast} and proportional to the propagation time $t - t_0$. The other rotations transform the asteroid-fixed frame of the initial epoch t_0 to $\mathcal{F}_{in}$, taking into account the ecliptic latitude β and ecliptic longitude λ of the rotation pole in $\mathcal{F}_{in}$.

The SRP acceleration is modelled with the Cannonball model (Scheeres, 2012), because of its low computational cost and good accuracy:

$$\boldsymbol{a}_{srp} = -\frac{P_\odot}{4\pi c}\frac{C_R S_{ref}}{m}\frac{\boldsymbol{r}_{CS/\odot}}{\boldsymbol{r}^3_{CS/\odot}} \tag{3}$$

where $P_\odot = 3.827 \cdot 10^{26}$ W is the total power output by the Sun, $c = 2.998 \cdot 10^8$ ms^{-1} is the speed of light, C_R is the CubeSat's SRP coefficient, S_{ref} its SRP reference area, m its mass and $\boldsymbol{r}_{CS/\odot}$ the Sun's position vector as seen from the CubeSat.

Finally, based on the comparison of accelerations provided in Figure 1, where R represents the asteroid's mean radius (Table 2), the Earth's third body PM is concluded negligible, as it is many orders of magnitudes smaller than the other accelerations. As such, only the Sun's third body PM acceleration is included in this work, which is given as the difference between that exerted on the CubeSat and on the asteroid:

$$\boldsymbol{a}_{\odot,pm} = \mu_\odot \left(\frac{\boldsymbol{r}_{CS/\odot}}{\boldsymbol{r}^3_{CS/\odot}} - \frac{\boldsymbol{r}_\odot}{\boldsymbol{r}^3_\odot}\right) \tag{4}$$

with $\boldsymbol{r}_\odot$ being the Sun's position as seen from the asteroid.

The EoM contains many case-dependent parameters. They are governed by the choice of asteroid or spacecraft design. Several of these parameters are also subject to uncertainty. They are not known exactly by mission designers, either due to the large effort required or the inability to determine them with current technology. This work focuses on uncertainties that arise due to a lack of knowledge, which can be reduced with additional information (Eldred, 2009). Examples are μ, $\bar{C}_{nm}$ and C_R. β, λ and T_{ast} are uncertain as well. They affect the orbital motion indirectly, by defining the asteroid's orientation and its change over time. Thereby they define how the gravitational potential U varies in inertial space and time, as indicated by Equation 2.

Uncertainties are usually defined with Probability Density Functions (PDF) (Feng et al., 2019b). Gaussian or Uniform distributions (Eldred, 2009) are most commonly used, because in typical astrodynamics problems only a nominal value and uncertainty magnitude are known or estimated, rather than higher order moments that would describe more complicated PDFs. The nominal value, typically the expected value for the Gaussian and Uniform distributions, is the value that best fits reference data or observations. Specific information on the uncertainties studied in this work is given in section 4.

The mismodelling of parameters, due to uncertainties, results in dynamical model errors. To quantify this type of error, which is the subject of this work, errors originating from other sources should be controlled. These include the dynamical model errors originating from the choice of models and the integration error originating from solving for the state of interest, $\boldsymbol{x}(t)$, numerically. The error due to model choices, for each of the acceleration terms in the EoM, can be reduced by employing increasingly sophisticated models. It is realised though, that the current study of uncertainties is not necessarily about finding the true orbit solution, but merely about finding reliable estimates of the errors therein due to the uncertainties. This can justify allowing a larger error in the model of one acceleration, when studying the effects of uncertainties in another. Although the errors due to model choices may then be larger than the size of the errors due to uncertainties that should be captured, this error may still be properly captured. Of course, indirect effects should still be considered, as they may indirectly affect the errors due to uncertainties as well, especially for longer propagation times. The dynamical model choices that are made in this regard are elaborated upon in section 4. On the other hand, the integration error directly affects the accuracy with which errors due to uncertainties can be captured. The required integration error is therefore set at the minimum of the errors due to uncertainties that need to be captured. A priori it is not known what magnitude of errors due to uncertainties will be encountered, but in terms of position deviations of the CubeSat, it is physically significant to be able to capture effects in the order of cm to dm-level. Errors below cm-level are insignificant and need not be detected, because they yield no significant change in the CubeSat's orbit. Integration errors of cm to dm-level maximum are thus acceptable.

The numerical propagations were performed with the Python-interfaced TU Delft Astrodynamics Toolbox (TudatPy) developed by the Astrodynamics & Space Missions department of Delft University of Technology[1].

3 Non-Intrusive Polynomial Chaos

The effects of uncertain parameters in the EoM are studied with Non-Intrusive Polynomial Chaos (NIPC), the foundation of which was laid by Wiener (1938). This method is used to estimate the distribution of the state of interest, $\boldsymbol{x}(t)$, subject to

[1] `https://docs.tudat.space/`

variations in the uncertain parameters gathered in $\boldsymbol{\xi}$. The state subject to these uncertainties is denoted $\boldsymbol{x}(t, \boldsymbol{\xi})$. This section elaborates on NIPC, the options therein, the considerations to take into account and the statistical information that can be obtained.

NIPC is a black-box non-linear uncertainty propagation method. This means that a limited number of samples are drawn from the domain of the uncertain parameters $\boldsymbol{\xi}$ and propagated according to the dynamics governed by the EoM, which is considered the black box in this work. The propagated states at the time of interest of all samples are used to generate an approximation function of this state, with the uncertain parameters $\boldsymbol{\xi}$ as independent variables. This function is a set of multivariate orthogonal polynomials $\boldsymbol{\Psi}(\boldsymbol{\xi})$, also referred to as the Polynomial Chaos Expansion (PCE) (Xiu and Karniadakis, 2002; Xiu, 2010; Eldred, 2009):

$$\begin{aligned}\boldsymbol{x}(t,\boldsymbol{\xi}) =& \boldsymbol{c}_0(t)\Psi_0 \\ &+ \sum_{i_1=1}^{\infty} \boldsymbol{c}_{i_1}(t)\Psi_1(\boldsymbol{\xi}_{i_1}) \\ &+ \sum_{i_1=1}^{\infty}\sum_{i_2=1}^{i_1} \boldsymbol{c}_{i_1 i_2}(t))\Psi_2(\boldsymbol{\xi}_{i_1},\boldsymbol{\xi}_{i_2}) \\ &+ \sum_{i_1=1}^{\infty}\sum_{i_2=1}^{i_1}\sum_{i_3=1}^{i_2} \boldsymbol{c}_{i_1 i_2 i_3}(t)\Psi_3(\boldsymbol{\xi}_{i_1},\boldsymbol{\xi}_{i_2},\boldsymbol{\xi}_{i_3}) \\ &+ ... \end{aligned} \tag{5}$$

In practise, the state is approximated by a truncated summation, by using a polynomial of of finite order p. By summing over the individual polynomial terms indicated by j, rather than by the uncertainties in a term as indicated by i_1, i_2, etc., a shorthand notation is given as:

$$\boldsymbol{x}(t,\boldsymbol{\xi}) \approx \sum_{j=0}^{P} \boldsymbol{c}_j(t)\Psi_j(\boldsymbol{\xi}) \tag{6}$$

$$\text{where} \quad \Psi_j(\boldsymbol{\xi}) = \prod_{i=1}^{l} \psi_i^j(\boldsymbol{\xi}_i)$$

where $\boldsymbol{c}_j(t)$ are the PCE coefficients to be obtained for the time of interest. $\psi_i^j(\boldsymbol{\xi}_i)$ forms an orthogonal polynomial basis function, denoting the contribution of uncertain parameter i to polynomial term j. The last line of Equation 6 therefore informs that each polynomial term consisting of l variables, can be obtained by a multiplication of univariate polynomial terms $\psi_i^j(\boldsymbol{\xi}_i)$, one for each of these l variables. Note that Equation 6 constructs a PCE for each state variable and thus the PCE coefficients have to be computed for each of them (Xiu and Karniadakis, 2002; Eldred, 2009).

Besides NIPC, also an intrusive variant of PC exists. This method considers a direct substitution of the PCE, Equation 6, into the EoM. Such a PCE is, in this case, also made and substituted into the EoM for the uncertain parameters. By projecting the EoM onto each of the orthogonal polynomial basis functions, it can be rewritten so that the PCE coefficients become the state variables and can be solved for with numerical integration methods (Xiu and Karniadakis, 2002; Lacor and Savin, 2018). The intrusive method can be more efficient, especially with an increasing number of uncertain parameters. However, its main disadvantage is that the EoM becomes coupled and extensive code modifications would be required to implement it in existing tools, such as TudatPy (Xiong et al., 2014). Therefore, this method was not considered in this work.

In essence, the NIPC method is an adaptation of the widely adopted, yet inefficient, Monte Carlo (MC) method, by using clever sampling techniques and combining the information that is available within these samples wisely to construct a polynomial approximation of the state distribution. The clever use of this information is what makes this method computationally more efficient than the MC method (Hosder et al., 2007).

The major burden of NIPC, aside from finding the solutions to the black-box function (EoM), lies in the computation of the $P+1$ PCE coefficients per state coordinate. Nonetheless, the same samples can be reused for each. The number of PCE coefficients per state coordinate follows from (Xiu and Karniadakis, 2002; Eldred, 2009):

$$P + 1 = \frac{(n+p)!}{n!p!} \tag{7}$$

where n denotes the number of uncertain parameters in $\boldsymbol{\xi}$ and p denotes the polynomial order. Equation 7 clearly shows the curse of dimensionality, i.e. the number of PCE coefficients increases exponentially with n and p. As will be discussed in the following subsections, the number of samples required increases with the number of PCE coefficients. Thus, the method becomes exponentially more costly with the number of uncertain parameters and the degree of non-linearity of the problem.

3.1 *Methods for computing* $\boldsymbol{c}(t)$

The PCE coefficients can be computed using the propagated states with several methods. Two of these are considered in this work, because of their availability in ChaosPy (discussed in subsection 3.4): Pseudo-spectral projection and Point Collocation. These methods are elaborated upon next.

3.1.1 *Pseudo-spectral projection*

Similar to the intrusive Polynomial Chaos method, the Pseudo-spectral projection (PSP) method relies on a projection onto the orthogonal polynomial basis functions. Where in the intrusive method this projection is done for the complete EoM, here it is done only for the PCE of the state of interest. In this way the error made in the approximation of the states is orthogonal to the PCE and therefore minimised for the used PCE. The coefficients for a specific time t_l follow from (Eldred, 2009; Vasile and Manzi, 2023):

$$\begin{aligned}\boldsymbol{c}_j(t_l) =& \frac{\int \rho(\boldsymbol{\xi})\boldsymbol{x}(t_l,\boldsymbol{\xi})\Psi_j(\boldsymbol{\xi})\mathrm{d}\boldsymbol{\xi}}{\langle\Psi_j^2\rangle} \\ \approx& \frac{\sum_{k=1}^{N} w_k \boldsymbol{x}(t_l,\boldsymbol{\xi}_k)\Psi_j(\boldsymbol{\xi}_k)}{\langle\Psi_j^2\rangle} \\ \text{where} \quad & \langle\Psi_j^2\rangle = \prod_{i=1}^{l}\langle(\psi_i^j)^2\rangle\end{aligned} \tag{8}$$

where quadrature rules are used to generate N nodes $\boldsymbol{\xi}_k$ with weights w_k, which approximate the integral in the numerator with $\rho(\boldsymbol{\xi})$ representing the PDF of $\boldsymbol{\xi}$. $\langle\Psi_j^2\rangle$ is the inner product of multivariate polynomial term j, which follows from the product of inner products of its constituent univariate polynomial terms, which can be computed analytically (Eldred, 2009).

For multiple uncertain parameters, univariate quadrature rules are extended through full tensor products. Common rules, such as Clenshaw-Curtis, Gaussian, Fejer and Legendre quadrature yield $N = (q+1)^n$ quadrature nodes for quadrature order q. Other rules follow slightly different relations. Nonetheless, for all rules it holds that N grows exponentially with n. When the number of uncertain parameters grows beyond certain values, depending on the problem at hand, full tensor product quadrature becomes inefficient, similar to MC methods. In this case, Smolyak sparse grids can be considered to keep the required number of nodes low (Smolyak, 1963; Xiong et al., 2010). Although it can theoretically be deduced that a quadrature order $q = p+1$ is required to compute the PCE coefficients for a polynomial of order p with high accuracy (Eldred, 2009), this has limited use in practise. The reason is that, as will be encountered for some cases that are studied in section 6, the accuracy of the PCE will strongly depend on whether the distribution of the state of interest can actually be well represented by a polynomial of order p at all. Nonetheless, computing the PCE coefficients for higher orders with sufficient accuracy requires more samples than for lower orders.

3.1.2 *Point Collocation*

The Point Collocation method constructs a linear system, $\boldsymbol{x}(t,\boldsymbol{\xi}) = \boldsymbol{\Psi}(\boldsymbol{\xi})\boldsymbol{c}(t)$, and follows a least-squares regression to compute the PCE coefficients at a specific time t_l:

$$\boldsymbol{c}(t_l) \approx \left(\boldsymbol{\Psi}(\boldsymbol{\xi})^T\boldsymbol{\Psi}(\boldsymbol{\xi})\right)^{-1}\boldsymbol{\Psi}(\boldsymbol{\xi})^T\boldsymbol{x}(t_l,\boldsymbol{\xi}) \tag{9}$$

As a minimum, the number of samples must equal the number of PCE coefficients to avoid an under-determined system, but it is recommended to use twice this amount for significantly better approximations (Hosder et al., 2007). These samples can be generated in two ways. Again, quadrature rules can be employed, yielding the Point Collocation Quadrature (PCQ) method. In contrast to PSP, the weights are not used in this method, but in theory could be added to the least-squares regression. Additionally, quasi-random sampling sequences, such as Sobol, Hammersley and Halton, can be employed, yielding the Point Collocation Quasi-Random (PCR) method.

3.1.3 *Considerations*

The polynomial basis functions, $\psi_i^j(\boldsymbol{\xi}_i)$, can take any form, such as Hermite, Laguerre, Jacobi and Legendre polynomials. It was realised by Xiu and Karniadakis (2002), that each weighting function, which defines the inner product with respect to which one of these polynomials is orthogonal, is equal to the PDF of an uncertainty distribution, aside from a constant factor. For example, the PDF of a standard Gaussian distribution, $\frac{1}{\sqrt{2\pi}}e^{\frac{-x^2}{2}}$, is the same as the weighting function of Hermite polynomials, $e^{\frac{-x^2}{2}}$, aside from the constant factor $\frac{1}{\sqrt{2\pi}}$. Xiu and Karniadakis (2002) have shown that choosing the polynomial basis functions according to the uncertainty distribution yields exponential convergence of the PCE approximation, which is maximum.

When uncertain parameters behave according to different distribution types, the polynomial basis function becomes a mix of different types. When these uncertain parameters are correlated, an additional step is required for optimal performance. This step entails a transformation from uncorrelated standard uncertain parameters, such as Gaussian distributions with mean 0 and standard deviation 1 or uniform distributions between -1 and 1, to the real, correlated uncertain parameter values. This transformation could be considered part of the black-box function in NIPC. In this case, the uncorrelated standard uncertain parameters are the independent variables of the PCE. This transformation decouples the multidimensional integrals that occur in the inner products of multivariate polynomials, $\langle\Psi_j^2\rangle$, into a product of one-dimensional integrals, meaning that Equation 8 still holds. As will be elaborated in section 4, this study only considers uncorrelated uniform distributions. Thus, there is no need to do the transformation to uncorrelated standard uncertain parameters.

3.2 *Statistical information*

A powerful characteristic of NIPC is that statistical characteristics of the distribution of the state can be retrieved from the PCE directly. That is, for this only the PCE coefficients and the evaluations of the multivariate polynomial terms at the used nodes are required. The expectation, E, of a state variable follows directly from its zeroth coefficient, because its corresponding polynomial term equals 1. The covariance matrix, $\boldsymbol{P}$, can be obtained from the other PCE coefficients and their corresponding polynomial terms. For time t_l they follow from:

$$\begin{aligned}\mathrm{E}[\boldsymbol{x}(t_l,\boldsymbol{\xi})] =& \boldsymbol{m}(t_l) = \boldsymbol{c}_0(t_l) = \\ & \begin{bmatrix} c_{x_1,0}(t_l) & c_{x_2,0}(t_l) & \dots & c_{x_q,0}(t_l)\end{bmatrix}^T\end{aligned} \tag{10}$$

$$
\boldsymbol{P}(t_l) = \begin{bmatrix} \sum_{j=1}^{P} \langle \Psi_j^2 \rangle c_{x_1,j}^2(t_l) & \sum_{j=1}^{P} \langle \Psi_j^2 \rangle c_{x_1,j}(t_l) c_{x_2,j}(t_l) & \dots & \sum_{j=1}^{P} \langle \Psi_j^2 \rangle c_{x_1,j}(t_l) c_{x_q,j}(t_l) \\ \sum_{j=1}^{P} \langle \Psi_j^2 \rangle c_{x_2,j}(t_l) c_{x_1,j}(t_l) & \sum_{j=1}^{P} \langle \Psi_j^2 \rangle c_{x_2,j}^2(t_l) & \dots & \sum_{j=1}^{P} \langle \Psi_j^2 \rangle c_{x_2,j}(t_l) c_{x_q,j}(t_l) \\ \vdots & \vdots & \ddots & \vdots \\ \sum_{j=1}^{P} \langle \Psi_j^2 \rangle c_{x_q,j}(t_l) c_{x_1,j}(t_l) & \sum_{j=1}^{P} \langle \Psi_j^2 \rangle c_{x_q,j}(t_l) c_{x_2,j}(t_l) & \dots & \sum_{j=1}^{P} \langle \Psi_j^2 \rangle c_{x_q,j}^2(t_l) \end{bmatrix} \tag{11}
$$

where the dependence of Ψ_j on $\boldsymbol{\xi}$ has been left out for brevity. $c_{x_i,j}$ is the j-th coefficient corresponding to state variable x_i. Higher order moments of the distribution can be obtained similarly (Savin and Faverjon, 2017).

The contribution of a specific uncertain parameter, or an interaction of multiple uncertain parameters, to the variance can be obtained by summing the contributions of all terms containing those uncertain parameters. This allows for the simple computation of Sobol' indices, s, both of a finite order and of total order, by dividing these contributions by the total variance σ^2 (Sudret, 2008). As an example, the second order Sobol' index, $s_2(t_l)$, for the interaction between uncertain variables i_1 and i_2 on state coordinate x_1 is:

$$
s_2 = \frac{\langle \Psi_{i_1,i_2}^2 \rangle c_{x_1,i_1} c_{x_1,i_2}}{\sigma_{x_1}^2} \tag{12}
$$

where Ψ_{i_1,i_2} indicates the polynomial term(s) that are only a function of both i_1 and i_2. In essence, all of the information on relative contributions is already contained in the individual terms and the coefficients of the PCE. In Equation 12, the dependence of $\boldsymbol{c}$ on time t_l has been left out for brevity. This will also be done in the next subsection about uncertainty indicators, but it must be remembered that all statistical information and uncertainty indicators are always computed for a specific time t_l.

3.3 Uncertainty indicators

Besides the statistical moments and Sobol' indices, other uncertainty indicators are often used to provide information on additional characteristics of the effects of uncertainties. Firstly, the diffusion coefficient α is based on the idea that the variance grows proportionally to t^α and is computed for state variable x_i as (Vasile and Manzi, 2023):

$$
\alpha_{x_i} \approx \frac{\log\left(\sum_{j=1}^{P} \langle \Psi_j^2 \rangle c_{x_i,j}^2 + 1\right)}{\log(t)} \tag{13}
$$

This indicator is used to analyse the relative growth of the variance throughout different periods in the propagations.

The degree of non-linearity of a particular problem can be analysed with the non-linearity index S_{p+1}. It is computed only using the PCE coefficients, by summing them for each polynomial order and estimating this sum for one polynomial order higher with a logarithmic regression (Fodde et al., 2022):

$$
S_l = \sum_{|\boldsymbol{\kappa}|=l} \boldsymbol{c}_{\boldsymbol{\kappa}} \tag{14}
$$

$$
\log S_l \approx \log A + Bl \quad \rightarrow \quad S_{p+1} \tag{15}
$$

where $|\boldsymbol{\kappa}| = l$ indicates the subset of the PCE coefficients that belong to a multivariate polynomial term of order l. The idea behind this concept is that, the larger S_{p+1}, the more important this term and the higher the non-linearity of the problem.

Finally, a more practical approach, from a mission operations point of view, is developed in this work. This approach constructs PCEs of the Kepler elements (semi-major axis a, eccentricity e, inclination i, argument of periapsis ω, right ascension of the ascending node Ω and true anomaly θ), which only requires a transformation from the Cartesian elements to them before computing the PCE coefficients. The idea is to transform the variation in each individual Kepler element into a distance d, in m. This distance is computed between indicative orbits corresponding to the distribution of the states of interest. These indicative orbits are the expected orbit and the orbit at one standard deviation from the expected orbit. The expectation E and standard deviation σ are obtained from the PCE with Equation 10 and 11 for each Kepler element (E_a and σ_a for the semi-major axis, etc.). The distance is computed for each Kepler element individually (d_a for semi-major axis, d_e for eccentricity, etc.). This requires the decoupling of the effects on each element and thus some assumptions to be made. For the distance d_a it is assumed that the orbit is circular, which is representative for typical missions, because then d_a is equal to the standard deviation of a. The distance d_e is maximum and equal at periapsis and apoapsis and thus conservatively computed there. This also assumes that the semi-major axis remains its expected value, because it simplifies the equation and still allows for analysing the individual effects. For the computation of d_i it is also assumed that the orbit is circular and that the semi-major axis remains its expected value for the same reasons. The distances follow from:

$$
d_a = \sigma_a \tag{16}
$$

$$
d_e = \mathrm{E}_a \sigma_e \tag{17}
$$

$$
d_i = 2\mathrm{E}_a \sin\frac{\sigma_i}{2} \tag{18}
$$

where the latter equation can also be used for ω, Ω and θ. These equations thus decouple the dispersion per Kepler element and are therefore indicative of the relative effects on each orbital

Table 1. NIPC setting options within ChaosPy

Setting	Options	
Computation method	PSP, PCQ	PCR
Polynomial type Polynomial order Extra option	Hermite, Laguerre, Jacobi, Legendre, ... 1, 2, ... Normal polynomials Cross-truncated polynomials	
Quadrature order Quadrature rule	1, 2, ... Clenshaw-Curtis Gaussian ... (16 options)	
Sampling sequence Sample size		Sobol Hammersley ... (11 options) $\geqslant P+1$
Extra option	Smolyak sparse grid	Antithetic

characteristic. Because of the assumptions made for this decoupling, these distances only provide a first-order indication of the magnitude of the dispersion in each element. They thus only allow for comparing the relative effects on the Kepler elements qualitatively to isolate the ones that are affected the most. This gives insight into the type of maneuvers that could be required to steer the CubeSat back into its planned orbit.

It has been realised that some of the Kepler elements, ω, Ω and θ are defined within a limited range of values from 0° to 360°. This is problematic for the construction of the PCE, if values near these boundaries are encountered. A part of the uncertain domain then takes on values near 0° and a neighbouring part takes on values near 360°, causing a discontinuity to arise. Such discontinuities are filtered, by shifting values of one part of the uncertain domain by 360°, so that the discontinuity is removed and the PCE can be constructed.

3.4 *ChaosPy*

The implementation of NIPC was enabled by ChaosPy, an open source Python software toolbox (Feinberg and Langtangen, 2015). The availability of a user guide and API[2] made the implementation straightforward. ChaosPy has been extensively verified and validated with two other software toolboxes that incorporate NIPC: The Dakota Project and the Opus Open Turns library. An overview of all the possible setting options within the NIPC framework in ChaosPy is presented in Table 1.

The methodology described so far, including the dynamical model and the NIPC framework, and the inputs and chosen settings of the models which are subject of the next section, are summarised in the flowchart in Figure 2.

[2] `https://chaospy.readthedocs.io/`

4 Case study

The NIPC framework presented in section 3 can be applied to any uncertain problem. Here, it is applied to the dynamics of a CubeSat orbiting an asteroid, as generally described in section 2. The detailed inputs that define the case study of this work are presented and elaborated upon in this section.

4.1 *Asteroid 2000 ET70*

Near-Earth asteroid (162421) 2000 ET70, in the following referred the as 'the asteroid', is selected for this work. This Aten asteroid with an absolute magnitude of 18.37 was discovered in 2000 and orbits the Sun at $a = 0.947$ AU with $e = 0.124$ and $i = 22.3^\circ$, making it go slightly beyond Earth's orbit (JPL, 2022). Relevant physical characteristics of the asteroid are presented in Table 2 (Naidu et al., 2013). Its shape, shown in Figure 3, reveals large ridges and concavities. The asteroid was selected mainly for of its size and rotation period, which are representative of a large group of asteroids (Scheeres, 2012) and the availability of a shape model from Earth-based radar observations (Naidu et al., 2013). The asteroid has not been previously visited by a spacecraft.

The normalised SH coefficients required to model the gravitational potential of the asteroid, according to Equation 2, were retrieved from the constant density shape model using the Global Spherical Harmonic (GSH) package which uses the model described by Root (2021). The main reason for using this package is its readily availability and its ability to simultaneously compute SH coefficients of any degree and order numerically. Another option would have been to compute them according to the method described by Balmino (1994). Although these yield straightforward equations for the degree 2 and 4 SH cosine coefficients of even orders for an ellipsoid as a function of its semi-axes, this computation becomes burdensome for other coefficients and more complicated shape models. SH cosine coefficients of uneven degree and/or order and sine coefficients are sought, though, because they may contribute significantly to the revelation of the effects of uncertainties in the rotational state parameters, especially over long propagation times. Nonetheless, high accuracy in these SH coefficients is not required, as they are highly uncertain, due to the unknown heterogeneous interior density distribution. As such, the GSH package provides the most efficient tool to obtain a set of nominal SH coefficients. The SH coefficients are obtained with the asteroid's mean reference radius, $R = 1131.6$ m, and a constant density of 2000 kgm^{-3} (Naidu et al., 2013) and are listed in Appendix A. For verification purposes, $\bar{C}_{20}$ and $\bar{C}_{22}$ were compared to those obtained from the ellipsoid's semi-axes with the analytical equations from Balmino (1994). These differ by 8% and 20%, respectively, which indicates that the orders of magnitude are the same and that these values are therefore good representatives for the asteroid.

A 6-Unit CubeSat of 8 kg is employed to orbit the asteroid,

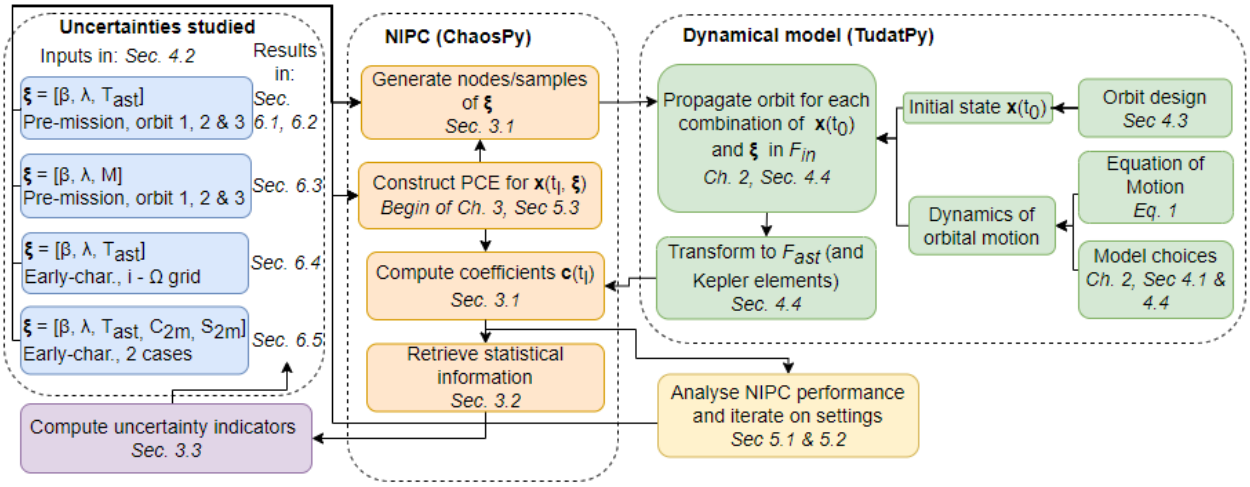

Fig. 2. Flowchart of the methodology of this work

Table 2. Asteroid 2000 ET70 characteristics (Naidu et al., 2013)

Quantity	Value
Size	2.61 x 2.22 x 2.04 km
R	1131.6 m
μ	810.05 $\mathrm{m^3 s^{-2}}$
β, λ	$-50°, 80°$
T_{ast}	8.96 hr
SH Coefficients	Appendix A

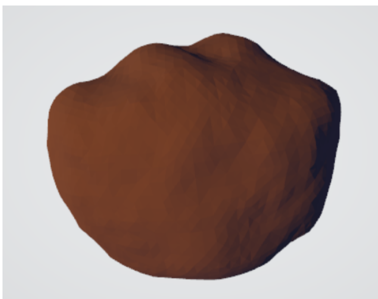

Fig. 3. Asteroid 2000 ET70's shape model containing 4000 vertices and 7996 faces (Naidu et al., 2013) (scale 1:68000)

similar to the Milani and Juventas CubeSats of the HERA mission that will visit the Didymos system (Topputo et al., 2021). It is given an SRP reference area of 0.2 m^2 and SRP coefficient $C_R = 1.1$, representative of present day spacecraft designs (Peter et al., 2020).

4.2 *Uncertainties*

In this work, the uncertainties in the asteroid's rotational parameters, β, λ and T_{ast} (Equation 2), are studied. Both uncertainties related to pre-mission scenarios and post early-characterisation phases are studied. The pre-mission scenario entails that an asteroid has not been visited yet, but Earth-based radar observations are available that constrain the asteroid's size, shape and rotation. The post early-characterisation phase has better constrained asteroid properties, because of the availability of optical spacecraft observations of the asteroid. These are still from relatively far away, though, such that the irregular gravity field has not been constrained.

Firstly, the effects are studied for three orbits, as presented in subsection 4.3, over 5, 15 and 30 days. This includes a realistic time period (5 days) between real mission trajectory corrections and allows for analysing the long-term and non-linear effects of these uncertainties (15 and 30 days). This analysis is performed considering the pre-mission scenario, involving relatively large uncertainties, that follow from Earth-based radar observations, made during a close flyby to Earth of the asteroid. These are obtained from Naidu et al. (2013) and are expected to result in significant non-linearity and dispersion in the trajectories. Thereby, this analysis gives both insight in the dynamical effects of rotational state uncertainties and in the functioning of NIPC in this application.

Secondly, this analysis is put into perspective by an analysis of the same pre-mission uncertainties in β and λ and an uncertainty of 1% in the asteroid's mass, or gravitational parameter. Mass uncertainties have been studied before by Feng et al. (2022) and Fodde et al. (2022) and can show significant dispersion and non-linearities. They should therefore allow for a qualitative comparison. Although the 1% uncertainty does not correspond to the pre-mission scenario of this asteroid (which would be $> 15\%$), it is more representative of binary asteroids which can be more accurately characterised through their mutual orbits (Naidu et al., 2020). In addition, the mass uncertainty is anticipated to yield significantly larger trajectory dispersions than the rotational state parameters, thus the smaller value was also partially chosen to make the effects due to both mass and rotation distinguishable and to be able to study this case efficiently with a low order polynomial. It must be realised, therefore, when interpreting the results, that the mass uncertainty of a single asteroid is typically > 15 times larger and that the relative contribution changes accordingly.

Thirdly, the rotational state parameters are studied with post early-characterisation uncertainties. These uncertain magnitudes are substantially smaller than their pre-mission counterparts, but their exact values will depend on the specific mission planning, especially on the orbital distance to the asteroid. Nonetheless, already at still large orbital distances from the asteroid, optical observations can fix the rotational state parameters with great accuracy. Estimates for the OSIRIS-REx mission to Bennu (Lauretta et al., 2019) and the impact mission to Didymos (Zannoni et al., 2017) show uncertainties in the order of 0.1-0.25° for the rotation pole orientation in this phase. The conservative upper value is used in this work. Similarly, optical observations can fix the rotation period with greater accuracy than radar observations. Optical observations were used to fix 2867 Stein's sidereal rotation period to 0.00002 hr (Lamy et al., 2008) and that of Bennu and Eros to 0.000002 hr (Lauretta et al., 2019; Yeomans et al., 2000). It was decided to use a conservative rotation period uncertainty of 0.00001 hr in this work. These uncertainties are studied within a broad grid of initial states at orbital distances of 2.5 km, 5 km and 10 km, to study which orbital geometries are more robust against these uncertainties. This study is performed over 5 days only, because this scenario comes close to the actual mission operations where maneuvers will be executed after a similar period. In addition, this relatively short propagation time allows for the study for many different initial conditions to still be performed efficiently with a low polynomial order. The smaller uncertainties are used, because they relate to the values actually present during a detailed characterisation phase, which is typically the mission phase for the considered altitudes (Lauretta et al., 2017).

Finally, the interactions between the rotational state parameters and the degree 2 SH coefficients are studied. This could provide insights into which components of the irregular gravity field, as indicated by Equation 2, contribute more to the propagation of the rotational state uncertainties to the orbital motion. This analysis could potentially explain the results of the previous analyses. Although the asteroid's shape will be fixed with much greater accuracy, uncertainties in the SH coefficients still persist, due to density heterogeneity inside the asteroid. This uncertainty has not been reduced in the foregoing mission phases, because the CubeSat is still too far to estimate the SH coefficients well. As such, SH uncertainties arising from the uncertain interior density distribution are used as values for the post early-characterisation phase. Only SH coefficients of degree 2 are considered here. These are directly related to the asteroid's inertia tensor and can therefore be estimated to constrain the body's interior. Degree 1 coefficients are much less uncertain, because they can also be well estimated from optical observations over a sufficiently long time. The rotation pole can be identified from a time sequence of optical observations, while the center of figure can be computed geometrically for each individual observation as well. The offsets between the two in various directions are direct measures of the degree 1 coefficients, as the center of mass lies on the rotation pole by definition. Degree 3, and higher, coefficients are expected to have significantly less effect on the orbit, because of the $\left(\frac{R}{r}\right)^n$ term, with $R < r$, in Equation 2. The degree 2 SH coefficients uncertainties were obtained from a study on Phobos (Le Maistre et al., 2019), where many of the nominal SH coefficients are similar to those in this work. It was assumed, however, that unlike Phobos, the asteroid has no large crater. Therefore, the heavily fractured and compressed porous interior models are unlikely and thus not considered here, yielding slightly smaller uncertainty magnitudes. The uncertainty for $\bar{S}_{22}$ was not studied by Le Maistre et al. (2019), because it is nearly zero by definition for Phobos orbiting Mars with synchronous rotation. This is not the case for the asteroid in this work and the uncertainty $\bar{S}_{22}$ was therefore set equal to that of $\bar{C}_{21}$ and $\bar{S}_{21}$.

Table 3. Uncertainty magnitudes (given as half the uniform range)

Uncertainty	Nominal	Pre-mission	Early-charact.
β, λ	$-50°, 80°$	$\pm 10°$	$\pm 0.25°$
T_{ast}	8.96 hr	$\pm$0.01 hr	$\pm$0.00001 hr
$\bar{C}_{20}$	Appendix A	-	$\pm$0.0050
$\bar{C}_{22}$	Appendix A	-	$\pm$0.0030
$\bar{C}_{21}, \bar{S}_{21}, \bar{S}_{22}$	Appendix A	-	$\pm$0.0015
M	$1.214 \cdot 10^{13}$ kg	-	$\pm 1\%$

The uncertain parameters in this work are assumed to have uncorrelated uniform distributions. This is largely because of the lack of knowledge on more details of the distributions of these quantities. In addition, using uniform distributions removes the possibility to sample extreme outliers, as the case for Gaussian distributions, which is anticipated to be disadvantageous for the NIPC performance. It means that ChaosPy automatically employs Legendre polynomials to achieve the most optimal convergence rate. The uncertain magnitudes of the studied parameters are given in Table 3 as half of their uncertainty range, in a sense similar to the definition of one standard deviation.

4.3 Orbits of interest

The detailed sensitivity analysis requires nominal orbits to be studied. These should start from initial conditions in different orbital regimes to allow for distinguishing between the effects in these regimes. In addition, it is required that these orbits remain bounded to the asteroid and close to their original orbit over a sufficient time span. This both guarantees that the effects that are observed belong to the orbital regime that the CubeSat is started out in and represents a realistic scenario in the case multiple CubeSats are employed to study an asteroid.

Ideally, periodic orbits would be considered, but these do not exist due to the highly irregular gravitational field and SRP. It was therefor opted to seek for orbits that are close to periodic, thus which remain close to their initial orbit parameters, for a

Table 4. Initial conditions in the asteroid's body-fixed frame of initial epoch

Orbit nr	a [m]	e [-]	i [°]	ω [°]	Ω [°]	θ [°]
1	2678.26	0.126	178.42	57.2	52.0	317
2	5147.11	0.050	92.2	286.9	254.4	130.4
3	11197.54	0.053	86.8	70.2	72.5	294.1

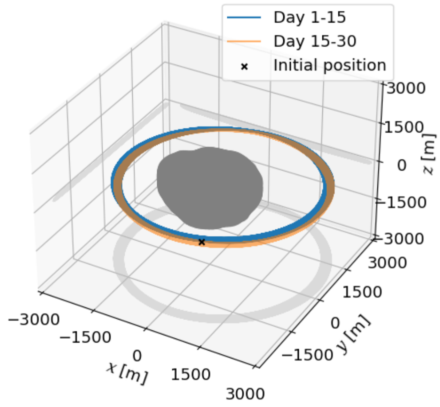

(a) Orbit 1 (clockwise travel direction)

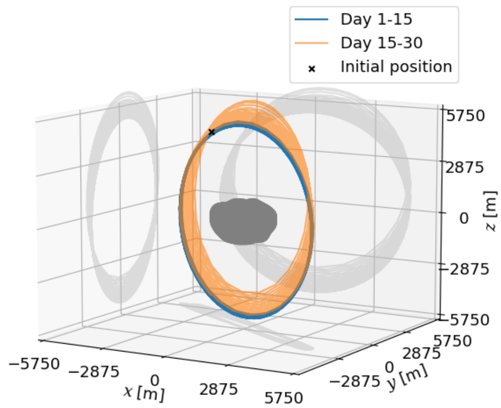

(b) Orbit 2 (clockwise travel direction)

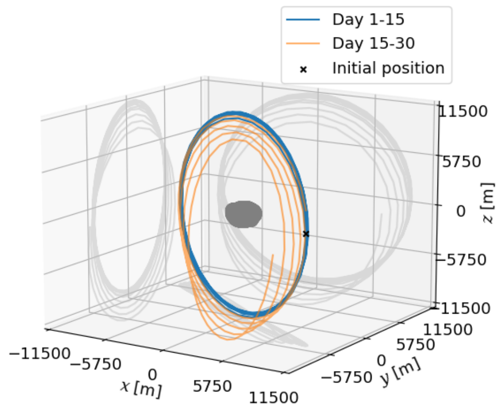

(c) Orbit 3 (counter-clockwise travel direction)

Fig. 4. Nominal orbits

period of 15 up to 30 days. Usually, orbit maneuvers are performed more regularly, so this should allow for sufficient detail in the analysis considering real mission scenarios.

Three bounded orbits were sought, with semi-major axes of about 2.5 km, 5 km and 10 km and ideally low eccentricities. Monte Carlo simulations were performed for a small range of semi-major axes around each of the three values and with the full ranges of i and Ω. The position and velocity differences with respect to the initial state were computed after one full revolution. Regions in the state-space where these differences are low are closer to periodic. Additional Monte Carlo simulations were then performed in these regions, including variations in e, ω and θ. Some orbits with low position and velocity differences were taken and an attempt was made to improve them via differential correction to the initial state. This did not result in systematically improved orbits, because of the high non-linearity of the dynamics. Especially when applying the correction for state deviations after several full orbits, which was also tried for improved long-term behaviour, this procedure broke down. Nonetheless, good nominal orbits were found for different orbital regimes, with initial conditions given in Table 4 and an initial epoch of midnight 19 February 2031. They are shown in Figure 4. Orbit 1 is retrograde equatorial and orbit 2 and 3 are polar orbits, with Ω values about 180° apart. Such orbits are also beneficial for maximizing the scientific return of the asteroid (Fayolle, 2020).

4.4 Dynamical model settings

The rotational state parameters only indirectly affect the accelerations experienced by the CubeSat. They affect the gravitational field orientation and its change over time, which in turn affects the gravitational acceleration (Equation 2). Orbits close to the asteroid feel more of the irregular gravity field than orbits farther away. Therefore, these orbits closer by require higher fidelity models of the asteroids gravity field, by using higher degree and order SH terms. However, the gravitational acceleration for orbits farther away are smaller and these may require the inclusion of other perturbations, such as third body point masses, to obtain sufficient accuracy in the orbit computation. However, because of the indirect effect of the asteroid's rotation on the CubeSat's orbit, it is more important to include higher degree and order SH coefficients than to include every single third body perturbation. Similarly, it has been argued in the foregoing subsections that uncertainties in SH coefficients can be large. If they are larger than their nominal values, their nominal values could be set to zero, because the effects of their uncertainty could then still be captured properly. However, for the revelation of the effects of rotational state uncertainties, it is beneficial to use non-zero nominal values. As mentioned in section 2, it is realised that the current work is a sensitivity analysis, which means that it is not strictly about absolute accuracy in single orbit computations, but merely about accuracy in the orbit deviations when varying uncertain parameters. A perturbation like SRP is not directly linked to the asteroid's rotational state parameters, but its effects may change as orbits deviate under these uncertainties, for example by varying the eclipse duration or via other non-linearities. This perturbation is therefore considered important. Similarly, a third body perturbation does not change directly under the asteroids rotational state uncertainties. However, as an orbit deviates under this uncertainty, the third body acceleration changes accordingly and may cause further deviations. Under these considerations and having compared, through step-wise increments in model fidelity, the influence of several perturbations on the CubeSats position, the following accelerations settings were selected for the three orbits:

- Orbit 1: SH up to degree 5 and order 5 and Cannonball SRP.
- Orbit 2: SH up to degree 2 and order 2 and Cannonball SRP.
- Orbit 3: SH up to degree 2 and order 2, Cannonball SRP and Sun PM.

The reason for including the Sun PM for orbit 3 is that, at this orbital altitude, this perturbation yields a 15 m trajectory deviation after one orbit, while it remains below 10 m after 30 days for orbit 1 and 2. It was anticipated that this could be sufficient to change the nominal orbit 3 such that the deviations under rotational state uncertainty could very well be different.

The integration settings were selected to yield 10^{-1} m accuracy after 30 days, as elaborated upon already in section 2, which is sufficient to allow for distinguishing physically different orbits. The RKDP-8(7) integrator was used, with fixed step sizes of 3000 seconds and 9000 seconds for orbit 2 and 3, respectively. For orbit 1, however, a variable step size integrator with absolute and relative tolerance of 10^{-10} was required for an accuracy of 10^{-1} m, because of the occurrence of eclipses. Similarly, the broad initial state grid analysis was also performed with this variable step size integrator for the two larger orbital altitudes, for the same reasons that eclipses occur for a significant portion of the initial states. All propagations were performed with the Cowell propagator.

Finally, the states, after being propagated according the EoM in the inertial frame $\mathcal{F}_{in}$, are transformed to and analysed in the asteroid-fixed frame of the initial epoch $\mathcal{F}_{ast}$, which is defined with the nominal rotational state parameters β_{nom} and λ_{nom} as follows:

$$\mathcal{F}_{ast} = \mathcal{R}_y(\tfrac{\pi}{2} - \beta_{nom})\mathcal{R}_z(\lambda_{nom})\mathcal{F}_{in} \tag{19}$$

As such, the z-axis points along the asteroid's rotation pole. $\mathcal{F}_{ast}$ is used to give a direct meaning to the scientific observations that are made based on the orbital geometry, especially when states are also transformed to Kepler elements, and to avoid kinematic rotation effects. The latter would be introduced when the the frame co-rotates with the asteroid and if the transformations were done with off-nominal values for β and γ.

5 NIPC performance

The NIPC options available in ChaosPy were tested extensively for various uncertainties applied to the different orbits and propagation times. This section will elaborate on this study by presenting the measures that define the NIPC performance, the conclusions drawn from this study and the settings chosen for the detailed sensitivity analyses performed.

5.1 Measures of performance

The accuracy of a polynomial approximation is analysed using two measures, ζ_{RMSE} and ζ_{max}, inspired by Fodde et al. (2021). Both measures are computed for an ensemble of $N = 500$ Sobol samples, by comparing their true final positions following from a MC simulation, $\boldsymbol{r}_{l,MC}$, with their NIPC position approximations, $\boldsymbol{r}_{l,NIPC}$. The measures were slightly adjusted from the original work, because it used dimensionless state variables, which is not the case in this work. This means that taking the norm of the measures over all state variables is not appropriate. Here, only the position variables are considered. This is a valid approach as well, because throughout a trajectory, the velocity directly affects the position thereafter, and vice versa. Thus, if the velocity has been effected with large dispersion or with high non-linearity, this has also been propagated to the position coordinates. Thus, the performance in position should also be a good indicator of the performance in velocity.

$$\text{RMSE} = \sqrt{\frac{1}{N}\sum_{l=1}^{N} \|\boldsymbol{r}_{l,NIPC} - \boldsymbol{r}_{l,MC}\|^2} \tag{20}$$

$$\epsilon_{max} = \max_{1 \leqslant l \leqslant N} \left(\|\boldsymbol{r}_{l,NIPC} - \boldsymbol{r}_{l,MC}\|^2\right) \tag{21}$$

$$d_{mean} = \frac{1}{N}\sum_{l=1}^{N} \|\boldsymbol{r}_{l,MC} - \frac{1}{N}\sum_{k=1}^{N} \boldsymbol{r}_{k,MC}\| \tag{22}$$

$$\zeta_{RMSE} = \frac{\text{RMSE}}{d_{mean}}, \quad \zeta_{max} = \frac{\epsilon_{max}}{d_{mean}} \tag{23}$$

Firstly, the Root-Mean-Squared Error (RMSE) is used as a measure for the overall performance, as given by Equation 20. Secondly, the maximum error ϵ_{max} within this ensemble of 500 samples is used as a measure for the largest outlier, i.e. the sample that is approximated worst, as given by Equation 21. The performance measures, ζ_{RMSE} and ζ_{max}, are then given as a fraction of the mean distance d_{mean} of the 500 MC samples to the mean position of this ensemble, as given by Equation 22. The use of these fractions is motivated by the fact that the accuracy of the NIPC approximation of individual samples may be lower if the spread in the MC ensemble is large, because this will have less influence on the final statistical quantities of the ensemble. If the spread in the MC ensemble is small, the NIPC approximation of individual samples needs to be more accurate to obtain sufficiently accurate statistical information for the ensemble. Here, the idea is that this required accuracy can be determined relative to the spread in the MC ensemble.

NIPC will also be applied to different element sets, such as the

Kepler elements. Again, the Cartesian position elements can be used to verify the performance, because of the direct transformation that exists between the element sets.

5.2 Conclusions on settings

The performance of NIPC was studied for the three orbits and three propagation times with different numbers of uncertainties and corresponding magnitudes with a wide variety of setting combinations from the ones listed in Table 1.

This process was started with testing the performance of the different methods for computing the PCE coefficients for simple cases. A simple case is in this regard one with low non-linearity and dispersion. Subsequently, the non-linearity and dispersion was increased, by increasing the propagation time and decreasing the orbital altitude, which complicates the PCE construction. Simultaneously, the variety of settings that was tested was incremented, first by testing different sampling/quadrature rules and subsequently applying Smolyak sparse grids and normal and cross-truncated polynomials. For many PCEs, the NIPC approximation ensembles were visually compared to the true MC ensembles. This gave insight in the values for ζ_{RMSE} and ζ_{max} that are required for sufficiently accurate approximations. In general, the NIPC performance is heavily dependent on the orbit and propagation time considered and iterations over various settings were often required for individual cases in order to find good settings. Nonetheless, some general guidelines were found as well. The most important conclusions, which more or less hold in general, that were drawn from this study and were used as guidelines for determining the detailed sensitivity analysis settings are listed:

- $\zeta_{RMSE} \leqslant 0.01$ and $\zeta_{max} \leqslant 0.1$ result in quantitatively accurate NIPC approximations and statistical information.
- PCQ converges for fewer samples than PSP. Where PSP converges to smaller ζ_{RMSE}, PCQ converges to smaller ζ_{max}, but differences are minimal.
- The choice of quadrature rule can improve performance by a factor two in ζ_{RMSE} and even more in ζ_{max}.
- PCR can outperform PCQ for five or more uncertain parameters

The better performance for certain quadrature rules, such as the Gaussian quadrature rule, could be explained by the fact that its nodes are located at the the zeros of polynomials that are orthogonal to a PDF weighting function. Thereby it minimises the error (Eldred, 2009).

In addition, it was observed that the computation time required to compute the PCE coefficients scales exponentially with the polynomial order. It was encountered for a case with 8 uncertainties and a 7$^{\text{th}}$ order polynomial that this computation took almost two hours, without considering the time for propagations. This is unworkable when multiple of such analyses have to be performed in order to tune the settings and guarantee accuracy.

Table 5. NIPC settings used

$\boldsymbol{\xi}$	**Method**	**p**	**Sample rule**	N
β, λ, T_{ast} Pre-mission / β, λ, M (1%) Pre-mission	PCQ	5	Gaussian	125 (q=4)
β, λ, T_{ast} Early-char.	PCQ	3	Gaussian	27 (q=2)
β, λ, T_{ast}, $\bar{C}_{2m}, \bar{S}_{2m}$ Early-char.	PCR	3	Hammersley	495 (3(P+1))

5.3 Settings used

Based on the analyses performed and the conclusions drawn, settings were chosen for the cases that are studied in this work. Table 5 provides the final choice of NIPC settings used for the analyses that are performed and presented in section 6. Subsequently, Figure 5 presents the corresponding NIPC performance when these settings are used for the case with pre-mission uncertainties for β, λ and T_{ast}. The performance for orbit 1 propagated for 30 days does not reach the recommended accuracy. Still these settings were used, because the increase in polynomial order, and thus the required number of quadrature nodes, was considered too large to reach the recommended accuracy. Nonetheless, as shown by a comparison to cases with sufficient accuracy in Figure 6, the NIPC approximation still matches the qualitative behaviour of the MC ensemble quite well and thus qualitative conclusions can still be drawn from this analysis. The NIPC performance for the analysis including mass uncertainties and the cases with early-characterisation uncertainties all have $\zeta_{RMSE} < 0.007$ and $\zeta_{max} < 0.04$ for propagation times of 5 days. Only one special case that was investigated, which includes uncertainties in the degree 2 SH coefficients and undergoes large dispersions, has $\zeta_{RMSE} = 0.02$ and $\zeta_{max} = 0.2$. Although larger than advised, they are sufficient to obtain qualitatively accurate Sobol' indices for this analysis as well.

6 Results and discussion

In this section the results of the detailed sensitivity analyses, performed with the settings given in the previous section, are presented and discussed, as summarised in Figure 2. First, subsection 6.1 elaborates on the analysis of pre-mission uncertainties in β, λ and T_{ast}. It provides a comparison of their effects on the different orbits, as well as the relative contribution by each parameter. Subsection 6.2 explains some of the remarkable results of the foregoing analysis. Subsequently, subsection 6.3 puts that analysis into perspective by comparing the contribution of uncertainty in β and λ to that in the asteroid's mass. Then, subsection 6.4 presents a broader analysis of initial states to study which orbital geometries are more robust

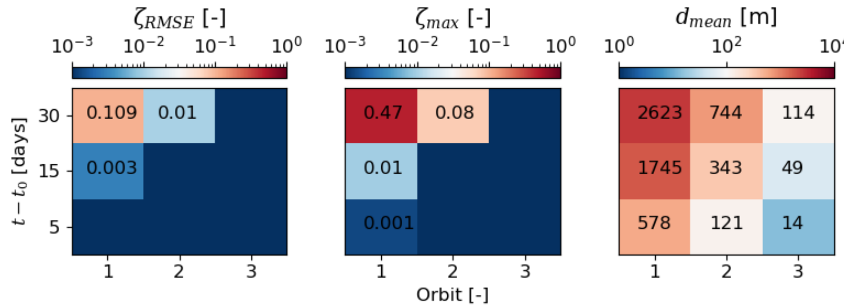

Fig. 5. NIPC performance for: PCQ, $p = 5$, Gaussian quadrature, $q = 4$ and pre-mission uncertainties for β, λ and T_{ast}

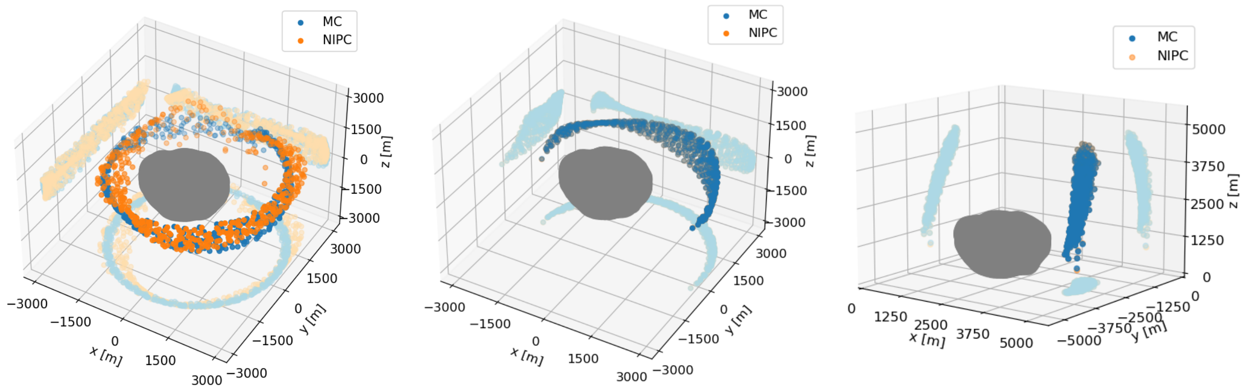

(a) Orbit 1 after 30 days

(b) Orbit 1 after 15 days

(c) Orbit 2 after 30 days

Fig. 6. Final position of 500 MC samples and their NIPC approximations (corresponding to Figure 5)

against rotational state uncertainties. This is done with early-characterisation uncertainties, because these are more representative of the actual mission phase at these altitudes. Finally, subsection 6.5 presents a brief analysis of the interaction between rotational state parameters and irregular gravity field components, in an effort to explain the results of subsection 6.4.

6.1 Sensitivity to rotational state uncertainties

The maximum uncertainty indicator among the Cartesian state elements is shown in Figure 7, subject to pre-mission uncertainties in β, λ and T_{ast}. σ^2 and S_{p+1} (Equation 14) increase systematically with propagation time and decrease with orbital altitude. Longer exposure to the uncertainties makes the dispersion build up, adding to the dispersion from the earlier phase. Similarly, as larger regions of the state-space are encountered, more non-linear effects in the dynamics emerge. α shows the same pattern for orbit 2 and 3, meaning that, relative to the time period considered, the variance grows more rapidly as propagation time increases. On the contrary, α reduces from 15 to 30 days for orbit 1. Looking at Figure 6a and 6b, though, it is observed that the range of attained x values is similar, while the spread of the MC ensemble does grow. This is because the ensemble stretches around the asteroid. Thus, while σ_x^2 remains nearly equal, α reduces. It is therefore not possible from these results to determine whether there is also a relatively larger increase in the dispersion in the final half of the propagation time. This is partially a result of the dispersion being mainly in an angular direction, rather than in the radial direction. Similarly, it is observed that the dispersion in the z-coordinate is similar for the two propagation times. Thus, it does not increase further in the latter half. However, where in the x-coordinate this is observed because the maximum range of values was already attained, in the z-coordinate the dispersion indeed stagnates. As such, to fully study the dispersion over multiple propagation times, there is a need to analyse the indicators for all state variables or define an indicator that takes into account all state variables, rather than taking the maximum indicator. On the other hand, this motivates the change to Kepler elements. Analysing any one of them separately could give meaningful insight in a particular aspect of the orbital geometry, while this is not the case for the Cartesian elements.

Before analysing Kepler elements, the relative contributions of β, λ and T_{ast} on the dispersion of the orbits are analysed. Figure 8 shows the total order Sobol' indices for the Cartesian element with maximum variance for each of the three orbits after 5 and 30 days. The total order Sobol' index is defined similar to Equation 12, but then by summing the contributions of all PCE terms containing the parameter of interest, thus of all

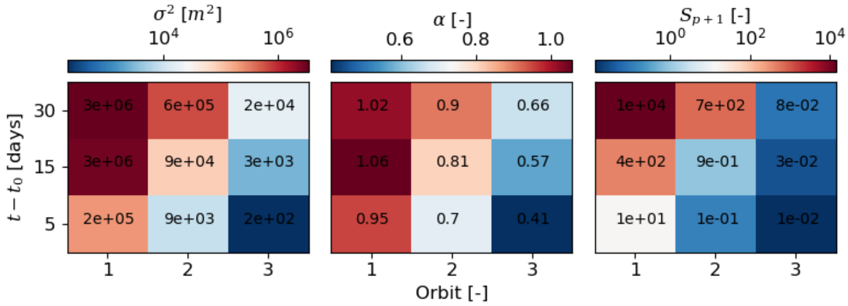

Fig. 7. Maximum value of uncertainty indicators among all Cartesian state variables (β, λ and T_{ast} with pre-mission uncertainties)

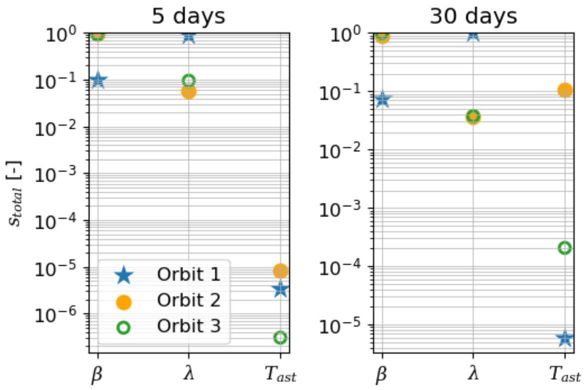

Fig. 8. Total order Sobol' indices for the Cartesian element with maximum variance

orders. It is observed that β and λ contribute significantly more than T_{ast} to the orbit dispersion for all three orbits after 5 days. Similar indices are found for orbit 1 after 30 days as after 5 days, while for orbit 2 and 3 the index of T_{ast} has increased by several orders of magnitude. It is logical that the contribution of T_{ast} increases with time, because a change in this parameter requires time to build up a difference in the asteroid's orientation. Where a change in β and λ cause an difference in the asteroid's orientation at t_0, T_{ast} does not. It is not clear whether this increase is not observed for orbit 1 because it lies closer to the asteroid or because it is retrograde equatorial, or because of both.

Figure 9 shows the distances d_a, d_e and d_i as defined in subsection 3.3. It is noteworthy that d_i shows a large increase for orbit 1 compared to orbit 2 and 3. This is because orbit 1, being nearly retrograde equatorial, lies within the equatorial plane with the largest gravitational bulges ($\bar{C}_{20}$ and $\bar{C}_{22}$) (Figure 4a). Changes in the rotation pole orientation cause these planes to rotate apart. However, the equatorial gravitational bulges pull them together again, thereby changing the inclination, as shown in Figure 11. Depending on the change of the rotation pole, the inclination departs from $180°$, but also approaches it again between 20 and 25 days for all samples. The time history shows that the dispersion in i is heavily dependent on the time chosen. As orbit 2 and 3 lie perpendicular to the equatorial plane, they do not experience this effect as much.

For d_a and d_e it is noteworthy that their values after 30 days are larger for orbit 2 than for orbit 1. The time histories of $\Delta a = a - a_{nom}$ and $\Delta e = e - e_{nom}$, with a_{nom} and e_{nom} being the semi-major axis and eccentricity of the orbit with the nominal rotation parameters, respectively, of 500 samples are shown in Figure 12. They show that for orbit 1 large deviations emerge already from the early phase of the orbit, while for orbit 2 these increase over time, especially in the latter 15 days. In addition, although the magnitude of Δe after 30 days of orbit 2 is similar to that of orbit 1, the larger value of the semi-major axis causes a larger distance d_e (Equation 17).

d_a, d_e and d_i were expected to generally increase with propagation time. This is not observed for d_i of orbit 1, which is in line with the limited dispersion of the z-coordinate (Figure 6) and the time history of i (Figure 11). It is, again, a result of the orbital plane nearly coinciding with the asteroid's equatorial plane, containing the largest gravitational bulges. The same is observed in the similar magnitudes for the corresponding non-linearity index shown in Figure 10. On the contrary, clear increases in S_{p+1} are observed for a and e with increasing propagation time and decreasing orbital altitude.

It is concluded that, in general, dispersion and non-linearity increase with propagation time and decrease with orbital altitude. However, for specific orbital elements, such as the inclination of equatorial orbits, the effects of rotational state uncertainties can be more unpredictable and can depart from this trend. Also the orbital geometry affects the degree of dispersion and non-linearity.

6.2 *Singularities in the Kepler elements*

Figure 13 shows the distances d_ω, d_Ω and d_θ. It is observed that the contributions in the state dispersion is larger for these elements, than in a, e and i. This is in line with the foregoing results in the Cartesian elements, which showed mostly angular variations and little radial variations. Here, the decrease with orbital altitude is more obvious than the increase with propagation time. The same patterns were obtained for the non-linearity in-

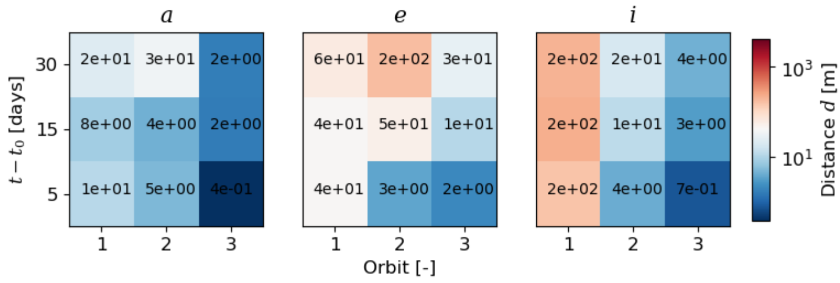

Fig. 9. Distance between the expected orbit and the orbit at 1σ (β, λ and T_{ast} with pre-mission uncertainties)

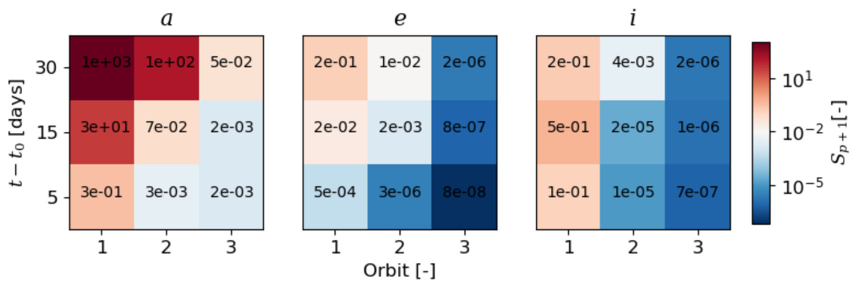

Fig. 10. Non-linearity indices for semi-major axis, eccentricity and inclination (β, λ and T_{ast} with pre-mission uncertainties)

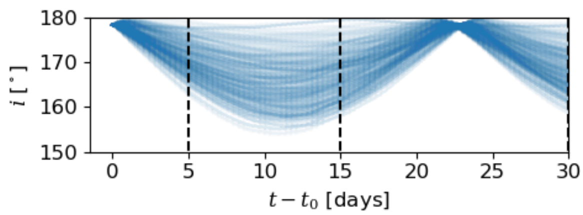

Fig. 11. Time history of inclination of 500 samples for orbit 1 (corresponding to Figure 9 and 10)

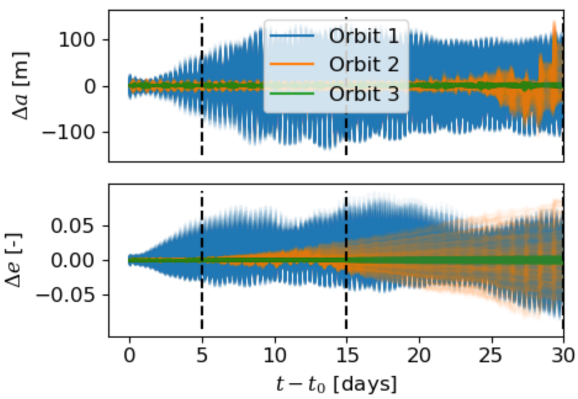

Fig. 12. Time history of Δa and Δe of 500 samples (corresponding to Figure 9 and 10)

dex as for the distance d of these elements. Two aspects of these patterns stand out.

Firstly, ω and Ω have nearly equal distances for all propagation times for orbit 1. As shown in Figure 14, both quantities encounter a discontinuity, in the following referred to as the 'torn discontinuity', because the response looks like a plane with a tear in it. These are impossible to filter, because both quantities attain values in the full range from $0°$ to $360°$. It is remarkable that this torn discontinuity arises where i approaches $180°$. The time histories of ω and Ω of some samples close to the torn discontinuity were studied and show jumps from $0°$ to $360°$, or vice versa. Other samples do not, or at different times. Some samples make such jumps just before a certain time, others make it just after. This results in the torn discontinuity that is observed. Moreover, it means that the location of the torn discontinuity in the uncertain domain is not fixed, but changes with time. Although these jumps do not strictly occur when the inclination is very close to $180°$, large changes in ω and Ω are always observed when this is the case. It is therefore the reason that the jumps are encountered eventually. Thus, the torn discontinuity arises, because the orbit is retrograde equatorial, thereby approaching the singularity in Ω and yielding large variation in ω and Ω.

To avoid the torn discontinuities in ω and Ω one can use other elements sets. The Cartesian elements studied before can be used, but to reveal information about how the orbital geometry changes one must transform them to Kepler elements after constructing the PCE. The disadvantage here is that none of the

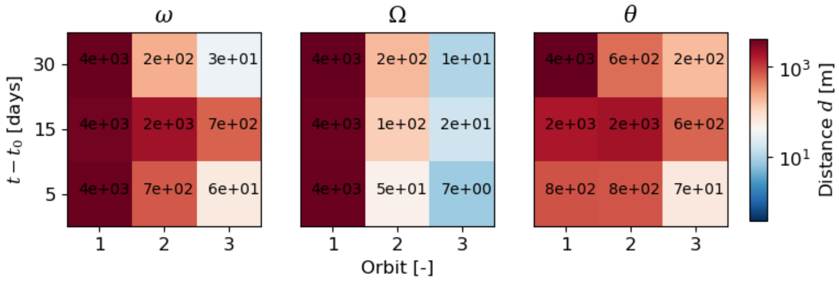

Fig. 13. Distance between expected orbit and 1σ orbit (β, λ and T_{ast} with pre-mission uncertainties)

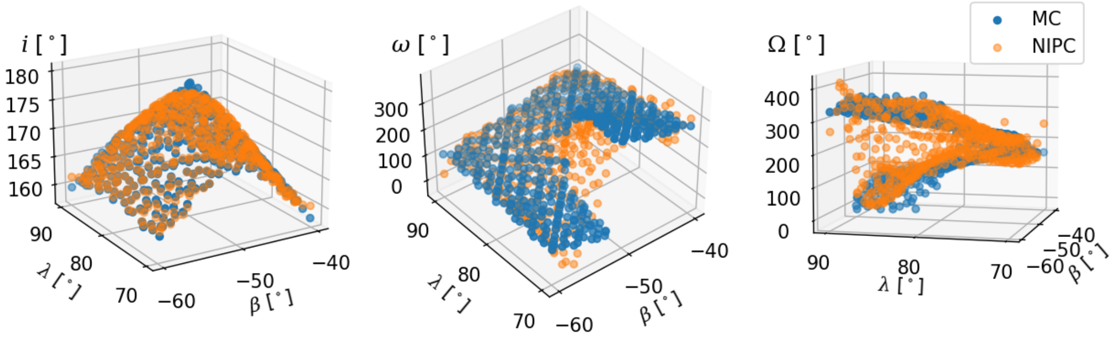

Fig. 14. Discontinuities in the MC ensemble of ω and Ω for i approaching $180°$, causing a bad NIPC approximation, for orbit 1 propagated for 15 days (β, λ and T_{ast} with pre-mission uncertainties) (dependence on T_{ast} left out for visualisation purposes)

statistical information contained in the PCE can be used anymore. Another possibility is to use Mean Equinoctial Elements (MEE). This set combines multiple Kepler elements in each element, and one of two variants can be used, depending on the inclination value, to avoid singularities. This comes at the cost of a reduction in the ease of interpreting the individual elements. Figure 15 shows the response surfaces of $f = e\cos(\omega - \Omega)$, $k = \cot\left(\frac{i}{2}\right)\sin(\Omega)$ and true longitude $L = -\Omega + \omega + \theta$, revealing that no discontinuities are present.

Secondly, ω and θ have large distances for orbit 2 propagated for 15 days, compared to 30 days (Figure 13). As shown in Figure 16, this larger variation is due to a non-linearity encountered near an edge of the uncertain domain, corresponding to very small e. Here, approaching the singularity of a circular orbit, for which ω is undefined, causes it to show large variations. Although there is no discontinuity in this case, it could be that one is present just outside the studied domain. As the eccentricity increases in the latter 15 days, there is less variation in ω there.

It is noted that this does not mean that the actual size of the MC ensemble, in Cartesian space, is larger for 15 days than for 30 days. There are strong, mostly negative, correlations between ω, Ω and θ. As such, a variation in one of the elements, is accompanied by a variation in the others, which could (partially) cancel the corresponding change in position.

The NIPC performance in ω, Ω and θ is thus highly susceptible to the singularities in the definition of the Kepler elements. It must be realised that these effects would also appear when other non-linear uncertainty propagation methods are used. That is, they originate from the element set definition, rather than from the non-linear dynamics or the NIPC method. Since equatorial and circular orbits form a major group of the orbits that are of scientific interest, there is a limited use of ω, Ω and θ in non-linear uncertainty propagation. Even if non-equatorial and non-circular orbits are studied, it is not guaranteed that they will not approach such cases under uncertainty during longer time periods, due to the highly non-linear dynamics.

6.3 *Comparison to mass uncertainty*

The effects of uncertainties in the rotational state parameters were compared to the effects of mass uncertainties, which was researched by Feng et al. (2022) and Fodde et al. (2022) and shows various degrees of dispersion and non-linearity for different initial conditions. To this end, the first order Sobol' indices s_1 (similar to Equation 12) were studied of an analysis including a 1% uncertainty in the asteroid's mass M and pre-mission uncertainties for β and λ. T_{ast} was left out, as it was found at the end of subsection 6.1 to have significantly less effect on the orbit dispersion. The Sobol' indices are shown for the Cartesian element with maximum variance, a, e, i and Ω (orbit 2 and 3 only, which do not experience the torn discontinuity) for a propagation time of 5 days in Figure 17. Some aspects are observed from the Sobol' indices, as discussed next.

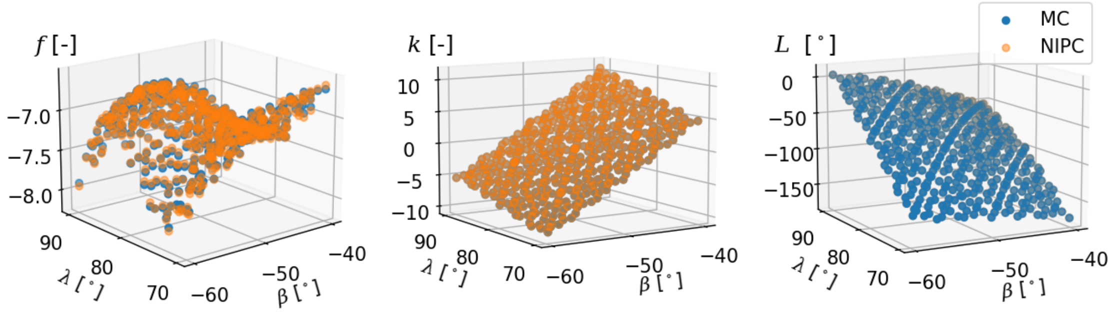

Fig. 15. NIPC for Mean Equinoctial Elements, orbit 1 propagated for 15 days

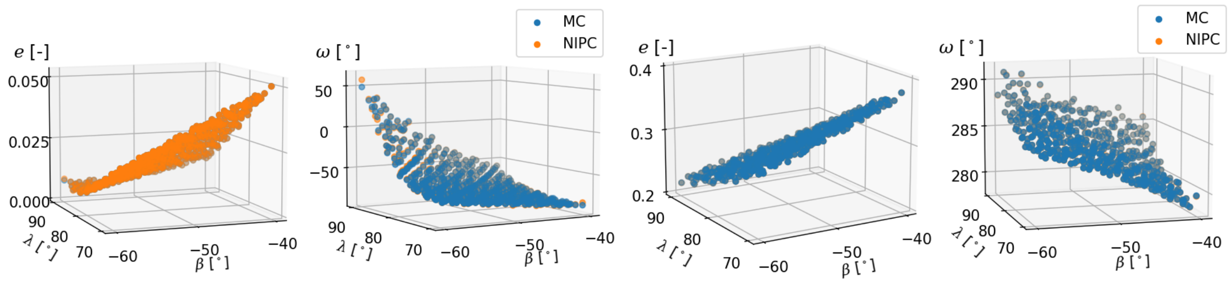

(a) After 15 days

(b) After 30 days

Fig. 16. ω and e values for orbit 2 (corresponding to Figure 13) (Note that, in addition to β and λ, also T_{ast} is uncertain here, but is left out for visualisation purposes)

First and foremost, M has clearly the largest contribution on the Cartesian element for all orbits, with a difference of almost two orders of magnitude compared to β and λ. Thus, in general, mass uncertainty affects the orbital motion much more than rotational state uncertainty.

Secondly, for orbit 3 the M index is clearly the largest for the Kepler elements. The other indices are at least 2 orders of magnitude smaller for a, and 3 orders of magnitude smaller for the other elements. For the orbits closer to the asteroid, the β and λ indices become larger. Still, it is only for e, i and Ω that the β and λ indices take on values of the same or a higher order of magnitude as the first order M index. This shows that for low orbital altitudes it is more important to consider the effect of rotational state uncertainties than for higher orbital altitudes. Moreover, depending on which orbital elements need to be analysed, they may be equally, or even more, important as the 1% mass uncertainty.

Thirdly, the M index is low for i (and to some extent e) of orbit 1, while the first order β and λ indices are large. This is not observed for orbit 2 and 3, and is, the same as observed before for the inclination in Figure 9, because orbit 1 is nearly retrograde equatorial.

Fourthly, Ω has large first order β and λ indices for orbit 2. On the contrary, this is not the case for orbit 3, where the first order M index is largest by far. This shows that dependence of the location of the ascending node on the asteroid's rotational state reduces significantly with orbital altitude for polar orbits.

The Sobol' indices for the elements not shown in Figure 17 were studied for orbit 2 and 3 as well (for orbit 1 the torn discontinuities arose). ω shows relative behaviour very similar to e. As these orbits approach the circular orbit case in part of the uncertain domain ω is affected accordingly, as described previously. θ, though, has a first order M index that is an order of magnitude larger than the others. This is the same as observed in a and is because of their strong correlation: as a increases, the orbital period increases and θ will start to lag behind.

Other than these points, there do not seem to be clearly systematic relations between the indices. This shows that these results may very well differ if analysed over different time spans. Considering that the mass uncertainty of 1% is low for a pre-mission scenario, although not necessarily for binary asteroids, it can be concluded that the relative contribution of rotational state uncertainties is comparatively low in general for pre-mission uncertainties. Yet, significant contributions may occur in particular cases, such as i for equatorial orbits and Ω for sufficiently low polar orbits. When significant, the rotational state uncertainties have their dominant effect mostly in i and Ω and to some extent in e, while the mass uncertainty has a major effect on a and θ. Also the second order Sobol' indices were studied. In general, these are smaller than the first order indices. In some

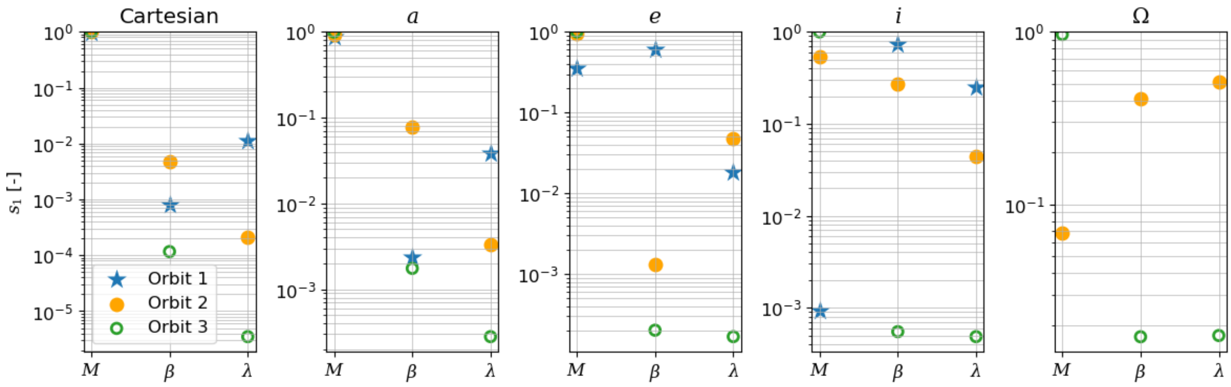

Fig. 17. First order Sobol' indices for 5 days propagation times, the Cartesian position element with the largest variance is shown (β and λ with pre-mission uncertainties, M with 1% uncertainty; Ω of orbit 1 is not shown because it encountered the torn discontinuity)

cases, though, they become equal to a first order index, but in none of the cases were they the largest contributor.

6.4 Sensitivity for different initial orbits

The knowledge gained from the results of the previous subsections was used within a broader analysis with different orbital geometries. A grid analysis in terms of i_0 and Ω_0 was conducted for the three semi-major axes. The rotational state parameters were given their post early-characterisation uncertainties, because these are the actual ones when the spacecraft is going to orbit at these altitudes. In this analysis, $e_0 = 0.001, \omega_0 = 0.001$ rad and $\theta_0 = 0$ rad, so that the initial state is always nearly the ascending node of a nearly circular orbit. The lowest considered inclination is also 0.001 rad. It was found by Feng et al. (2019a) that having an initial state closer to the asteroid's polar region increases the trajectory's dispersion, thus the following results are likely only lower bounds for the dispersion of these orbits.

The analysis was conducted only for 5 days, because it results in substantial differences between the studied cases, while keeping the computation cost low. The corresponding maximum variance among the Cartesian position elements is presented in Figure 18a for an initial semi-major axis of 2500 m. It should be noted that for some cases these values correspond to standard deviations in the order of km and thus reaches the maximum range that such coordinate attains, as also encountered for x in Figure 6a and 6b. This is against the initial expectations based on the small uncertainties and short propagation times and it was found that some of the corresponding PCEs are not accurate. Nonetheless, these results can be used, because they were verified to be accurate for all the cases that are less sensitive to the uncertainties. This only limits the relative comparison of the most sensitive regions.

It is clear from Figure 18a that the state space contains two semi-elliptical contours that are much less robust against rotational state uncertainties. These two semi-ellipses seem to be nearly symmetrical about the $\Omega = 180°$ line, and each semi-ellipse seems to be symmetrical about its center line ($\Omega = 90°$ or $\Omega = 270°$). The occurrence of these semi-ellipses is therefore thought to be a result of the interaction of the rotational state parameters with one of the largest terms of the SH gravity field, $\bar{C}_{22}$. Uncertainties in this term were also found to be more influential than those in $\bar{C}_{20}$, which is similarly large, by Feng et al. (2021). Deviations from exact symmetry could then be caused by the other, smaller, SH terms. However, if indeed the $\bar{C}_{22}$ term were the cause, the opposite results should have been expected. Evaluating the derivatives of the accelerations (i.e. the second derivatives of the potential U) caused by $\bar{C}_{22}$ with respect to the body-fixed longitude and latitude (which change under the rotational state uncertainties), shows that the acceleration changes most with changes in the rotational state at longitudes (and thus Ω_0 values) of $0°$ and $180°$. Thus, the most dispersion should be expected for these initial states, which is clearly against the results of Figure 18a. The same grid analysis was therefore performed for a duration of only 1 hour, during which the CubeSat fulfills less than a quarter of an orbit, thereby isolating the effect of the initial position. As shown in Figure 20, these results are more in line with the theoretical prediction just described, thereby verifying the results. It is therefore concluded that the large dispersions over 5 days are not necessarily a direct result of the initial states of the orbits, but also of which states they go through at later times. Moreover, as shown in Figure 19 by the time history of the orbital radius and magnitude of the gravitational acceleration of 500 MC samples for each of the four numbered cases in Figure 18a, large dispersions seem to be initialised at different times throughout the 5 day period, rather than only immediately at t_0. This also explains the fairly erratic behaviour of the variance and indicates that it might be the high non-linearity of the dynamics that cause such effects. Moreover, it can be difficult to find their root causes. As an example, consider the occurrence of eclipses. It could be that for certain initial states, a change in the rotational state parameters results in an eclipse that occurs after 2 days starting slightly later, taking slightly longer or just not happening at all. This can significantly affect the trajectory as SRP is

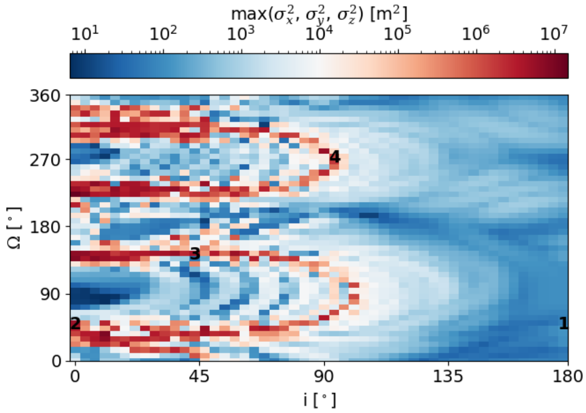

(a) Maximum variance of Cartesian position for $a_0 = 2500$ m

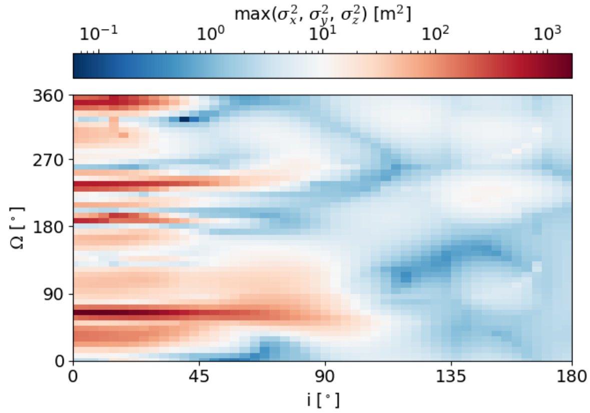

(b) Maximum variance of Cartesian position for $a_0 = 5000$ m

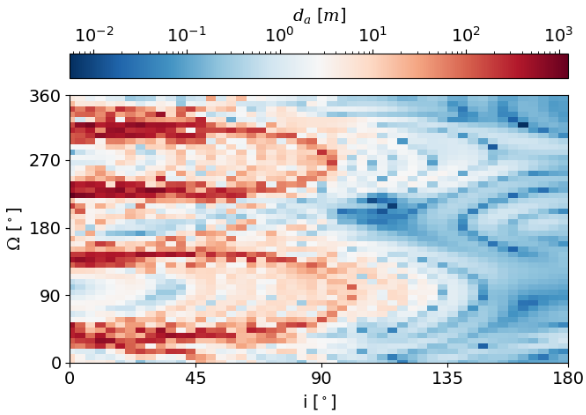

(c) Variation in semi-major axis for $a_0 = 2500$ m

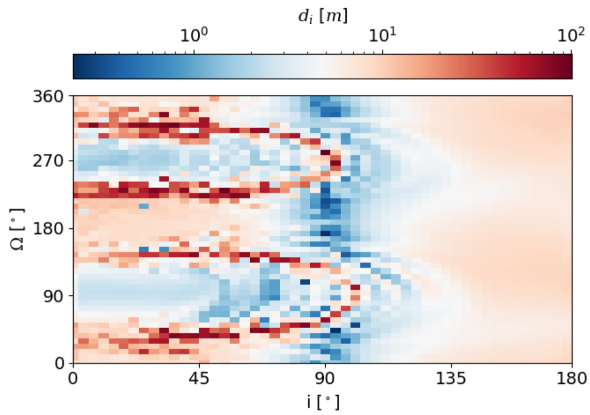

(d) Variation in inclination for $a_0 = 2500$ m

Fig. 18. Variation in trajectory dispersion after 5 days for different initial orbital geometries due to rotational state uncertainty (β, λ and T_{ast} with post early-characterisation uncertainties)

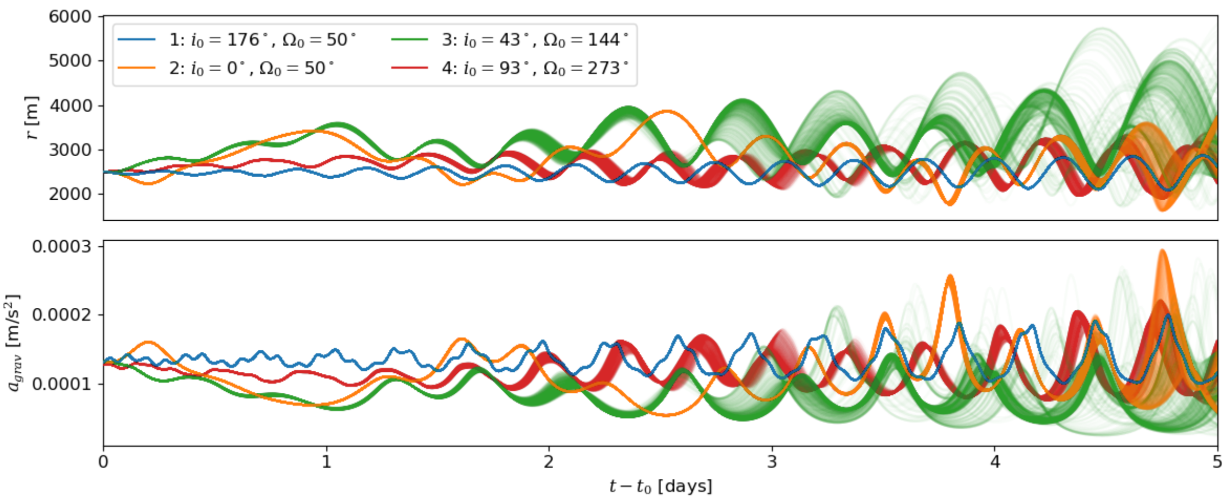

Fig. 19. Difference in orbital radius and gravitational acceleration dispersion for different initial i and Ω values (legend numbers correspond to Figure 18a)

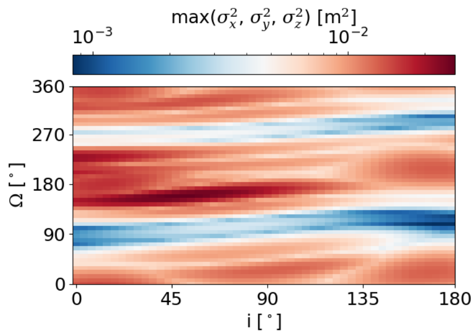

Fig. 20. Variation in trajectory dispersion after 1 hour for different orbital geometries (β, λ and T_{ast} with post early-characterisation uncertainties)

a large perturbation. A trajectory that initially undergoes larger dispersion due to the rotational state uncertainties, but does not undergo any eclipses within this uncertainty, might turn out to be more stable over the longer duration.

Retrograde orbits do not show these unstable regions, because their velocity relative to the asteroid is much bigger. Therefore, they are only exposed to large changes in the accelerations for shorter amounts of time, resulting in less dispersion in the trajectories overall. Similar to this result, retrograde orbits were found to be more robust against uncertainties in the irregular gravity field by Feng et al. (2019a and 2021). Retrograde orbits were also found most suitable for geodetic parameter estimation under uncertainty by Fayolle (2020). Thus, retrograde orbits are both easier and cheaper to maintain and they maximise the mission's scientific return under all these uncertainties. On the other hand, Feng et al. (2022) showed that polar orbits, and specifically the Solar Terminator Orbits, are more robust against mass and SRP uncertainties than equatorial and inclined orbits. This is not observed for rotational state uncertainties and it shows that different types of uncertainties can affect distinct orbital geometries in different ways.

Figure 18b shows, for a semi-major axis of 5000 m, that the results can differ a lot, likely due to the high non-linearity of the dynamics. Some of the sensitive Ω_0 regions have shifted and fade away for inclinations approaching 90°. In addition, it shows less erratic behaviour, which is a result of the lower degree of non-linearity at this larger semi-major axis. Also the relatively stronger perturbation of SRP can be causing these differences, as it was found to have significant more effect on all orbital plane orientations at higher altitudes by Feng et al. (2021).

Figure 18c and 18d show the distances between the expected orbit and the orbit at one standard deviation for the semi-major axis and inclination (d_a and d_i). Whereas both show similar patterns as Figure 18a, three clear differences are observed. Firstly, the maximum value of d_a is an order of magnitude larger than that of d_i. Thus, the dispersion under rotational state uncertainty occurs more in the semi-major axis than in the inclination. Secondly, the inclination is least sensitive for polar orbits, which is in line with the observations made in subsection 6.1 and 6.3, where i showed more dispersion due to rotational state uncertainty for orbit 1 than for orbit 2 and 3. Thirdly, d_i shows significant differences between the regions inside and outside the semi-elliptical regions, which are not observed in d_a and the maximum Cartesian variance. This indicates that regions that may not seem better in general, can be beneficial for maintaining a specific orbital element.

Similar plots were studied for e, ω, Ω and θ. Although the same patterns were found, which suggests that the torn discontinuities were not encountered for at least the least sensitive cases, one aspect stood out. The stable regions, e.g. retrograde orbits, show smaller distances for a and e than for the angular Kepler elements. Stable orbits are thus most stable in a and e.

Finally, the analysis for a 10 km semi-major axis resulted in errors less than 1 m. The rotational state uncertainties can therefore be ignored at this and higher orbital altitudes.

6.5 Interaction between rotation and the irregular gravity field

The second order Sobol' indices (Equation 12) from an uncertainty propagation including degree 2 SH coefficient uncertainties with post early-characterisation magnitudes, as well as the post early-characterisation rotational state uncertainties, were studied in another attempt to uncover the cause(s) of the semi-elliptical regions in Figure 18a. This analysis was performed for two initial states highlighted in Figure 18a: case 1 with low dispersion ($i_0 = 179°$, $\Omega_0 = 52°$) and case 3 with large dispersion ($i_0 = 43°$, $\Omega_0 = 144°$). To obtain an accurate NIPC approximation for the latter case, propagation times of 0.5, 0.8 and 1 day were studied. The dispersion difference between case 1 and 3 is then still similar to that found for 5 days.

It is observed in Figure 21 that there is not one SH coefficient that has the largest indices for all cases. This is also not the case for case 1 by itself. Whereas the λ-$\bar{C}_{22}$ index is largest for 0.5 day and 0.8 day, the β-$\bar{S}_{21}$ index becomes largest for 1 day. For case 3, however, it is the λ-$\bar{S}_{21}$ index that is largest and the λ-$\bar{C}_{20}$ index that is also large for all propagation times. Nonetheless, also for this case, the relative contributions of the other interactions differ among the different propagation times. Thus, this analysis does not allow for drawing a conclusion about the cause(s) of the semi-elliptical regions in Figure 18a. It is expected that they are caused by the combination of specific gravitational bulges that are encountered throughout the trajectories, which could also affect the occurrence of eclipses and thus the effects of SRP.

7 Conclusion

In this work the non-linear effects of the uncertainties in an asteroid's rotational state on the orbital motion of a CubeSat were studied using NIPC. Different initial orbital geometries

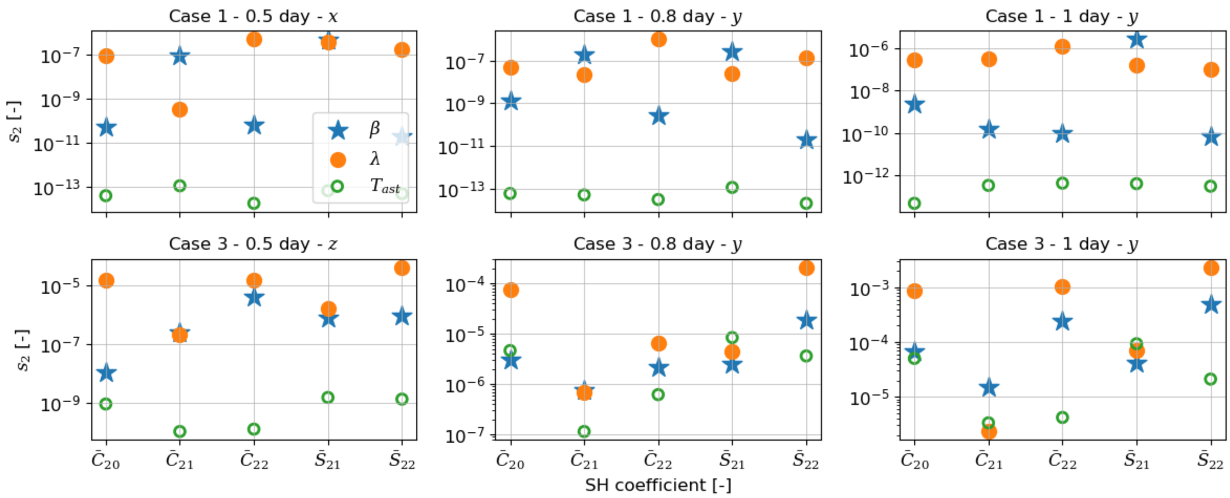

Fig. 21. Second order Sobol' indices of interactions between a rotational state parameter and a degree 2 SH coefficient (Case 1 has $i_0 = 179°$, $\Omega_0 = 52°$, case 3 has $i_0 = 43°$, $\Omega_0 = 144°$) (β, λ and T_{ast} with post early-characterisation uncertainties)

were propagated for various time periods to analyse the sensitivities of different orbital regimes and identify robust orbit solutions. Both uncertainties related to pre-mission scenarios and post early-characterisation phases were studied.

In general, the results show that dispersion and non-linearity increase with increased propagation time and decreased orbital altitude. However, an interesting case was encountered which departs from this trend. Considering a retrograde equatorial orbit, it is found that its inclination reaches maximum dispersion already within 5 days. This is due to the interaction with the gravitational bulges in the equatorial plane. Also, the uncertainty in β and λ affect the orbital motion more than uncertainty in T_{ast} over short propagation times, while the contribution by T_{ast} builds up over time and can become equally effective for some cases.

Uncertainty in the asteroid's mass in general affects the orbital motion more than those in its rotational state, but exceptions have been encountered. Considering a polar orbit at 5 km, the right ascension of the ascending node is more prone to uncertainties in the rotation pole orientation than to that in mass. From this it is concluded that, although the effects of mass are generally larger, an analysis of a specific orbital element could require the inclusion of rotational state uncertainties for reliable results.

A wide initial orbital geometry analysis has revealed that retrograde orbits, which are also most suitable for geodetic parameter estimation, are more stable against rotational state uncertainties. However, also stable prograde orbits exist for specific combinations of the initial inclination and right ascension of the ascending node. Interestingly, the unstable regions in the initial state space show symmetry that at first sight seems attributed to the $\bar{C}_{22}$ SH term, yet it does not match the theoretical prediction. Thorough future analysis should reveal the cause of this symmetry, which is expected to be the result of the specific gravitational bulges that are encountered throughout the trajectories. In addition, it is found that polar orbits are more stable against inclination changes than inclined and equatorial orbits.

These results can guide the mission design process in selecting orbital geometries that are more stable against uncertainties, thereby minimizing the fuel required for trajectory corrections. Future research could compare these results to those for different propagation times, as well as initial states near the polar regions.

Finally, this works has thus demonstrated the abilities of NIPC in its application to the non-linear propagation of uncertainties in the environment of a small solar system body. Both its effectiveness in terms of efficiency and accuracy, as well as its limitations have been observed. In this process, this work has provided insights in the possible orbit deviations due to uncertainties in the rotational state of an asteroid. Also the need to study these in detail for actual missions has been discussed. Hereby it facilitates small body mission designers in making choices for target orbits that minimise the fuel required for trajectory corrections. Ultimately, this leads to the best observations and scientific knowledge that can be used to better constrain the origins and evolution of the Solar System and to design and execute planetary defense missions.

References

Armellin, R., Di Lizia, P., Bernelli-Zazzera, F. and Berz, M. (2010). Asteroid close encounters characterization using differential algebra: the case of Apophis. *Celestial Mechanics and Dynamical Astronomy* **107**, pp 451-470.

Balmino, G. (1994). Gravitational Potential Harmonics from the Shape of an Homogeneous Body. *Celestial Mechanics & Dynamical Astronomy* **60** (3), pp 331–364.

Barucci, M. A., Dotto, E. and Levasseur-Regourd, A. C. (2011). Space missions to small bodies: asteroids and cometary nuclei. *Astronomy and Astrophyiscs Review* **19** (48).

Benson, C. J., Scheeres, D., Brozovic, M. et al. (2023). Spin state evolution of (99942) Apophis during its 2029 Earth encounter. *Icarus* **390** (115324).

Bottke Jr., W. F., Cellino, A., Paolicchi, P. and Binzel, R. P. (2002). An Overview of the Asteroids: The Asteroids III Perspective. *Asteroids III*

Cheng, A. F., Rivkin, A. S., Michel, P. et al. (2018). AIDA DART asteroid deflection test: Planetary defense and science objectives. *Planetary and Space Science* **157**, pp 104-115.

DeMeo, F. E. and Carry, B. (2014). Solar System evolution from compositional mapping of the asteroid belt. *Nature* **505**, pp 629–634.

Eldred, M. (2009). Recent advances in non-intrusive polynomial chaos and stochastic collocation methods for uncertainty analysis and design. *50th AIAA/ASME/ASCE/AHS/ASC Structures, Structural Dynamics, and Materials Conference* (2274).

Fayolle, M. (2020). Geodetic parameter estimation for small-satellite small-body missions: An uncertainty-driven approach. MSc Thesis *TU Delft Repository:* `http://resolver.tudelft.nl/uuid:b341defc-1b37-49b4-b14f-6a5a1748931b`

Feinberg, J. and Langtangen., H. P. (2015). Chaospy: An open source tool for designing methods of uncertainty quantification. *Journal of Computational Science* **11**, pp 46–57.

Feng, J. and Hou, X. (2018). The semi-analytical analysis of orbital evolution around an asteroid under the effects of the C20 term, the solar radiation pressure and the asteroid's orbital eccentricity. *Advances in Space Research* **62** (9), pp2649–2664.

Feng, J., Armellin, R. and Hou, X. (2019a). Orbit propagation in irregular and uncertain gravity field using differential algebra. *Acta Astronautica* **161**, pp 338–347.

Feng, J., Hou, X. and Armellin, R. (2019b). Survey on studies about model uncertainties in small body explorations. *Progress in Aerospace Sciences* **110**, 100549.

Feng, J., Santeramo, D., Di Lizia, P., Armellin, R. and Hou, X. (2021). Dynamical structure of the motion around asteroids with uncertain gravity and solar radiation pressure. *Acta Astronautica* **186**, pp 135–147.

Feng, J., Hou, X., Di Lizia. P., Armellin, R. and Santeramo, D. A. (2022). Sensitivity analysis of the orbital motion around 469219 Kamo'oalewa (2016 HO3) to uncertainties on asteroid mass and solar radiation pressure. *Advances in Space Research* **69** (3), pp 1602-1618.

Fodde, I., Feng, J. and Vasile, M. (2021). Uncertainty propagation for orbital motion around an asteroid using Generalized Intrusive Polynomial Algebra: application to the Didymos system. *8th International Conference on Astrodynamics Tools and Techniques*.

Fodde, I., Feng, J. and Vasile, M. (2022). Uncertainty maps for motion around binary asteroids. *Celestial Mechanics and Dynamical Astronomy* **134** (41).

Hestroffer, D., Sánchez, P., Staron, L. et al. (2019). Small Solar System Bodies as granular media. *Astronomy and Astrophysics Review* **27** (6).

Hosder, S., Walters, R. W. and Balch, M. (2007). Efficient sampling for non-intrusive polynomial chaos applications with multiple uncertain input variables. *48th AIAA/ASME/ASCE/AHS/ASC Structures, Structural Dynamics, and Materials Conference* (1939).

Jet Propulsion Laboratory. Solar System Dynamics: Small-Body Database Lookup. `https://ssd.jpl.nasa.gov/tools/sbdb_lookup.html#/`. Accessed throughout July/August 2022.

Julier, S., Uhlmann, J. and Durrant-Whyte, H. F. (2000). A New Method for the Nonlinear Transformation of Means and Covariances in Filters and Estimators. *IEEE Transactions on Automatic Control* **45** (3), pp477–482.

Lacor, C. and Savin, É. (2018). General Introduction to Polynomial Chaos and Collocation Methods. *Uncertainty Management in Robust Industrial Design and Aeronautics*, pp 109–122.

Lamy, P. L., Kaasalainen, M., Lowry, S., et al. (2008). Asteroid 2867 Steins II. Multi-telescope visible observations, shape reconstruction and rotational state. *Astronomy & Physics* **487**, pp 1179–1185.

Lauretta, D. S., Balram-Knutson, S. S., Beshore, E., et al. 2017. OSIRIS-REx: Sample Return from Asteroid (101955) Bennu. *Space Science Reviews* **212**, pp 925—984.

Lauretta, D. S., DellaGiustina, D. N., Bennet, C. A. et al., & the OSIRIS-REx Team (2019). The unexpected surface of asteroid (101955) Bennu. *Nature* **568**, pp 55–60.

Le Maistre, S., Rivoldini, A. and Rosenblatt, P. (2019). Signature of Phobos' interior structure in its gravity field and libration. *Icarus* **321**, pp 272–290.

Lhotka, C., Reimond, S., Souchay, J. and Baur, O. (2016). Gravity field and solar component of the precession rate and nutation coefficients of comet 67P/Churyumov-Gerasimenko. *Monthly Notices of the Royal Astronomical Society* **455**, pp3588–3596.

Madeira, G., Charnoz, S. and Ryuki, H. (2023). Dynamical origin of Dimorphos from fast spining Didymos. *Icarus* **394** (115428).

Maybeck, S. (1982). Stochastic Models, Estimation and Control. *Academic Press, New York*.

Melman, J., Mooij, E. and Noomen, R. (2013). State propagation in an uncertain asteroid gravity field. *Acta Astronautica* **91**, pp 8–19.

Miller, J. K., Konopliv, A. S., Antreasian, P. G. et al. (2002). Determination of shape, gravity and rotational state of asteroid 433 Eros. *Icarus* **155** (1), pp3-17.

Montenbruck, O. and Gill, E. (2000). Satellite Orbits: Models, Methods and Applications. *Springer*. pp 56–58.

Morbidelli, A., Levison, H. F., Tsiganis, K. and Gomes, R. (2005). Chaotic capture of Jupiter's Trojan asteroids in the early Solar System. *Nature* **435**, pp 462—465.

Naidu, S. P., Margot, J. L., Busch, M. W. et al. (2013). Radar imaging and physical characterization of near-Earth Asteroid (162421) 2000 ET70 . *Icarus* **226** (1), pp 323–335.

Naidu, S. P., Benner, L. A. M., Brozovic, M. et al. (2020). Radar observations and a physical model of binary near-Earth asteroid 65803 Didymos, target of the DART mission . *Icarus* **348** (113777).

Park, R. S. and Scheeres, D. (2006). Nonlinear mapping of Gaussian Statistics: Theory and Applications to Spacecraft Trajectory Design. *Journal of Guidance, Control and Dynamics* **29** (6), pp 1367–1375.

Peter, H., Berzosa, J., Fernández, J and Féménias, P. (2020). Long-term evaluation of estimated solar radiation pressure coefficients from Copernicus Sentinel-1, -2, -3 satellites. *European Geosciences Union (EGU) General Assembly* Poster.

Poghosyan, A. and Golkar, A. (2017). CubeSat evolution: Analyzing CubeSat capabilities for conducting science missions. *Progress in Aerospace Sciences* **88**, pp 59-83.

Root, B. (2021). GSH is a MATLAB package to do Global Spherical Harmonic Analyses (GSHA) and Synthesis (GSHS) for Crust1.0. *4TU.ResearchData*, TU Delft, Faculty of Aerospace Engineering.

Savin, É. and Faverjon, B. (2017). Computation of higher-order moments of generalized polynomial chaos expansions. *International Journal for Numerical Methods in Engineering* **111** (12), pp1192–1200.

Scheeres, D. (2012). Orbital Motion in Strongly Perturbed Environments: Applications to asteroid, comet and planetary satellite orbiters. *Springer*, pp 35, 55–57.

Smolyak, S. A. (1963). Quadrature and interpolation formulas for tensor products of certain classes of functions. *Soviet Mathematics Doklady* **4**, pp 240-243.

Sudret, B. (2008). Global sensitivity analysis using polynomial chaos expansions. *Reliability Engineering and System Safety* **93** (7), pp 964–979.

Swindle, T. D. and The SBAG Steering Committee (2017). Small bodies exploration in the next 35 years. *Lunar and Planetary Institute Contributions - Planetary Science Vision 2050 Workshop* **1989**.

Takahashi, S. and Scheeres, D. (2020). Higher-Order Corrections for Frozen Terminator Orbit Design. *Journal of Guidance, Control and Dynamics* **43** (9), pp 1642–1655.

Topputo, F. and the Milani Team (2021). The Hera Milani CubeSat Mission. *Planetary Defense Conference*.

Vasile, M. and Manzi, M. (2023). Polynomial stochastic dynamical indicators. *Celestial Mechanics and Dynamical Astronomy* **135** (4).

Wiener, N. (1938). The Homogeneous Chaos. *American Journal of Mathematics* **60** (4), pp 897–936.

Xiong, F., Greene, S., Chen, W., Xiong, Y. and Yang, S. (2010). A new sparse grid based method for uncertainty propagation. *Structural and Multidisciplinary Optimization* **41** (3), pp 335–349.

Xiong, F., Chen. S. and Xiong, Y. (2014). Dynamic system uncertainty propagation using polynomial chaos. *Chinese Journal of Aeronautics* **27** (5), pp 1156–1170.

Xiu, D. and Karniadakis, G. E. (2002). The Wiener-Askey polynomial chaos for stochastic differential equations. *SIAM Journal on Scientific Computing* **24** (2), pp 619–644.

Xiu, D. (2010). Numerical Methods for Stochastic Computations: A Spectral Method Approach. *Princeton University Press* ISBN: 9780691142128.

Yeomans, D. K., Antreasian, P. G., Barriot, et al. (2000). Radio science Results During the NEAR-Shoemakers Spacecraft Rendezevous with Eros. *Science* **289** (5487), pp 2085–2088.

Zannoni, M., Tommei, G., Modenini, et al. (2017). Radio science investigations with the asteroid impact mission. *Advances in Space Research* **62** (8), pp 2273–2289.

Zuber, M. T., Park, R. S., Elkins-Tanson, L. T. et al. (2022). The Psyche Gravity Investigation. *Space Science Reviews* **218** (57).

APPENDIX A: Spherical Harmonic coefficients

The normalized spherical harmonic coefficients were retrieved from a constant density shape model of asteroid 2000 ET70 using the Global Spherical Harmonic (GSH) Package available at `https://github.com/bartroot/GSH`. The shape model was retrieved from `https://3d-asteroids.space/asteroids/162421-2000-ET70` and consists of 4000 vertices and 7996 faces. A constant density of 2000 kgm^{-3} (Naidu et al., 2013) and the volume averaged radius of 1131.6 m was used as reference radius R.

Table A1. Nominal normalized spherical harmonic coefficients

n	m	$\bar{C}_{nm}$	$\bar{S}_{nm}$
0	0	0.99886223	0
1	0	-0.0013447323	0
1	1	0.0002770569	-0.0013428831
2	0	-0.0243609310	0
2	1	-0.0001971808	-0.0000120438
2	2	0.0267656020	0.0000005117
3	0	-0.0053988986	0
3	1	0.0000491777	-0.0011901703
3	2	0.0015972360	0.0033030442
3	3	-0.0033099975	-0.0045905665
4	0	-0.0003487162	0
4	1	0.0001199528	0.0015916781
4	2	-0.0049342722	0.0017180791
4	3	-0.0013741496	-0.0017141996
4	4	0.0045661298	-0.0017444782
5	0	0.0051683975	0
5	1	0.0007023177	0.0009806907
5	2	-0.0017793191	-0.0000709472
5	3	0.0000407067	0.0000253136
5	4	-0.0004803431	0.0003636395
5	5	-0.0019120774	0.0000737780

The $\bar{C}_{00}$ value of 0.99886223 effectively means that the mass, and the gravitational parameter, are 0.1% smaller than reported. This is likely a discretisation error introduced by the GSH Package. This has no significant effect on the results as this margin falls well within the mass uncertainty of the asteroid.

3

Conclusions and recommendations

The detailed conclusions based on the results presented and discussed in the journal paper, and partially in the Appendices of this report, are presented in this chapter. Also recommendations for are given.

3.1. Conclusions

This section provides answers to the research questions posed in chapter 1. The answers to the sub-questions will be treated first. These answers combined will then lead to an answer to the main research question.

- **What are the capabilities of Non-Intrusive Polynomial Chaos and what challenges are encountered in its application to orbital motion around asteroids?**

  The performance of NIPC has been tested in an application to orbital motion around an asteroid with a large variety of settings, as presented and discussed in Appendix C. The process of tweaking and tuning the NIPC settings that efficiently generate a PCE which accurately approximates the true states was found to become increasingly challenging with an increase in the number of uncertainties. Similarly, a decrease in the orbital altitude and an increase in the propagation time, both of which can be regarded as measures for the degree of non-linearity encountered as observed in Section 6 of the journal paper, make this process more demanding. This process, therefore, not only requires a trade off between accuracy and efficiency of the method, but also between those aspects and the effort put into optimising them. In all cases must the accuracy be verified, at the very least by a comparison to a small MC ensemble.

  When tuning general settings, such as the polynomial order and the number of samples/quadrature nodes, does not provide the desired result, using more advanced settings can turn out beneficial. When the number of uncertainties increase, the performance of PCR improves relative to PCQ and PSP. Similarly, the benefits of Smolyak sparse grids becomes apparent only for a larger number of uncertain variables. The use of cross-truncated and orthonormal polynomials has not improved the NIPC performance in the studied cases.

  Another challenge was encountered in this work, besides the inability of finding generally optimal settings. The utility of Kepler elements in studying the orbital motion is limited by the singularities in their definition. As an orbit approaches one of these singularities, large variations in one or several of the elements are encountered. This may lead to the so-called torn discontinuities that cannot be filtered properly, as these variables also fully span the range from $0°$ to $360°$. When this is encountered, there is no use in analysing these elements. In addition to this, it must always be realised that strong negative correlations can exist between two Kepler elements, such as ω and θ. This means that two aspects of an orbit can change significantly, while the CubeSat's three-dimensional position does not. It must be realised, though, that these effects are not a result of applying NIPC and would be encountered for any non-linear uncertainty propagation method. They originate from the element set definition, rather than from the non-linear dynamics or NIPC method.

- **What orbital aspects are affected the most by rotational state uncertainties?**

In general, the dispersion and non-linearity due to rotational state uncertainties increase with a decrease in the orbital altitude and with an increase in propagation time. Especially when considering the Cartesian elements this is found to hold in general. However, it was found to be different in some cases where Kepler elements are studied. For example, the distance and non-linearity in inclination does not grow significantly with time for orbit 1, due to its equatorial orientation. Thus, where the dispersion in inclination can be largest compared to that in other elements over short propagation times, it will be superseded by those other elements over longer times.

A comparison to mass uncertainties revealed a difference in the orbital aspects most affected by these different uncertainties for different orbits. Where the semi-major axis and true anomaly are mostly affected by the mass uncertainty for all three orbits, e and the angular Kepler elements can also undergo significant contributions by the rotational state uncertainties. Moreover, Ω of a sufficiently low polar orbit was found to be more susceptible to the rotational state parameters than to mass.

Focusing on one semi-major axis, it was found that retrograde orbits are generally more stable than prograde orbits against rotational state uncertainties. However, for specific combinations of i_0 and Ω_0 also prograde and polar orbits can be stable. These findings were clearly observed for all Kepler elements, except i. Polar orbits were found to be more robust in i to rotational state uncertainties than equatorial and inclined orbits.

- **Do particular interactions between rotational state parameters and irregular gravity field components contribute relatively more to the dispersion of orbits than others?**

  No clear physical relation was found for the unstable semi-elliptical regions in the initial state grid analysis. It was observed that these regions can change with orbital altitude and propagation time. This means that the presence and location of such regions is highly case dependent. Moreover, it means that large dispersions can be initiated throughout the trajectories, at different instances in time.

  As verified by a study of the interactions between the rotational state parameters and the irregular gravity field components, there has not been a consistent set of cases in which a particular interaction clearly contributed more than the others. Thus, for different orbits and different propagation times, multiple, possibly different, interactions, can cause the majority of the dispersion. The unstable regions are therefore not strictly determined only by the location of the initial state with respect to a specific gravitational bulge, but rather by all the gravitational bulges that are encountered closely throughout the complete trajectory. Subsequently, this can affect the occurrence of eclipses and thus the effects of SRP, which can disperse the trajectories further. Of course, these are an indirect result of the initial state, but it shows that the effects are rather unpredictable based solely on the initial state. It may be the case as well, though, that a specific interaction clearly contributes the most to a specific case. Then, it is expected that the corresponding gravitational bulge is approached closely very often in this trajectory. However, this thus depends on various aspects, such as the initial state, the propagation time and the magnitude of the uncertainties.

- **Should rotational state uncertainties be considered in mission design studies and operational procedures?**

  Based on the comparison with the mass uncertainty, it is concluded that the effects due to rotational state uncertainties are significantly smaller. Thus, if, relative to the rotational state uncertainties, significant uncertainty in the asteroid's mass, and possibly also in SRP and the irregular gravity field, remain, there seems little need to also study the effects of rotational state uncertainties, both during mission design and operation.

  However, it was found that the rotational state uncertainties do contribute more to the dispersion of Ω for the polar orbit at 5 km. This shows that, in some cases the encountered non-linearity could result in rotational state uncertainties to more effectively alter a particular aspect of the orbit than mass uncertainty. This leads to conclude that there could be many more cases where the rotational state parameter uncertainties change specific orbital aspects more. In addition, the long-term propagation of rotational state uncertainties show significant dispersion, that may be costly to make up for with corrective maneuvers. Therefore, it is considered important for mission designers to verify whether ignoring the rotational state uncertainties is indeed valid for their specific study. If not, they must perform a detailed analysis of the effects it has on various orbital aspects and check if the orbit design they found without rotational state uncertainties actually remains optimal when these are present.

Considering operational procedures, it must be realised that deep space CubeSats are ideally autonomous. Especially in the highly non-linear and uncertain environment of a small body, the significant light time delays in communication with the spacecraft ask for self-corrective capabilities. Optical navigation with respect to the asteroid to facilitate these efforts is a trending research topic with regular advances being made. Although autonomous CubeSats should have some uncertainty propagator build into them to optimise their trajectory corrections, the limits on their computational power can restrict these to just the largest contributors, thereby eliminating the rotational state uncertainties. These effects should, therefore, have been considered in the mission design phase, which should have resulted in orbit designs that minimise the trajectory deviations due to these uncertainties. In cases where this is not (sufficiently) feasible, it should be questioned whether the mission should actually be executed, as probably better alternatives exist. As such, the CubeSat should undergo only small orbit deviations from nominal in a real mission. In addition, as the CubeSat approaches the asteroid more closely and the influence of rotational state uncertainties become larger, the rotational state parameters also become more accurately fixed. Thus, their effect may not actually become significant. As such, there are both little need and limited capabilities to consider rotational state uncertainties during operational procedures onboard the autonomous CubeSat and it is therefore considered to be even more important to consider them in the mission design process. On the other hand, the mission operations team on the ground should still update the orbit propagations with improved data of the asteroid. This allows them to better predict the orbit deviations that are to come, beyond the CubeSat's own capabilities, and possibly correct for them if deemed necessary. This should be done as a mere backup to the autonomous functionality of the CubeSat.

What are the non-linear effects of an asteroid's rotational state uncertainties on the orbital motion of a CubeSat?

The orbits studied in this work have revealed a wide variety of effects that can be observed when a CubeSat is exposed to uncertainties in the rotational state of an asteroid. Generally, the dispersion and degree of non-linearity increase with propagation time and decrease with orbital altitudes. However, this is not strictly the case for individual Kepler elements, as both have also been observed to stagnate after an initial increase.

It was also found that uncertainties in the rotation pole orientation (β and λ) affect the orbital motion more than uncertainty in the rotation period (T_{ast}) for short propagation times. However, as the propagation time increases, a larger phase lag of the asteroid with its nominal rotational state is established. This can cause the contribution of T_{ast} to become equal to that of β and λ for some cases.

In general, retrograde orbits are more robust against these uncertainties than prograde orbits. However, starting out in specific orbital planes, in terms of i_0 and Ω_0, can also result in stable orbit solutions for prograde orbits. Moreover, the occurrence of large dispersions is dependent on which gravitational bulges are encountered closely and at which times in the propagation. This high non-linearity is what can cause unexpected trajectory deviations. As such, it is always recommended to study rotational state uncertainties during the design of a real mission, either in full if possible or as a verification step for the suitable orbits obtained from other analyses. Especially for long propagations close to the asteroid these effects could be significant and unpredictable. During the mission, however, the need to study these uncertainties diminishes.

The high non-linearity of the dynamical environment of the asteroid can cause a large variation in the orbital elements over time due to uncertainties. Orbits that start out as nearly circular can attain significant eccentricity, inclined orbits can become equatorial and vice versa. It is then very likely that, over time, singularities in the definition of the Kepler elements are approached. In turn, this results in large variations in some of them, making the construction of a PCE more difficult and less efficient. In the worst case, this results in the so-called torn discontinuities that can not be filtered, and this leads to the inability to analyse these elements. An alternative is then to use Mean Equinoctial Elements, which avoid these singularities, but that comes at the cost of lower interpretability.

3.2. Recommendations for future work

The results presented and conclusions drawn in this work have been used to identify several aspect that are interesting and useful to be further investigated in future research efforts. These are discussed next.

- **Find the cause(s) of the unstable semi-elliptical regions in the initial state space**

In this research the true cause(s) of the unstable semi-elliptical regions in the space i_0 and Ω_0 was not found. Although it is thought to be due to the complex interactions with various irregular gravity field components throughout the complete trajectory, the symmetry suggests that there is a strong connection to the asteroid's largest SH components, $\bar{C}_{20}$ and $\bar{C}_{22}$. A deeper investigation to the cause(s) of the dispersion should verify this.

This should include the same analysis using Sobol' indices as presented in Section 6.5 of the journal paper, but for many more of the initial orbits considered. Possibly these should be performed with smaller SH uncertainties, so that the trajectory dispersions are more similar to those studied with only rotational state uncertainty. Adding the proper correlations between individual degree 2 SH coefficients is advised as well. Finally, it is advised to perform detailed studies of the time histories of the trajectories, to find which gravitational bulges, as caused by the different SH coefficients, are flown by at different times and linking those to the times at which larger dispersions are initiated.

- **Automatic NIPC generation guaranteeing accuracy and efficiency**

  Throughout this research, the settings required for efficiently generating accurate NIPC approximations were obtained manually by iterative testing. The tuning of settings was found to be highly case dependent and considerable effort was put into guaranteeing accuracy and optimising efficiency. The effort put into this part of the process could be alleviated by research efforts that focus on developing algorithms that automatically, with minimal human interaction, generate PCEs that guarantee a predefined accuracy level. Of course, it is fairly simple to create an algorithm that automatically increases the polynomial order and/or number of samples when the accuracy is insufficient. However, other settings, such as different quadrature rules, using PCQ with or without sparse grids or using PCR, were found to have different effects among different cases and the optimal choice is much less intuitive. The proper implementation, i.e. the order of increments in settings that are applied, that is optimal requires further research.

  Automating the process of finding the right settings can save substantial time and effort by the user. It is realised, however, that this automation also leads to higher computational cost, as low order polynomials are tested and may turn out to not be useful. This is sub-optimal, but the fact that computational cost increases exponentially with polynomial order is reason to believe that the 'wasted' computational effort is minimal compared to the useful effort. This point of research also leads to the following point and should ideally be combined.

  In this automation, it may seem that some sort of maximum settings must be defined, at which the algorithm concludes it is not feasible to construct an accurate PCE. This can be avoided, however, by splitting the uncertain domain into sub-domains when this is encountered. Then, a PCE can be constructed for each sub-domain, each of which should show less dispersion and lower non-linearity. Theoretically there will then always be a proper PCE, as long as enough sub-domains are used, and enough sub-PCEs are constructed. A downside here is that statistical information is then available for each individual sub-domain, and not for the complete uncertain domain.

  Two aspects that could improve the NIPC performance in this automated process are also proposed. Currently these aspects are not available within ChaosPy nor have they been encountered to be researched in literature, therefore they are believed to be novel ideas. They are:

  * **Develop quadrature rules that allow for adding nodes to the set that was used for generating the previous PCE**

    Currently, the sets created by many quadrature rules are defined by the quadrature order that is specified. This means that the set of nodes of a particular size can be completely, or partially, different from that of another particular size. This is inefficient if systematic increments in NIPC settings are tested, which asks for different set sizes to be used. The aforementioned automatic NIPC generation would therefore be benefited by quadrature rules that add nodes to an already existing set of nodes. The set should be extended, rather than be replaced (partially). This limits the wasted computational effort to that of generating the PCE, by avoiding wasting computational effort on propagating samples that are not used in the end. In fact, Smolyak sparse grids already apply this to their advantage for quadrature rules that have partially overlapping sets for different orders. However, also the Smolyak sparse grid of a specific order may not contain all the nodes of the previous one either.

It is realised, though, that this is a complex mathematical process and it is unsure to what extent this is possible in reality. That is, quadrature rules approximate integrals by a weighted sum of function evaluations. Thus, when increasing the number of nodes, the weights should be changed accordingly. If this breaks down the approximation of the integral, there is no use to it. This feasibility should therefore be studied first. If not possible, one might resort to quasi-random sampling sequences such as Sobol sampling, that allow for adding samples to an already existing set.

  * **Use variable order PCEs**

    Similar to the prior item, information from a PCE created with the first settings can be used to determine the next settings. For example, consider a study of five uncertainties, where a polynomial of order three does not result in sufficient accuracy. This PCE, however, does reveal that two of the five uncertainties show much less non-linear effects than the others. The new samples required to generate the next PCE then do not need to vary much in these two variables, but focus must be led on their variation in the three more effective ones.

    This observation asks for the application of variable order PCEs, where the polynomial order in the two variables is lower than in the other three. Indeed, it is the practical feasibility of implementing these suggestions that must be investigated. Questions such as how can this information be obtained most efficiently and what measures should be used as thresholds for making these decisions should be researched.

- **Analyse the effects of uncertainties for different rotational states**

  The current research has focused on analysing the effects of rotational state uncertainties on one asteroid that uniformly rotates about its principal axis. However, the large variety of small solar system bodies shows that rotation pole orientations and rotation periods can differ a lot between small bodies. The dispersion and non-linearity in those cases could be substantially different. In addition, many asteroids are not uniform rotators, but tumblers. This means that the rotation pole oscillates in time. Subsequently, several excitations of the small body's rotation pole could be present, similar to the precession and nutation of Earth's rotation pole. It could very well be, in fact, that asteroid 2000 ET70 is in one of these more complicated rotational states. This is expected to induce even more non-linear effects on the CubeSats orbital motion that are interesting to investigate.

  The uncertainties in the rotation pole orientation that have been used in this research limit the degree of tumbling that the studied asteroid can exhibit. That is, the 10° uncertainty in the orientation parameters, means that the asteroid could also be tumbling with a precession magnitude of 10°. It cannot be larger, because then it would have been distinguished from the radar observations. Although the tumbling magnitude falls within the uncertainty magnitudes that have been analysed, it could very well be that the effects are quite different when the asteroid is in fact tumbling. As has been observed, the high non-linearity of the dynamics can cause unpredictable results. It is therefore interesting to analyse if the motion around a tumbling asteroid is bounded by the motion around the same asteroid in uniform rotation, or whether this motion around the tumbling asteroid is dispersed more.

  It is realised that analysing uncertainties for asteroids in different rotational states is more complex. They require more rotational state parameters for their definition and more uncertainties are present accordingly, which make the PCE generation more difficult and costly.

- **Use reference frame better suited for mission analysis**

  In this work, all orbits were analysed in the asteroid-centered reference frame of the initial epoch, with nominal rotation pole orientation parameters. This was most suitable for this research, as it avoids kinematic rotation effects in the results. However, for mission design studies, it would be better to analyse all the states at the times of interest in an asteroid-fixed reference frame, which rotates along with the asteroid. This would better enable the study of the scientific return of a potential mission, because it defines the states of interest with respect to the actual orientation of the asteroid at that time, rather than at the initial epoch. Still, it is argued that the nominal rotation parameters should be used for this reference frame definition, rather than having this frame vary under uncertainty. That is, because if the latter were used, the CubeSat's initial state with respect to the asteroid's irregular gravity field's orientation would not change under uncertainty. Subsequently, this means that the uncertainty in rotation pole orientation practically becomes an uncertainty in the position of third bodies.

A
Nominal orbit design

The methodology used to find the three orbits that were analysed in the journal paper was shortly described there, but focus was laid on the choices made. This chapter provides a more detailed discussion of how these orbits were obtained.

The first steps in this procedure were to do a preliminary analysis on the integrator settings and perturbations that need to be considered, which is described in section A.1 and A.2, respectively. This analysis is preliminary in the sense that it is only used for the nominal orbit design, which considers shorter propagation times, of only single orbital revolutions, than the actual uncertainty propagations in the journal paper. Then, section A.3 elaborates on the Monte Carlo simulations that were performed and section A.4 describes the differential correction method applied to improve the orbit solutions further.

A.1. Preliminary integrator analysis

To ensure sufficient accuracy in the Monte Carlo simulation, a preliminary analysis of the integrator settings was performed. Initially, the Cowell propagator was selected, because of its general robustness and non-existent singularities. An error analysis was performed with the Runge-Kutta 4 (RK4) integrator. This integrator was chosen for generally providing acceptable propagation times for good accuracy and being stable, thus being a good choice for a varied set of orbits. For this fixed step size integrator a step size had to be found. This was done by performing propagations, for each semi-major axis that was chosen (2.5, 5 and 10 km) for the duration of one orbit at that orbital altitude, with various step sizes. For this, the gravity field of the asteroid was set to a spherical harmonics (SH) model with maximum degree and order of 5 and the perturbations by the solar radiation pressure (SRP), the Sun's point mass (PM) and the Earth's PM were included. This choice was made based on the order of magnitudes of these accelerations as presented in Figure 1 of the journal paper. Here it was observed that the Sun's PM and Earth's PM accelerations are likely of no influence, but this will be verified later. For now, they are included anyway.

The initial state was set as the Keplerian elements with respect to the asteroids body-fixed frame of the initial epoch, F_{ast}. The semi-major axes were set as mentioned and the other elements were all set to 0. It was

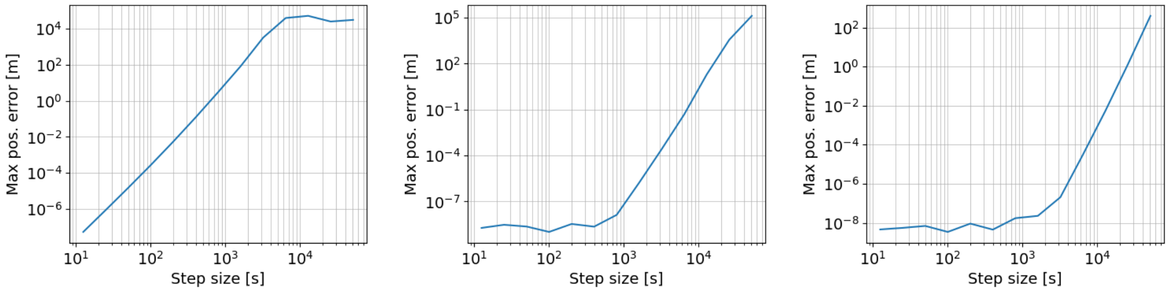

(a) Orbit 1

(b) Orbit 2

(c) Orbit 3

Figure A.1: Preliminary benchmark results with RK-4 integrator after one orbital revolution

Table A.1: Order of magnitude of position errors after one orbit when neglecting various perturbations

Perturbation	**2.5 km case**	**5.0 km case**	**10.0 km case**
Asteroid SH 2, 0	$3 \cdot 10^{1}$	$6 \cdot 10^{0}$	$2 \cdot 10^{2}$
Asteroid SH 2, 2	$4 \cdot 10^{2}$	$2 \cdot 10^{1}$	$6 \cdot 10^{0}$
Asteroid SH 5, 5	$4 \cdot 10^{1}$	$6 \cdot 10^{0}$	$2 \cdot 10^{0}$
Asteroid SH 10, 10	$2 \cdot 10^{0}$	$8 \cdot 10^{-2}$	$1 \cdot 10^{-3}$
Cannonball SRP	$2 \cdot 10^{0}$	$2 \cdot 10^{2}$	$9 \cdot 10^{1}$
Sun PM	$3 \cdot 10^{-2}$	$7 \cdot 10^{-1}$	$2 \cdot 10^{1}$
Earth PM	$1 \cdot 10^{-8}$	$2 \cdot 10^{-7}$	$4 \cdot 10^{-6}$

found that for all three cases, the orbits following from these initial conditions remained bounded to the asteroid for the duration of one orbit and are thus acceptable for this purpose. In subsequent propagations, the step size was doubled. The error associated with a single propagation was computed as the difference with respect to the propagation with half the step size, which is more accurate by a factor Δt^4 and can be considered the ground truth in this regard. As shown in Figure A.1a, a step size of 200 seconds yields truncation error dominance and cm-level accuracy for the semi-major axis of 2.5 km, which is deemed sufficient. As shown in Figure A.1b and A.1c, this step size yields rounding error dominance for the larger semi-major axes. This is unfavourable, because it makes the error unpredictable, so a larger step size was chosen. A step size of 4000 seconds yields truncation error dominance and position errors of 10^{-2} and 10^{-6} m for semi-major axes of 5.0 km and 10.0 km, respectively, and was therefore chosen. These step sizes yielded sufficient computational efficiency for the current purpose and thus no other integrators or propagators were considered.

A.2. Preliminary perturbation analysis

Similar to the integrator analysis, an analysis was performed to decide which perturbations to include in these propagations. Here, it is desirable that the model errors dominate the integration error, because that allows for a physical interpretation of the error, rather than one which is unpredictable. For this purpose, the same three orbits were propagated, first with only the asteroid's point mass gravity, and subsequently with a perturbation added. The perturbations were added considering their order of magnitude as seen in Figure 1 of the journal paper, the largest perturbation being added first. The error associated with neglecting a perturbation was found through the difference of the propagation with and without the perturbation. The results of this analysis are shown in Table A.1. The goal, here, is to obtain meter-level accuracy. This gives accurate insight into which orbits are close to periodic, because, as will be seen, position deviations will be significantly larger than 1 m after 1 orbit.

The results show that for the semi-major axis of 2.5 km, asteroid SH of degree and order 5 and Cannonball SRP need to be considered. For the semi-major axis of 5.0 km, asteroid SH of degree and order 2 and Cannonball SRP should be included. For the semi-major axis of 10.0 km, asteroid SH of degree 2 and order 0, Cannonball SRP and the Sun's point mass gravity should be included. From this it can be seen that the chosen orbital altitudes cover different orbital regimes, where different perturbation types have different effects, which is interesting for the analysis of uncertainties. It is found that the perturbation by Earth is negligible and therefore is was extrapolated that perturbations by the other planets are negligible too. This analysis was repeated for a different initial epoch, such that the alignment of the Sun, planets and the asteroid are different and the magnitude of perturbations will change. Moreover, the first initial time was chosen as midnight 19 February 2031 (982540800.0 sec since 1 January 2000), when the distance between the asteroid and Earth is near its maximum. The second initial time was chosen as 18 February 2035, when the distance between the asteroid and Earth is at a minimum(Figure A.2), and the perturbation thus larger. It was found that this did not alter the results by a significant amount, i.e. the perturbation by Earth's PM is still negligible. Although it may be more realistic to consider a mission when the asteroid is closest to Earth, considering the shorter transfer time required to visit the asteroid, it was opted to use 19 February 2031 from now on as initial time. The reason is that the distance between the asteroid and the Sun is at a minimum then, making the SRP and Sun PM perturbations largest and thus the uncertainties therein most pronounced, which might be useful in a later stage of the uncertainty analysis. This decision was made in an early stage of the research, when it was still open whether these uncertainties would be analysed. Nonetheless, it is expected that the initial time will not significantly affect the quality of the results of the uncertainty analysis, as the corresponding changes in the dynamics are only marginal and an uncertainty analysis is merely about changes in the dynamics under

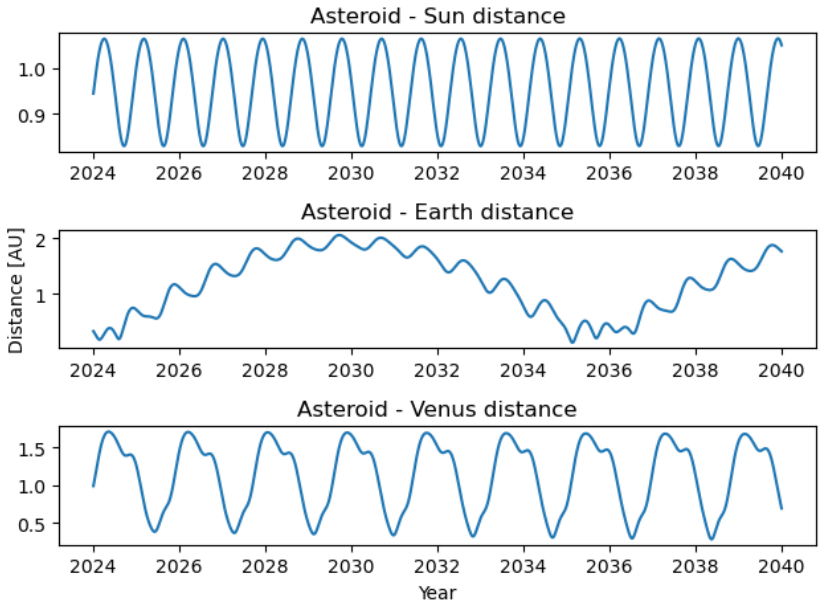

Figure A.2: Distances from asteroid 2000 ET70 to Earth, Venus and the Sun

uncertainty, rather than about their absolute accuracy.

To summarise, Table A.2 presents the selected integrator and perturbation settings that will be used for the design of the nominal orbits.

Table A.2: Preliminary propagation settings

Semi-major axis	Integrator	Perturbations
2500 m	RK4, 200 sec	SH D/O=5/5, SRP
5000 m	RK4, 4000 sec	SH D/O=2/2, SRP
10000 m	RK4, 4000 sec	SH D/O=2/0, SRP, Sun PM

Note that more detailed integrator and perturbation analyses were performed after the nominal orbit design phase, which is when orbits will be propagated over longer time spans and different settings will be needed. This is discussed in Appendix B.

A.3. Monte Carlo simulations

With the previously found settings, Monte-Carlo simulations were performed, for each semi-major axis separately. Each set of initial conditions was propagated for 1.25 times the duration of the corresponding Kepler orbit. This makes sure that each propagation fulfils more than a full revolution and the state after exactly one revolution can be checked against the initial state. This state difference is then used to check to what extend the orbit is periodic, which is defined in Equation A.1 and the ideal situation that is searched for. More specifically, for each computed orbit within the Monte Carlo simulations, the minimum position difference after one orbit with respect to the initial state was found through an 8th order Lagrange interpolation with 1 second time intervals. The velocity difference for the corresponding time instance was computed for comparison as well. The interpolation accuracy was verified once with a propagation with an exact termination condition at the obtained time of this minimum position difference.

$$\boldsymbol{x}(t+T) = \boldsymbol{x}(t) \tag{A.1}$$

The first Monte Carlo simulations only considered variations in the semi-major axis a (within a range containing the nominal value being studied), inclination i (0-180°) and right ascensions of the ascending node Ω (0-360°), as these are expected to alter the orbit's geometry with respect to the asteroid the most and thereby have the largest effect on the state differences after one orbit. The eccentricity e, argument of periapsis ω and true anomaly θ were fixed to zero and the initial time at 16 February 2031. The results from the first Monte Carlo runs were used as input for a narrower Monte Carlo search, in a region with small state differences. In these subsequent Monte Carlo runs, also e, ω and θ were varied. It was found that the subsequent Monte Carlo runs resulted in only marginal improvements to the original Monte Carlo runs, thus showing that a, i and Ω are more important in this regard.

Figure A.3 shows the results of the broadest Monte Carlo simulations. It is clear that the combination of i and Ω has important effects on the state differences, especially for the orbits around 5 and 10 km. Considering the orbits near 2.5 km (Figure A.3a and A.3b), the general trend is that state differences are smaller for $i > 90°$. Thus, polar and retrograde equatorial orbits are generally closer to periodic than prograde equatorial ones. However, prograde equatorial orbits that are similarly close to periodic also exist for particular values of Ω, namely near 60° and 250°.

Considering the orbits at 5 and 10 km, clearer trends are observed, that are similar for both as well. As presented in Figure A.3c through A.3f, where values of i near 90° yield low position differences in general, they are only accompanied with small velocity differences near Ω values of 90 and 270°. It is also observed, that for values of Ω near 180° yield larger velocity differences than those near 0° for orbits near 10 km, which is not observed for orbits near 5 km.

A.4. Differential correction

From all Monte Carlo runs, one orbit was taken per semi-major axis to be improved further. Here it was chosen to keep some diversity in the initial Kepler elements, to have a diverse set of orbits. Here, it was chosen to continue with a nearly retrograde equatorial orbit at 2.5 km and with polar orbits near 5 and 10 km, with Ω values near 90° and 270°, respectively. These orbits were propagated once again, now for a period of one month, to study their long-term behaviour. Also the State Transition Matrix (STM) was propagated, in order to allow for the application of differential correction to the initial state later, if deemed necessary.

Considering the orbit at a semi-major axis of 10.0 km, a significant drift away from the initial orbit was observed, which asks to be reduced. It was found though, that this drift mainly occurs in the second half of the propagation. Although the other two orbits seemed rather good, and definitely remain bounded within a limited range of orbital altitudes during one month, it was decided to try and improve them as well. This is done by applying differential corrections to the initial state, possibly multiple times, which works as follows. Along with the state, the STM is propagated. The STM, $\boldsymbol{\Phi}(t_l, t_0)$, contains the first derivatives of a state at time t_l with respect to an old state, here the initial state at time t_0, as given in Equation A.2a and Equation A.2b. Thereby it approximates a change in a state due to a change in the initial state. This matrix is propagated through Equation A.2c. Subsequently, Equation A.2d shows how the change in the state at t_l due to a change in the initial state is found. As it is known how a certain state changes due to a change in the initial state, it can also be computed how the initial state should be changed to obtain a particular change in the later state, which is the inverse operation, as described by Equation A.2e.

$$\boldsymbol{\Phi}(t_0, t_0) = \boldsymbol{I}_{6\cdot 6} \tag{A.2a}$$

$$\boldsymbol{\Phi}(t_l, t_0) = \frac{\partial \boldsymbol{x}(t_l)}{\partial \boldsymbol{x}(t_0)} \tag{A.2b}$$

$$\dot{\boldsymbol{\Phi}}(t_l, t_0) = \left(\frac{\partial \dot{\boldsymbol{x}}}{\partial \boldsymbol{x}}(t_l)\right)\boldsymbol{\Phi}(t_l, t_0), \tag{A.2c}$$

$$\Delta \boldsymbol{x}(t_l) \approx \boldsymbol{\Phi}(t_l, t_0)\Delta \boldsymbol{x}(t_0) \tag{A.2d}$$

$$\Delta \boldsymbol{x}(t_0) \approx \boldsymbol{\Phi}(t_l, t_0)^{-1}\Delta \boldsymbol{x}(t_l) \tag{A.2e}$$

The differential correction was applied as follows. The STM was interpolated, again with an 8th order Lagrange interpolator, to the time of the minimum position difference (after one orbit). Again, the interpolation accuracy was verified once with a propagation with exact termination conditions at this time of interest. This STM, along with the state difference with respect to the initial state was used to compute an update for the initial state according to Equation A.2e. This initial state was then propagated, as well as the STM, and if deemed necessary, a new update was computed. This procedure was repeated until the orbit was deemed good enough. A few observations were made during this process, as discussed now.

The initial state update did not always provide a better solution. Moreover, sometimes the initial state update resulted in an orbit that was significantly worse than the previous one. This is a result of the high non-linearity of the dynamics, which causes the validity of the linearised STM to break down for some cases.

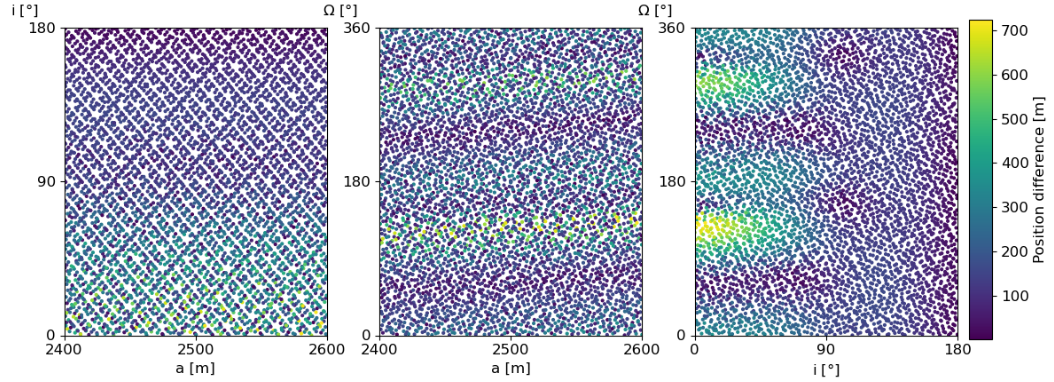

(a) Position difference near $a = 2.5$ km

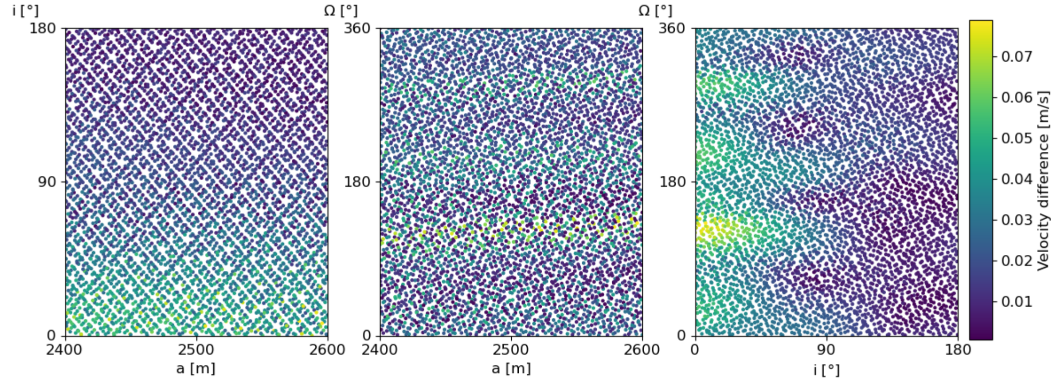

(b) Velocity difference near $a = 2.5$ km

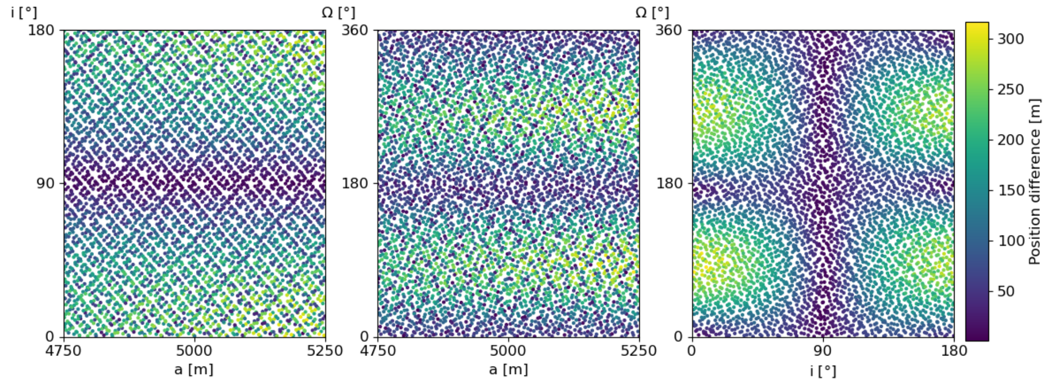

(c) Position difference near $a = 5$ km

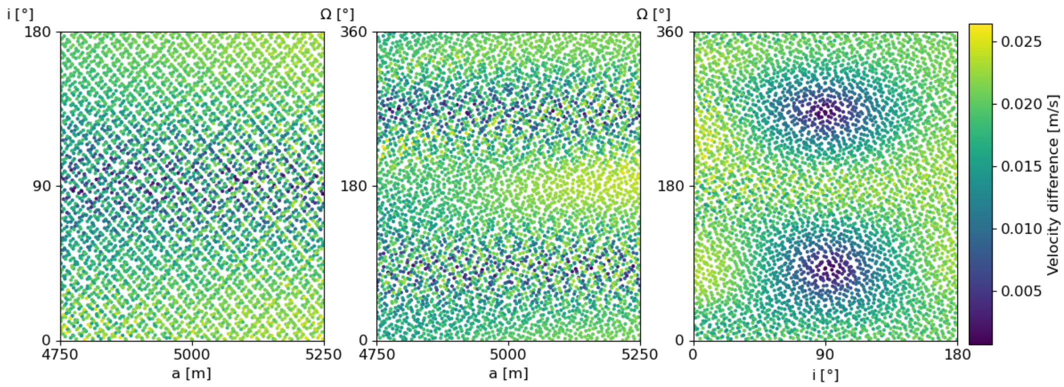

(d) Velocity difference near $a = 5$ km

Figure A.3: Position and velocity differences after one orbit for different orbital regimes

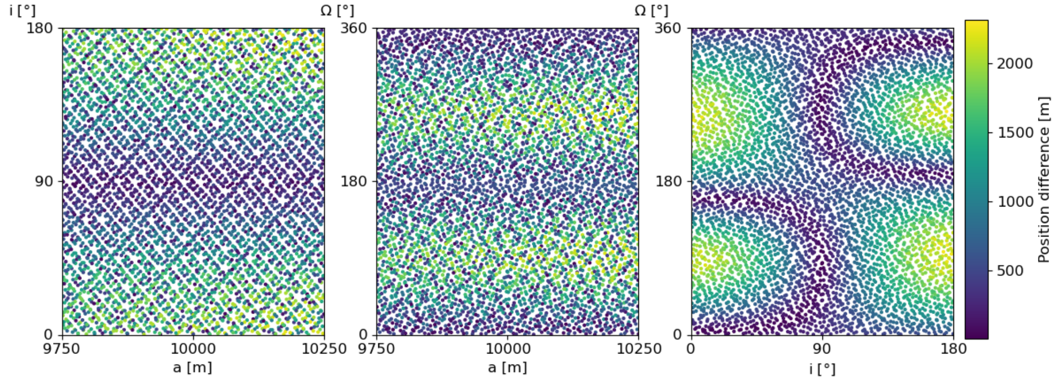

(e) Position difference near $a = 10$ km

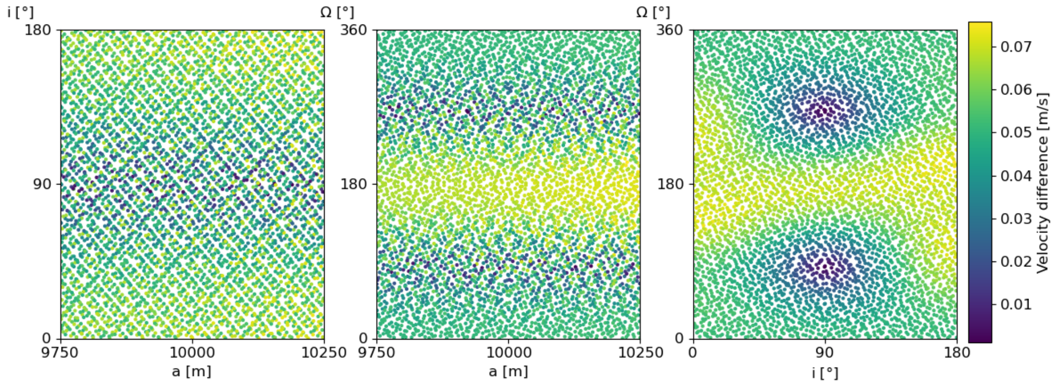

(f) Velocity difference near $a = 10$ km

Figure A.3: Position and velocity differences after one orbit for different orbital regimes

To counter this, the update procedure was extended by computing one more state update, this time through the state difference with respect to the initial state and the STM of the entry resulting from the propagation that lies closest to the initial state in terms of position, thus abandoning the interpolation. Both initial state updates were propagated and the best one was used for the next state iteration. It was found that, of the two initial state updates, the one with the smallest change in initial state generally yielded the best update. This can be explained by the fact that the STM assumes the dynamics to be linear, an assumption which is more valid for smaller state deviations. When this was realised, this was held onto as a rule of thumb, to reduce the number of required propagations. It was also observed that after a few iterations the state difference after one orbit did not reduce anymore after an update, at which point updates were computed from state differences after multiple orbits, which could make the orbit closer to periodic also for a longer period. Here, it was found that a trial and error approach had to be employed to find an update that would yield a better solution.

The best orbits found for each of the three semi-major axes were not truly periodic after several initial state updates, as expected. Even though the orbits had not improved as much as initially desired either, it was decided, for several reasons, that these orbits are acceptable to start the sensitivity analysis. Firstly, the orbits are bounded and their semi-major axes remain within a small range of the nominal, and initial, values. Secondly, the largest part of the drift occurs in the second half of the propagations, thus maneuvers can be applied after two weeks to stabilise the orbit, which is a common time span for such missions. Thirdly, finding better orbits with additional initial state updates or additional Monte Carlo runs will take significant amount of time and is considered not worth the effort. The three chosen orbits, corresponding to semi-major axes of approximately 2.5 km, 5 km and 10 km, respectively, 4 and their initial conditions in F_{ast}, were provided in Figure 4 and Table 4 of the journal Paper. It is interesting to the note the difference in the orbit drifts orbit 2, which drifts to positive z-values, and orbit 3, which drifts to negative z-values. Since there are no significant differences in the applied accelerations, neither in direction nor in magnitude, it is expected that this behaviour is due to the difference in periapsis location of both orbits. That is, the periapsis of orbit 2 lies 'above' the asteroid (positive z), whereas the periapsis of orbit 3 lies 'under' the asteroid (negative z).

B
Propagation settings

The black-box function, EoM 1 in the journal Paper, is solved numerically through integration. To verify the results, accuracy and efficiency, have to be ensured. This chapter explores the tuning of the propagation settings to achieve acceptable accuracy.

B.1. Benchmark

To find good propagation settings, benchmark solutions for each of the three orbits were to be generated for 30 day propagations, which is the maximum propagation duration analysed in the Journal paper. For this, the perturbations as found in section A.2 were used. In this analysis, occultations by the asteroid were not included, which was only realised later to be applicable. Benchmarks were generated with the RK-4 integrator, for its robustness and sufficient efficiency, and the step size was doubled for subsequent propagations. The error was computed as the largest state difference with the propagation with half the step size throughout the propagation. The results are shown in Figure B.1 for each orbit. Truncation error dominance is desired, corresponding to the smooth and regular increase in the maximum position error. From these results the following step sizes were chosen for the benchmarks: 6.25 seconds, 25.0 seconds and 100.0 seconds for orbits 1, 2 and 3, respectively. Some remarks are made. Firstly, the flattening of the error curve for large step sizes is a result of the CubeSat flying away from the asteroid in different directions for different step sizes. Secondly, for a particular step size, the error is greatest for orbit 1, second greatest for orbit 2 and least for orbit 3. Similarly, the occurrence of rounding error dominance, where more irregular error behaviour occurs, is delayed to smaller step sizes for smaller orbital altitudes.

B.2. Integrator analysis

The choice of integrator scheme can affect the propagation efficiency to a large extent. Various Runge-Kutta (RK) solvers, as well as Bulirsch-Stoer (BS) and Adams-Bashforth-Moulton (ABM) integrators are available in Tudat(Py). Each has their own (dis)advantages and thus a comparative analysis was performed on these inte-

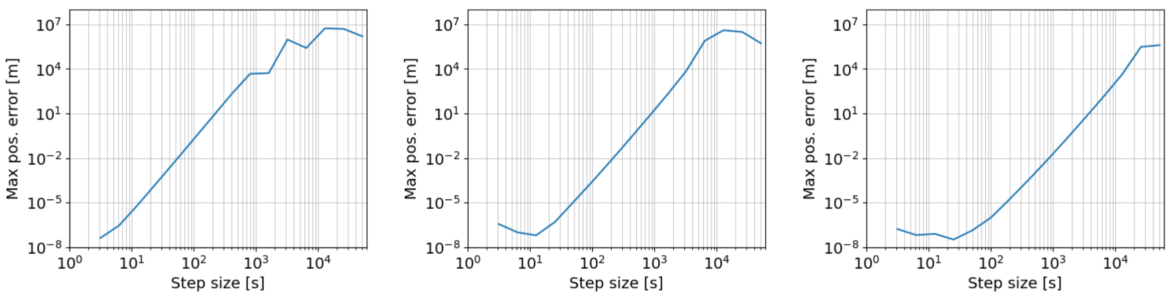

Orbit 1 Orbit 2 Orbit 3

Figure B.1: Benchmark results with RK-4 integrator grators. Both fixed and variables step size integrators were analysed, with the aim to achieve cm to dm-level accuracy, which is then dominated by the dynamical model errors. The error for each propagation was computed as the maximum state difference throughout the propagation with respect to the benchmark solution. The time history of the state difference was analysed for each case as well, to verify that the maximum state difference is not an outlier and is well representative of the whole trajectory. For the fixed step size integrators, step sizes were used that are multiples of the benchmark step size, so that direct comparisons between propagation results is possible. For the variable step size integrators this is not possible and interpolation of the benchmark solution was required. For the fixed step size integrators, step sizes of 100, 200, 400, 800, 1600, 3200, 6400 and 12800 seconds were analysed for each integrator. For the variables step size integrators, absolute and relative tolerances were set equal and values of 10^{-4}, 10^{-6}, 10^{-8}, 10^{-10} and 10^{-12} were used. In addition, the initial and minimum step sizes were set to 1 second and the maximum step size was set to the propagation duration of 30 days.

Overviews of the maximum state differences with respect to the benchmark solutions are provided in Figure B.2, where the errors are given as a function of the number of function evaluations required to achieve that result, a direct indication for the CPU time required. Several consistent observations are made. Firstly, Ralston-3, RK-4 and RKF-5(6) are less efficient than the higher order RK(F)/(DP) and ABM integrators. Secondly, The fixed step BS, higher order RK(F)/(DP) (in orange) and ABM integrators perform almost equally well for all three orbits. Thirdly, the variable step ABM integrators, however, perform consistently worse than its BS and higher order RK(F)/(DP) counterparts. This is most likely due to the way it is implemented in Tudat(Py). The step size control algorithm for this multi-step predictor-corrector integrator is complicated and not the most advanced and robust scheme is currently implemented, apparently yielding low efficiency. Fourthly, it is not necessarily the highest order RKF method that performs most efficiently among the variable step size integrators. Moreover, the RKDP-8(7) variable step size integrator is most efficient considering orbits 2 and 3. Finally, is seen that the fixed step size integrators can achieve higher accuracy than the variable step size integrators. Since both achieve accuracies better than cm-level and are almost equally efficient, this is not so relevant, though.

A fixed step size integrator has an important advantage and therefore it was opted for. This advantage is that no interpolation is required if the step sizes are chosen adequately and the propagation results can be compared directly. A variable step size integrator would require interpolation to compare states among different propagations, which in turn means that extra effort has to be put in ensuring that the interpolation error is negligible. Since we will be interested in the deviations of the state at various times in the propagation, and not just the final state, it is beneficial to use a fixed step integrator. From the analysis is seems that, for fixed step integrators, there is no clearly better integrator. It is therefore decided to go for a stable and robust algorithm. This was found in the RKDP-8(7) integrator, which was finally chosen for all orbits.

Although the performance of various integrators does not vary much among the different orbits, the required step size for a particular accuracy does. Moreover, it was found that for cm-level accuracy, Orbit 1 requires a step size between 400 and 800 seconds (follows from Figure B.2a), Orbit 2 requires a step size just below 3200 seconds (follows from Figure B.2c) and Orbit 3 requires a step size between 6400 and 12800 seconds (follows from Figure B.2e). In order to avoid the need of interpolating results later, it was chosen that the step sizes used for the different orbits have to be multiples of each other, so that direct comparisons of propagations results is possible. As such, it was chosen to use step sizes of 600 seconds, 3000 seconds and 9000 seconds for Orbit 1, Orbit 2 and Orbit 3, respectively. Orbit 3 then has the sparsest output, but with 288 state entries over 30 days, this should be more than enough to analyse the deviations of trajectories over this period and see if there are moments when the deviations become more pronounced than at other times.

As mentioned briefly earlier, occultations by the asteroid were not included in the foregoing analysis. At this point it was realised that, for a better representation of reality, these had to be included. Including them resulted in some changes that needed to be made to orbit 1, as it does undergo occultations in its trajectory. This is not the case for orbit 2 and 3.

It was found that orbit 1 deviates significantly with the inclusion of occultations. In addition, it was realised that, when uncertainties are propagated, these occultations will occur at different instances in time. Moreover, the transition into and out of an occultation typically requires smaller step sizes to be captured properly than those well within or out of eclipse. As such, it is argued that a variable step size integrator is better applicable for orbit 1. Rather than going through the entire process of finding proper integrator settings, it was chosen to use the variable step size RKDP-8(7) integrator, based on its performance shown in Figure B.2b, B.2d and B.2f. The required tolerance was found through another benchmark procedure. In this case, propagations were compared to one with a two orders of magnitude stricter tolerance level. As shown in

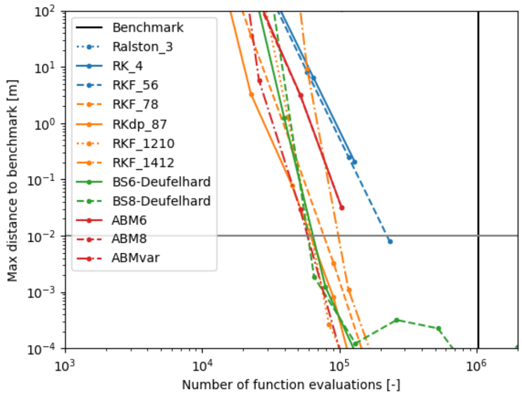

(a) Orbit 1- Fixed step size

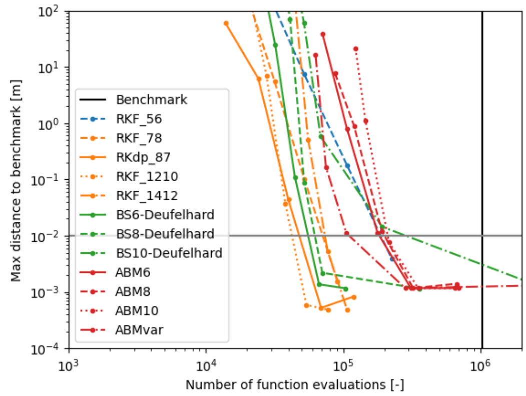

(b) Orbit 1 - Variable step size

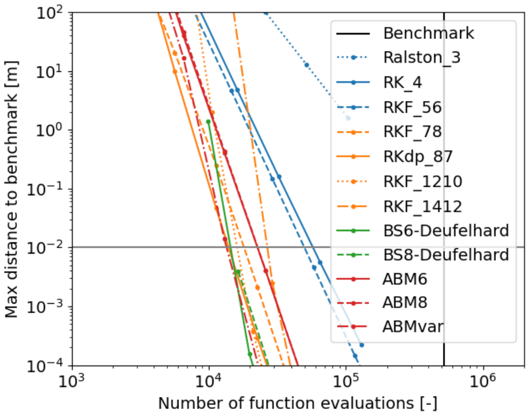

(c) Orbit 2 - Fixed step size

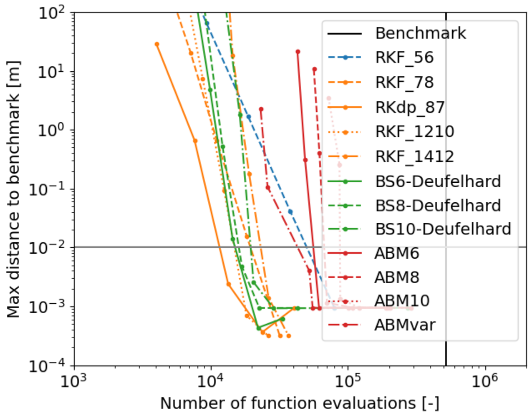

(d) Orbit 2 - Variable step size

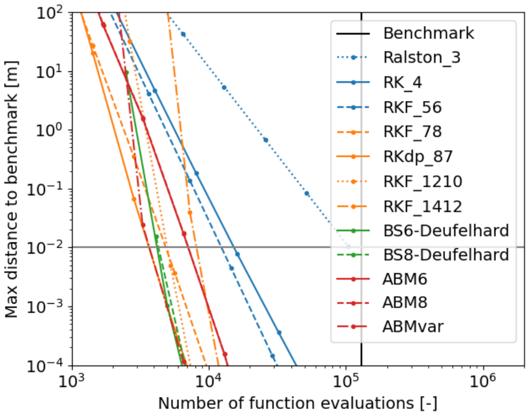

(e) Orbit 3 - Fixed step size

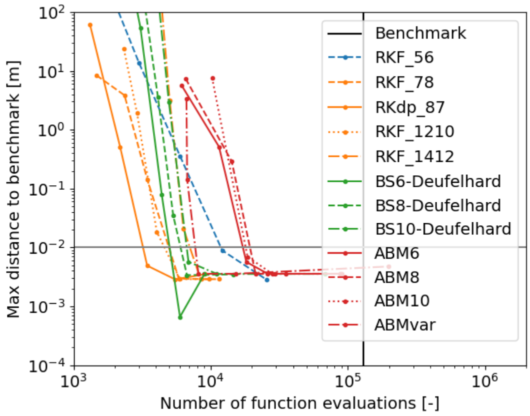

(f) Orbit 3 - Variable step size

Figure B.2: Integrator performance comparison for the three nominal orbits

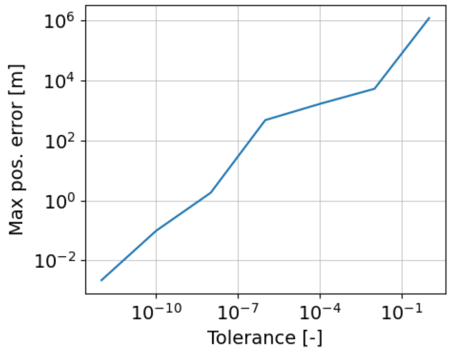

Figure B.3: Variable step size RKDP-8(7) integrator performance for orbit 1

Figure B.3, a tolerance of 10^{-10} is sufficient for dm-level accuracy. This was chosen over a tolerance of 10^{-11} for cm-level accuracy, because of the significant computational cost benefit. Especially for orbit 1 at close distance to the asteroid this should be sufficient, as trajectories will disperse much more than that under uncertainty.

Subsequently to deciding that a variable step size integrator is required, a need arises to perform interpolations on the obtained state history. Although undesired as mentioned before, this is not necessarily a problem. It does require a verification of the interpolation error, though. For that purpose, interpolations at 5, 10, 15, 20 and 25 days were performed with Lagrange interpolators with 6 and 8 points. The interpolation results were compared to propagations with exact terminations at these times and with the same tolerance of 10^{-10}. In addition, the interpolations with 6 and 8 points were cross-compared. All state differences were found to be of sub-cm-level (and most of sub-mm-level). Thus, the interpolation error is smaller than the integration error and well within acceptable ranges. The selected integrator settings are summarised in Table B.1.

Table B.1: Selected integrator settings per orbit

Orbit	Integrator	Settings
Orbit 1	Variable-step RKDP-8(7)	Tolerances: 10^{-10}
Orbit 2	Fixed-step RKDP-8(7)	Step size: 3000 sec
Orbit 3	Fixed-step RKDP-8(7)	Step size: 9000 sec

B.3. Perturbation analysis

Finally, a check was made on the accuracy that is achieved with the current choice of integrator settings and perturbations that were included. As such, propagations with the RKDP-8(7) integrator as selected in the previous section were performed with the first most effective perturbations, which was left out initially in Appendix A, now included. These are the spherical harmonics up to degree and order 10 and up to degree and order 5, for orbit 1 and 2 and 3, respectively. Also the Sun's point mass gravity was checked for orbit 1 and 2 and the Earth's point mass gravity was checked for orbit 3. The corresponding maximum state differences were checked over a 30 day propagation, rather than over one orbit as was done in section A.2. The corresponding errors are summarised in Table B.2.

Table B.2: Errors made by neglecting perturbations, after 30 day propagations with the integrators selected in the previous sections

Orbit	Perturbation	Position error [m]
Orbit 1	Asteroid SH D/O=10/10	60
	Sun PM	8
Orbit 2	Asteroid SH D/O=5/5	120
	Sun PM	8
Orbit 3	Asteroid SH D/0=5/5	2
	Earth PM	0

The model errors are deemed acceptable for the following reasons. As mentioned earlier, the uncertainty analysis is merely about deviations between trajectories under uncertainty, than about the true trajectory under a specific circumstance. As such, perturbations that have the same effect on all trajectories subject to uncertainty, are not critical to be included. This holds for the third body point masses, which are independent of the rotational state parameters. Also the corresponding model errors are small, thus these can safely be neglected. Considering the SH coefficients, one could argue that higher degree and order ones have to be included, because they yield significant model errors if not included and they will alter the trajectories subject to uncertainty in the rotational state parameters. However, the main effects of the uncertainty in the rotational parameters are expected to occur through the degree 2 SH coefficients. This is because the relative effects of SH coefficients vanishes with their degree, thus their contribution to the uncertainty analysis of the rotational state does, too. As such, there is no strict need to include the higher degree SH coefficients. In orbit 1 the degree and order 5 SH coefficients are included, though. This was decided because the corresponding model error would be much larger even, possible in the order of several hundreds of meters. This is deemed unacceptable for the representation of the nominal orbit. Finally, and as an additional motivation for the choices made, the effects due to uncertainties in the model parameters are expected to be significantly larger than the listed model errors. Therefore it was chosen to use the dynamical models for each of the orbits as summarised in Table B.3.

Table B.3: Dynamical models selected for inclusion in uncertainty analysis

Orbit 1	Orbit 2	Orbit 3
Asteroid SH D/O=5/5	Asteroid SH D/O=2/2	Asteroid SH D/O=2/2
Cannonball SRP	Cannonball SRP	Cannonball SRP
		Sun PM

Besides the integrator, its settings and the perturbations, also the propagator can be adapted. However, at this point the Cowell propagator has functioned well and the current integrator settings have made the propagation efficiency more than acceptable. As such, there is no need to improve it with another propagator. An advantage of this propagator is that it has no singularities.

C

Non-Intrusive Polynomial Chaos performance

As described in section 5 of the Journal paper, the performance of NIPC is heavily dependent on the particular problem case that is considered and the settings that are used. In the Journal paper, proof was given of the performance of the chosen settings for the cases that were studied there. In contrast, this chapter presents the performance of NIPC for various cases with different NIPC settings. The results presented here have been used to gain knowledge of the effects of the various NIPC settings and have functioned as guidelines throughout the project for selecting the right NIPC settings for the cases that were studied in great detail.

Again, the NIPC performance, which considers a trade-off between accuracy and efficiency, is given as the RMSE and ϵ_{max} as fraction of the mean distance of a quasi-random ensemble of 500 final states to the mean final state. These fractions are used, rather than the true RMSE and ϵ_{max} values, because the need for high accuracy in individual samples diminishes with an increase in the spread in the Monte Carlo ensemble. Both fractions are given with respect to the number of samples required, which is a direct indicator of efficiency.

This section is structured as follows. First, the performance of the different solution methods with various polynomial orders are compared for one and three uncertain variables. These results are put into perspective with a discussion of what level of accuracy should be aimed for. Then, various quadrature rules are compared within the PCQ method and the potential performance improvement by using Smolyak sparse grids, cross-truncated polynomials and orthonormal polynomials are tested, also for three uncertainties. Similar comparisons are then performed with five and eight uncertainties, revealing that different settings are optimal among these different cases.

PSP, PCQ, PCR and different polynomial orders

Figure C.1 and C.2 show, for one and three uncertain variables, respectively, the performance of NIPC for the three methods and three polynomial orders. It is clear that accuracy increases with polynomial order, as expected. Although all methods converge to similar values for the RMSE and ϵ_{max} values as the number of samples is increased, two systematic differences can be observed. First, PCQ converges for less samples than PSP. This could imply that the use of quadrature weights has an adverse effect on the computation of the polynomial coefficients and can be understood as follows. Quadrature weights are typically large in the centre of the uncertain domain and become smaller and smaller as nodes approach the boundaries of this domain. This means that the nodes near these boundaries have less control over the computation of the coefficients, which results in a polynomial that does not approximate the regions near these boundaries well. As more nodes are used, the weights of the nodes near the centre are reduced and more influence is given to nodes near the boundaries, yielding a polynomial that better approximates the boundary region as well, yielding a better overall approximation. This may be the reason that convergence for PSP is delayed to more samples than PCQ, which does not use the quadrature weights in the least-squares solution. Although in theory PCQ could also use these weights, this is also expected to delay convergence. The PSP method without using the quadrature weights was also not tested, because it is not expected to outperform PCQ, which should reach good accuracy for $q = p + 1$ as also mentioned in section 3.1.1 of the journal paper. Secondly, although PSP converges to smaller RMSE fractions than PCQ and PCR, its ϵ_{max} fraction converges to larger values. Thus, although the differences are minimal, it is observed that PSP performs generally better in terms of RMSE (after

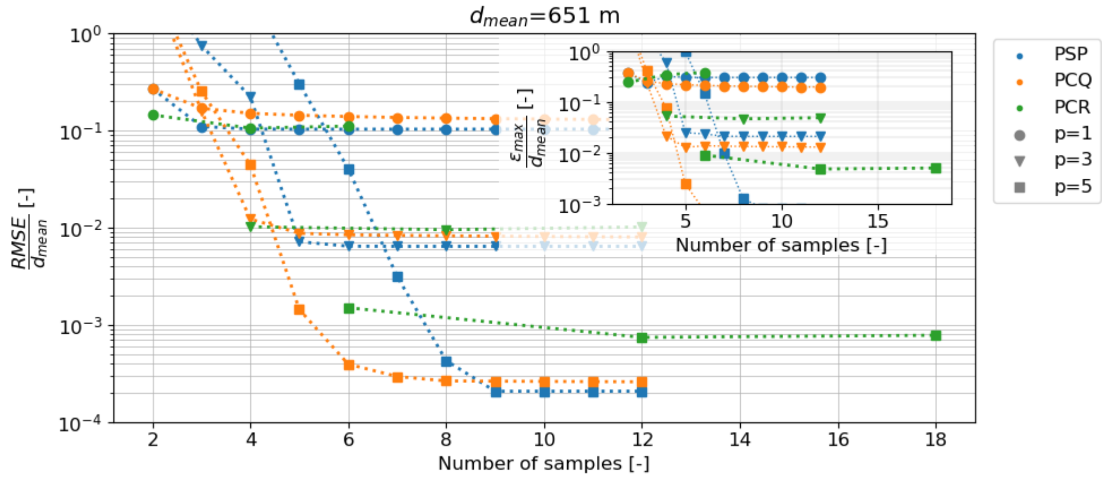

Figure C.1: NIPC performance for PSP and PCQ with Clenshaw-Curtis quadrature and PCR with random samples (seed=4444) and different polynomial orders: Orbit 2 - 30 days - 1 uncertainty: $\beta \pm 10°$)

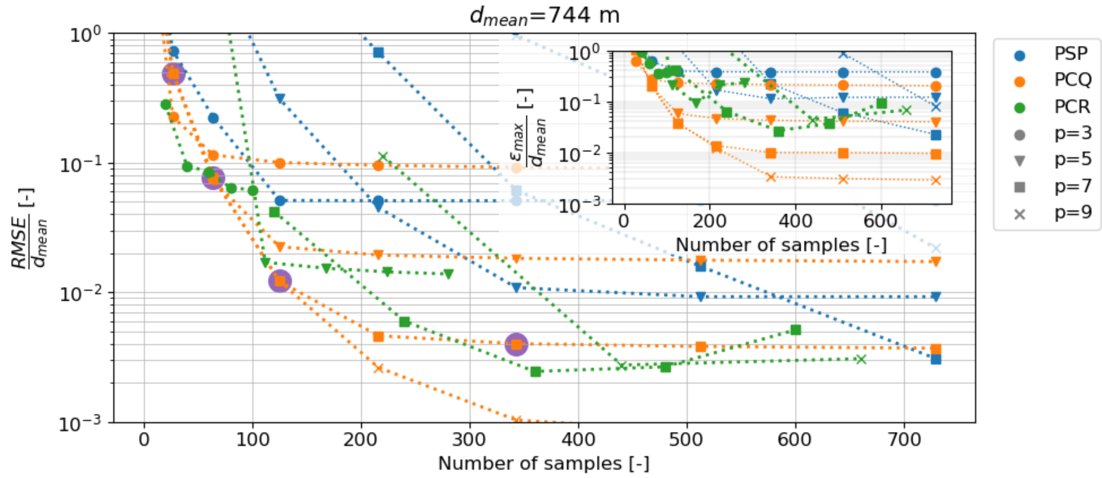

Figure C.2: NIPC performance for PSP and PCQ with Clenshaw-Curtis quadrature and PCR with random samples (seed=4444) and different polynomial orders: Orbit 2 - 30 days - 3 uncertainties: β and $\lambda \pm 10°$ and $T_{ast} \pm 0.01$ hr

convergence), whereas PCQ is more effective in minimizing the maximum error. With regard to both points made, the performance of PCR is somewhat unpredictable.

Required accuracy

To select the most efficient NIPC settings for a particular study case, it is crucial to understand the implications of the various accuracy levels. This subsection elaborates on the desired accuracy level to perform reliable sensitivity analyses.

One can realistically reason that an RMSE value equal to d_{mean} is too large. It means, that the errors of the polynomial approximations with respect to the Monte Carlo samples are in the order of magnitude of the mean distance to the nominal point of this Monte Carlo ensemble. This implies that individual points may be approximated to lie far outside the actual ensemble and therefor the errors are too large. Similarly, an RMSE value of 10^{-4} implies that the errors are in the order of 1000 times smaller than the mean distance to the nominal point of the ensemble, which suggests that individual points are well approximated with respect to the spread in the full ensemble. Thus, sufficiently accurate to draw reliable conclusions about the sensitivity of the dynamics to the uncertainties that are analysed.

To get a better feeling for the implications of various accuracy levels in between the two mentioned, Figure C.3 shows, for the four cases highlighted in purple in Figure C.2, the 500 Monte Carlo final states and

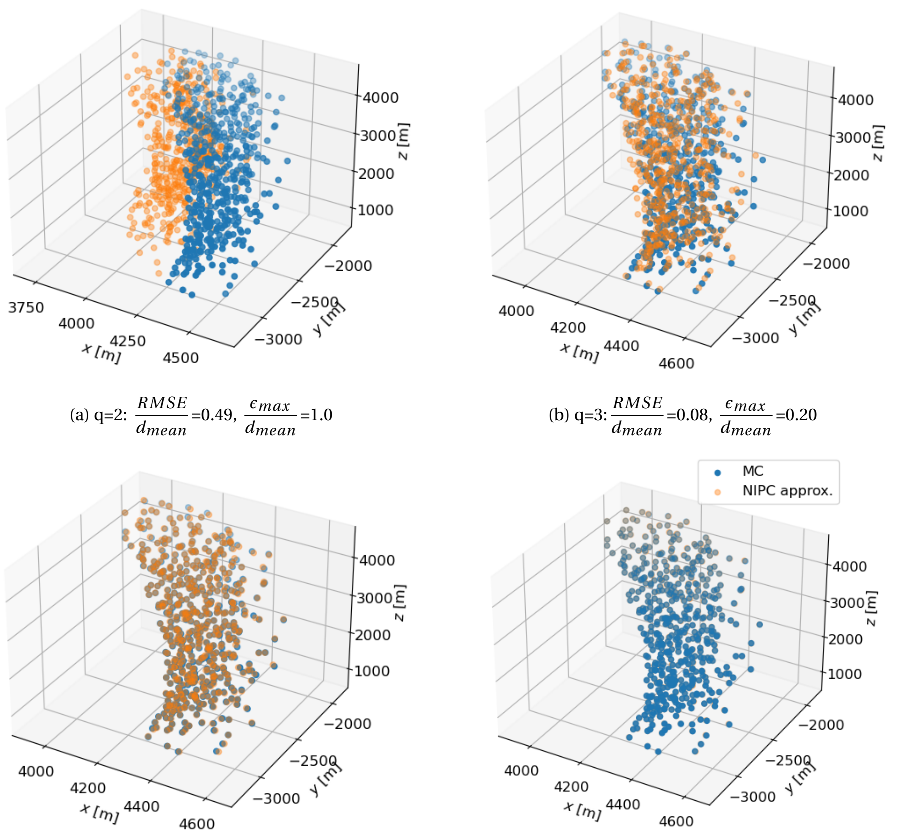

(a) q=2: $\frac{RMSE}{d_{mean}}$=0.49, $\frac{\epsilon_{max}}{d_{mean}}$=1.0

(b) q=3: $\frac{RMSE}{d_{mean}}$=0.08, $\frac{\epsilon_{max}}{d_{mean}}$=0.20

(c) q=4: $\frac{RMSE}{d_{mean}}$=0.01, $\frac{\epsilon_{max}}{d_{mean}}$=0.04

(d) q=6: $\frac{RMSE}{d_{mean}}$=0.004, $\frac{\epsilon_{max}}{d_{mean}}$=0.01

Figure C.3: NIPC performance for PCQ with Clenshaw-Curtis quadrature and different quadrature orders. $p = 7$, orbit 2, 30 days, 3 uncertainties: β and $\lambda \pm 10^{\circ}$ and $T_{ast} \pm 0.01$ hr, d_{mean}=744 m

their NIPC approximations. Clearly, C.3a shows large errors in the individual samples and the ensemble as a whole. It cannot be used for a proper analysis. Subsequently, C.3b shows significant improvement, where the ensemble as a whole is quite well represented. Errors in individual samples are still clearly visible, but for many samples it is clear which NIPC approximation belongs to which Monte Carlo sample. The same is true for C.3c and C.3d, where the individual errors have become significantly smaller and each NIPC approximation can be clearly linked to a Monte Carlo sample. As such, it is concluded that RMSE fractions in the order of 0.01 and ϵ_{max} fractions in the order 0.05-0.1 are proper guidelines for NIPC performance levels that will yield sufficiently accurate sensitivity analysis results. As such, it can be concluded, that for the case of Figure C.2, PCQ with a polynomial of order 7 and using 125 samples is most efficient to yield sufficiently accurate results.

Quadrature rules

PCQ in ChaosPy can be used with 16 different quadrature rules. Figure C.4 shows, for a subset of these, that performance can differ by a factor two in RMSE and more in ϵ_{max} among these rules. This can be understood by the considering a simple example. Considering a case that is well-represented by a univariate quadratic polynomial, but not perfectly. A good approximation can be made if 3 samples are used of which one is located at the extreme value. However, using 4 samples that are all quite far from this extreme point, might yield a worse approximation considering the full uncertain domain, possibly with a larger error for the extreme point. It is expected that this is case dependent, so it is recommended to consider different quadrature rules if the accuracy is not yet sufficient.

The sensitivity to pure rotation was analysed with PCQ, polynomial order 5 and the Gaussian quadrature rule in the Journal paper. It was shown that these settings do not achieve the accuracy as recommended earlier for orbit 1 and a propagation of 30 days. Still choosing these settings was partly based on the results presented in Figure C.5. It shows that Gaussian quadrature outperforms Clenshaw-Curtis quadrature and that significant improvements are only possible with higher polynomial orders and a large increase in the

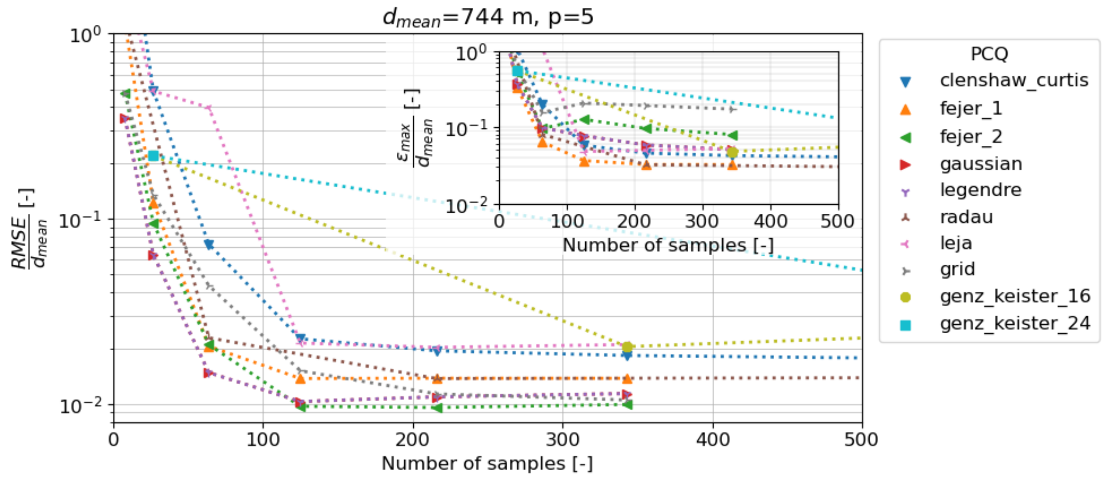

Figure C.4: NIPC performance for various quadrature rules and $p = 5$: Orbit 2 - 30 days - 3 uncertainties: β and $\lambda \pm 10°$ and $T_{ast} \pm 0.01$ hr

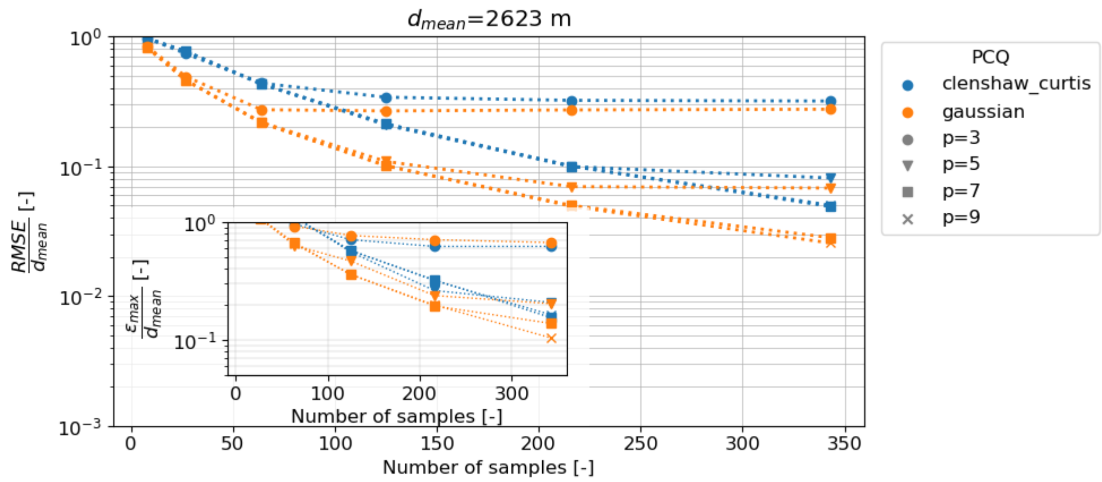

Figure C.5: NIPC performance for Clenshaw-Curtis and Gausian quadrature with different polynomial orders: orbit 1 - 30 days - 3 uncertainties: β and $\lambda \pm 10°$ and $T_{ast} \pm 0.01$ hr

number of samples used, which was deemed undesired.

Sparse, cross-truncation and normal polynomials

Figure C.6 shows that, for this case of three uncertainties, the use of Smolyak sparse grid, normal polynomials and cross-truncated polynomials is not beneficial in terms of either efficiency or accuracy.

Five uncertainties

As an intermediate step to the case of eight uncertainties as analysed in the Journal paper, five uncertainties were studied as well. The rotation parameters were given their pre-mission uncertain magnitudes and additionally $\bar{C}_{20}$ and $\bar{C}_{22}$ with ±50% uncertainties were studied. This choice was motivated by the following two considerations. Firstly, these two coefficients have the largest nominal magnitudes (see Appendix A from the Journal paper) and are therefor have the largest effect on the dynamics. Secondly, spherical harmonic coefficient uncertainty prior to any mission is typically extremely high, because of both size uncertainty and interior structure uncertainty. Size is directly related to inertia, which in turn is directly related to the degree 2 coefficients through simple equations [41]. Thus, the pre-mission size uncertainties of 5% [37] in each semi-axes were transformed to degree 2 coefficient uncertainties, yielding uncertainties up to 50%. This dominates interior structure uncertainty [42] and thus these uncertain magnitudes were studied here.

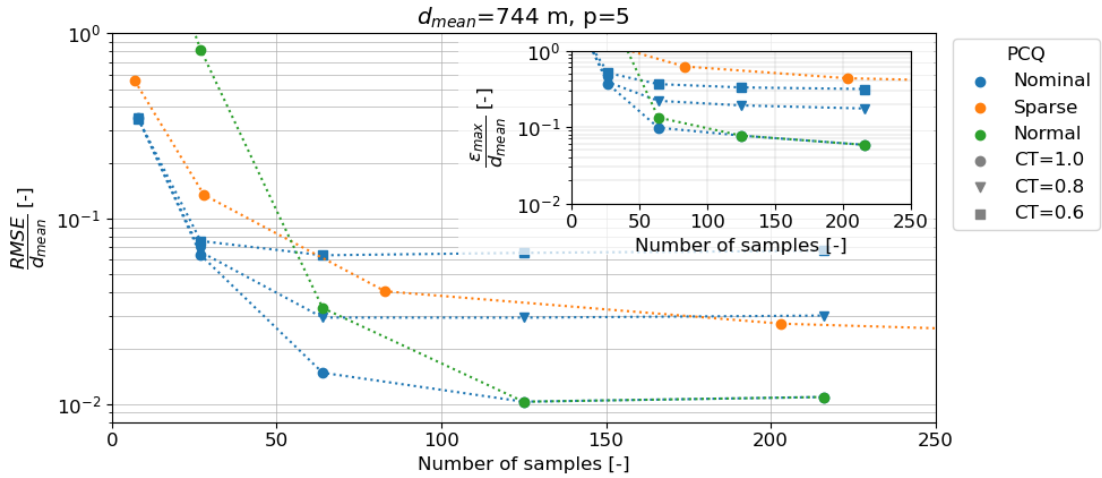

Figure C.6: NIPC performance for different settings with Gaussian quadrature and $p = 5$ - orbit 2 - 30 days - 3 uncertainties: β and $\lambda \pm 10°$ and $T_{ast} \pm 0.01$ hr

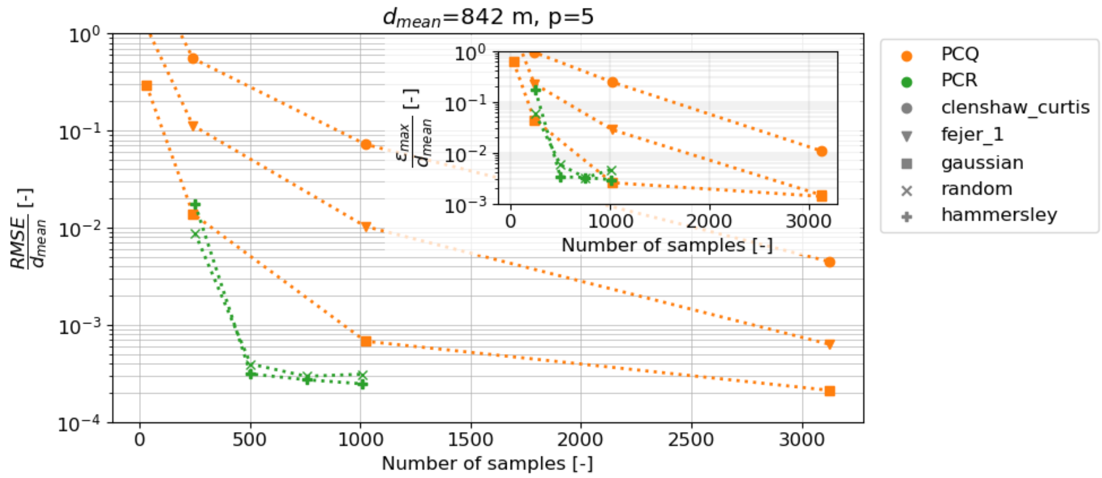

Figure C.7: NIPC performance for different quadrature rules and sampling sequences (seed = 4444) and $p = 5$ - orbit 2 - 15 days - 5 uncertainties: β and $\lambda \pm 10°$, $T_{ast} \pm 0.01$ hr and $\bar{C}_{20}$ and $\bar{C}_{22} \pm 50\%$

As shown by the differences between Figure C.7 and C.8, performance is also heavily dependent on the propagation time (15 and 30 days, respectively). With longer propagation times, trajectories have more time to disperse and more non-linearities can be encountered, requiring different NIPC settings to be optimal. Whereas 252 samples yield sufficient accuracy for the 15 day propagation, not even 1000 samples is enough for the 30 day propagation. Similarly, it is observed that PCR converges at a sample size of twice the number of polynomial coefficients (=252), whereas this is not the case for 30 days. Nonetheless, it is observed that PCR performs generally better than PCQ when the sample size is at least twice the number of polynomial coefficients, which has also been previously advised [43]. Finally, no significant differences are observed between the quasi-random sampling sequences for PCR. As such, the antithetic option, which is a variance-reduction option by mirroring samples [44], was not tested, because no improvements in terms of accuracy or efficiency are expected from it.

Similar to the previous points, the performance of Smolyak sparse grids can differ among various cases. As illustrated by Figure C.9 and C.10 (orbit 2, 30 days and orbit 1, 5 days, respectively), although the spread in the Monte Carlo ensemble is similar as indicated by the d_{mean} values, the sparse-grid approach is significantly worse than the nominal settings for orbit 2 (30 days), but more efficient for orbit 1 (5 days), considering the smaller sample sizes. This is likely due to a Smolyak sparse grid using relatively few samples in the uncertain domain's centre and more and more towards its edges and corners. When the dynamics are highly non-linear

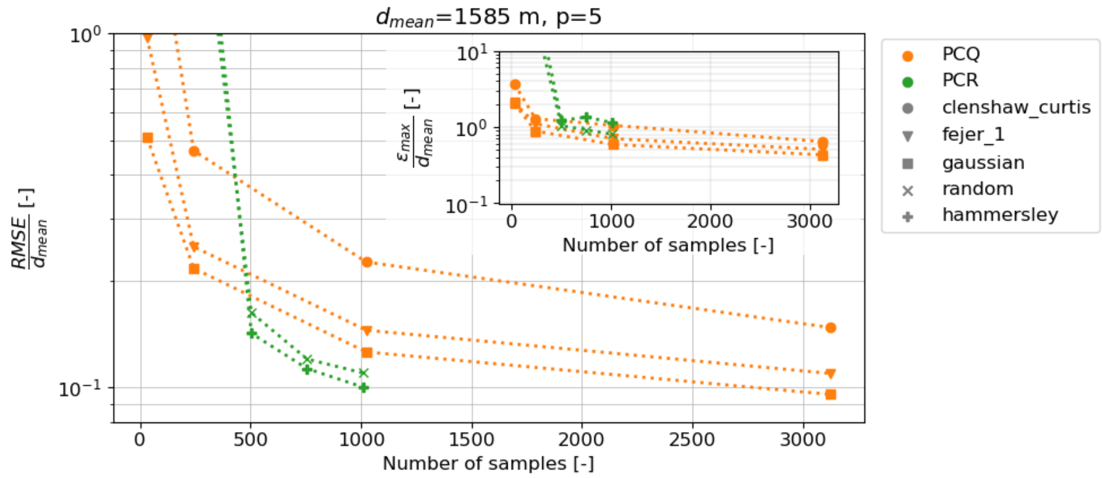

Figure C.8: NIPC performance for different quadrature rules and sampling sequences (seed = 4444) and $p = 5$ - orbit 2 - 30 days - 5 uncertainties: β and $\lambda \pm 10°$, $T_{ast} \pm 0.01$ hr and $\bar{C}_{20}$ and $\bar{C}_{22} \pm 50\%$

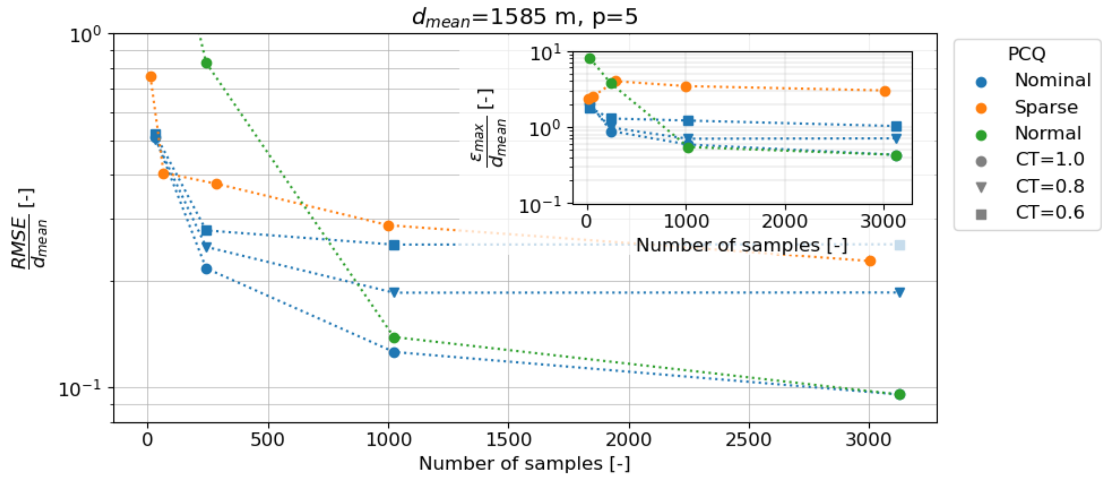

Figure C.9: NIPC performance for various settings with Gaussian quadrature and $p = 5$: orbit 2 - 30 days - 5 uncertainties: β and $\lambda \pm 10°$, $T_{ast} \pm 0.01$ hr and $\bar{C}_{20}$ and $\bar{C}_{22} \pm 50\%$

in the centre of the uncertain domain, as is the case for orbit 2 propagated for 30 days, not enough samples are used from the uncertain domain's centre to capture these non-linear dynamics completely in this region. When the dynamics are less non-linear in the centre of the domain, as is the case for orbit 1 propagated for only 5 days, these relatively few samples from the uncertain domain's centre is enough to capture the dynamics completely in this region. Apparently, this effect due to a difference in propagation time is stronger than difference in non-linearity because of the orbital altitude difference, which would dictate that orbit 1 is more non-linear than orbit 2.

For both cases described above, it is observed that using normal or cross-truncated polynomials is not advantageous, neither in terms of efficiency nor accuracy.

Eight uncertainties

The NIPC performance for two orbits over different propagation times with different polynomial orders is given in Figure C.11 for the case with eight uncertainties as analysed in the Journal paper. It is clearly observed that there is a large difference in NIPC performance between these cases. A 5th order polynomial performs worse for orbit 2 for a 30 days propagation than a 3rd order polynomial for orbit 1 for a propagation of 5 days, while the former's mean distance value is smaller. This, again, indicates the difference in non-linearity over different propagation times. In addition, it is observed that PCR outperforms PCQ in accuracy after

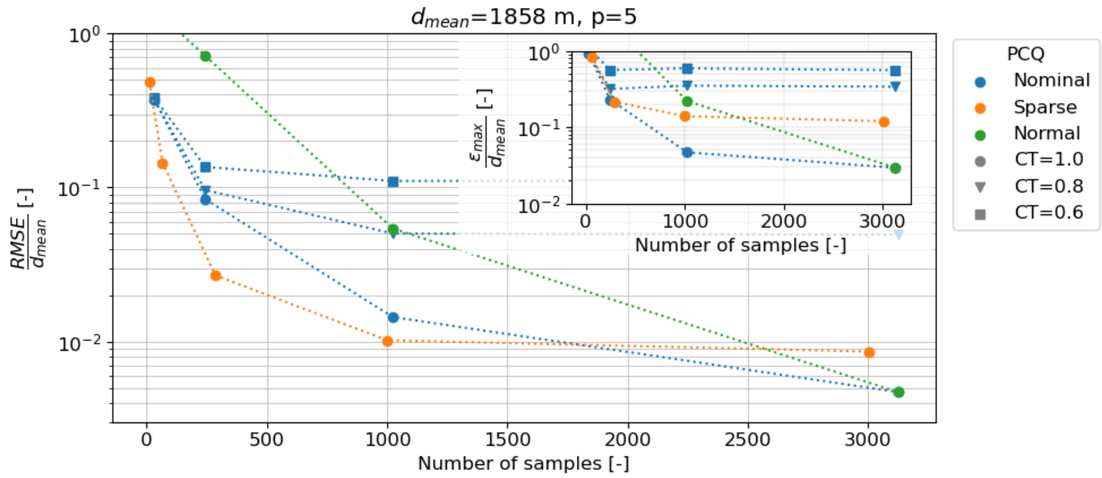

Figure C.10: NIPC performance for various settings with Gaussian quadrature and $p = 5$: orbit 1 - 5 days - 5 uncertainties: β and λ with 10°, T_{ast} ± 0.01 hr and $\bar{C}_{20}$ and $\bar{C}_{22}$ ± 50%

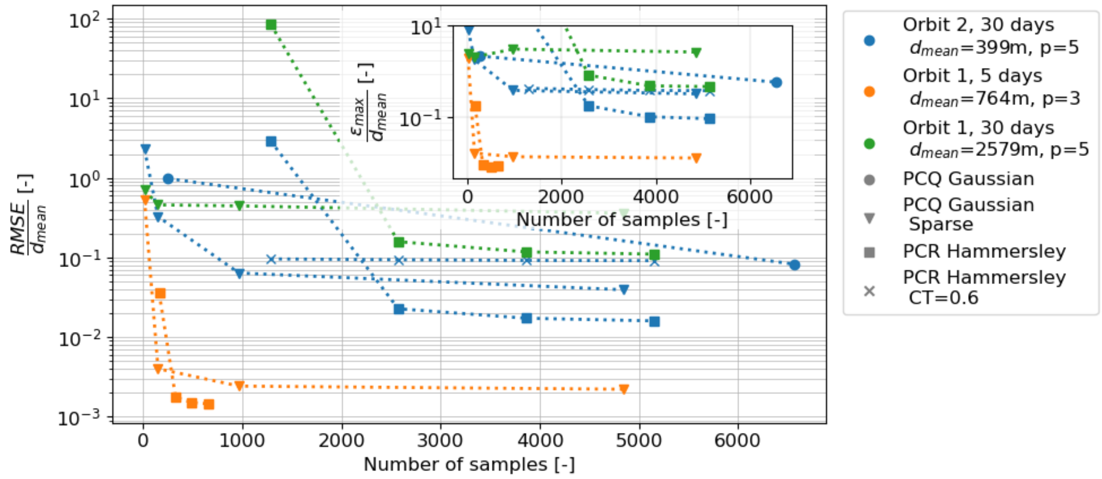

Figure C.11: NIPC performance for several orbits - 8 uncertainties: β and λ ± 0.25°, T_{ast} ± 0.00001 hr, $\bar{C}_{20}$ ± 0.005, $\bar{C}_{22}$ ± 0.003 and $\bar{C}_{21}$, $\bar{S}_{21}$ and $\bar{S}_{22}$ ± 0.0015

convergence. This happens for all cases when the number of samples is twice the number of polynomial coefficients. It is also observed that using Smolyak sparse grids is beneficial in terms of efficiency when using PCQ, looking at the results for orbit 2. Finally, it is observed that cross-truncated polynomials converge for less samples when using PCR. This is probably because the number of polynomial coefficients is smaller and thus fewer samples are required for a sufficiently over-determined system to perform the least-squares fit. Nonetheless, the achievable accuracy is lower than for non-cross-truncated polynomials.

In summary, the findings of tuning the NIPC settings are:

- $\frac{\text{RMSE}}{d_{mean}} \leq 0.01$ and $\frac{\epsilon_{max}}{d_{mean}} \leq 0.1$ yield quantitatively accurate NIPC approximations and statistical information
- PCQ converges for less samples than PSP.
- PSP converges to smaller RMSE values than PCQ, but PCQ converges to smaller ϵ_{max} values than PSP, but differences are minimal.
- The choice of quadrature rule can improve performance by a factor two in RMSE and even more in ϵ_{max}.

- The choice of quasi-random sampling sequence has no significant effect on performance.
- Using normal and cross-truncated polynomials does not improve performance for any of the studied cases.
- The performance increase with polynomial order and the number of samples or nodes is highly case-dependent. In some cases improvements can be one order of magnitude, whereas in others it may be negligible.
- PCR can outperform PCQ for five or more uncertain variables.
- Using Smolyak sparse grids can increase efficiency for five or more uncertain variables, but this is highly case-dependent.
- PCR typically converges when the number of samples is at least twice the number of polynomial coefficients, as also found in and recommended by [43].

D

Discontinuities and singularities

As mentioned in the journal paper, the Kepler elements ω, Ω and θ and the MEE true longitude L are defined within a limited range of values from 0° to 360° rad. This is problematic for the construction of the PCE, if values near these boundaries are encountered. Two types of these occurrences were encountered and the filtering of those will be elaborated upon in this chapter. The first type, described in section D.1, is when the variable does not take on particular range of values, somewhere in between 0° and 360°, throughout the uncertain domain (section D.1). The second type, described in section D.2, is when all values between 0° and 360° are encountered throughout the uncertain domain and the discontinuity is also present. Finally, section D.3 elaborates on the analysis of the discontinuities described in the journal paper, which were not possible to be filtered.

D.1. Discontinuity type I

An example of the first type of discontinuity is provided in Figure D.1. ω takes on values below 100°, as well as above 250°. The PCE is fitted also on the values in between, yielding a bad approximation. By shifting the values above 250° down by 360° and then constructing the PCE yields the results in Figure D.1b. Obviously this yields much better NIPC approximations without losing any information, because the meaning of ω shifted by 360° is exactly the same.

The filter was implemented as follows. A histogram is made of the concerning variable, ω in the above example. The histogram contains 52 bins and spans from $-\frac{2\pi}{50}$ rad (−7.2°) to $\pi + \frac{2\pi}{50}$ rad (367.2°), to guarantee that all values are properly captured. Subsequently, SciPy's[1] peak finding function within the signal module is used to search for peaks in the histogram that are at least 25 bins apart. If 1 peak is found, there is no discontinuity and the filter is skipped. If two peaks are found, this corresponds to a discontinuity that must be filtered. The peak bins and the bins without any values are then used to determine the minimum value of the concerning variable which should be shifted by 360°. All values larger than it are shifted. This algorithm was implemented for ω, Ω, θ and the true longitude L.

D.2. Discontinuity type II

In the case where the variable has a discontinuity of type I, but also covers the full range of values from 0° to 360°, as in Figure D.2a, the algorithm described above will not work. Even if it actually finds two peaks, it cannot find a minimum value for the values that must be shifted, because there are not bins with no values. This discontinuity type was therefore filtered differently. This discontinuity type was also only encountered in θ and L. It arises because, under uncertainty, the CubeSat makes a different number of full revolutions around the asteroid in the considered time. This causes all values between 0° and 360° to be encountered. The location of the jump from 0° to 360° in the uncertain domain is unpredictable and will occur in different locations for different cases.

This discontinuity type was filtered when it was encountered as follows, yielding the result shown in Figure D.2b as an example. Rather than using the converted state variable at the final time, the full time history of it is considered. When the time history jumps from 360° to 0°, the values should be shifted up by 360°.

[1] `https://scipy.org/`

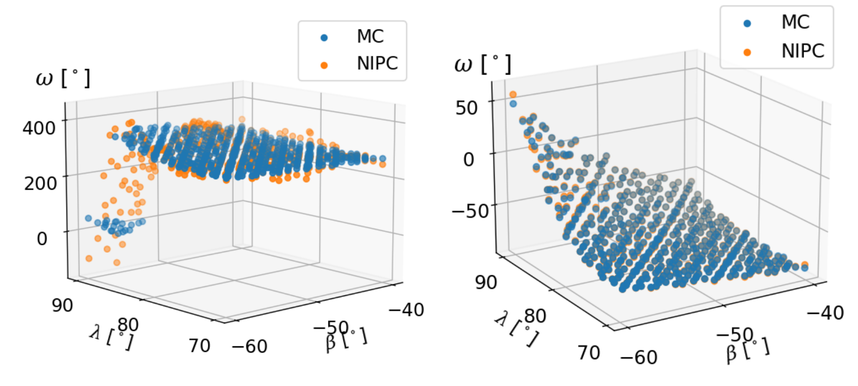

(a) Problem

(b) Verification of solution

Figure D.1: Type I discontinuity

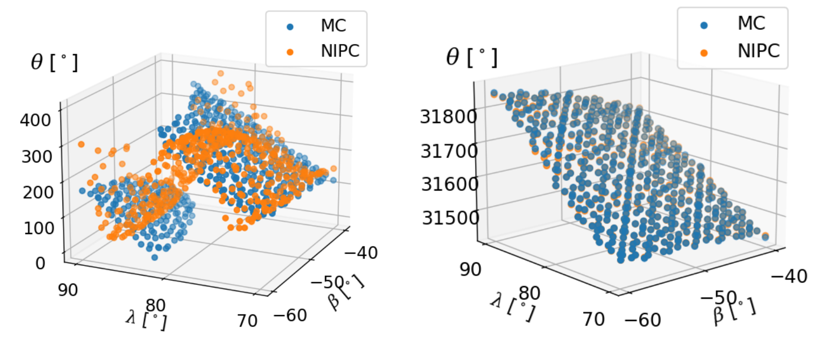

(a) Problem

(b) Verification of solution

Figure D.2: Type II discontinuity

Thus, after 1 full orbit, values above 360° should be encountered, after 2 full orbits values above 720° should be encountered, and so on. This was established by first shifting the time histories by their initial values, so that the time histories start at 0°. Subsequently, the time history is traversed from the initial to the final time. Each value is checked against the value before it. When the value is smaller than the one before it, and when the result of the multiplication of these values is also smaller than 0, this means that it crosses the zero line from positive to negative values. This indicates that a complete revolution has been fulfilled and 360° should be added to all of time history after this point. As such, the final time attains large values, which are a direct indication of the number of orbits that have been completed. For example, the case in Figure D.2b has completed between $\frac{31400}{350} = 87.2$ and $\frac{31850}{350} = 88.5$ orbits.

It is realised, that due to the high non-linearity of the dynamics, it could occur that θ and L do not increase steadily from 0° to 360°, then jump back to 0° and repeat that pattern throughout the full propagation time. It is expected, especially in the case of θ for equatorial and circular orbits (near the Kepler singularities), the time history could show more erratic behaviour. In those cases the used filter may not yield the desired result. As elaborated upon extensively in the journal paper, when they are encountered, it is advised to use MEE in these cases (including L), rather than Kepler elements. Since these cases were not encountered in this research, it has not been tested whether the described filter would still work for L and this is thus subject for future research.

D.3. Singularities in the Kepler elements

As described in the journal paper, discontinuities where encountered that could not be filtered. This section elaborates on the analysis that was performed to find the cause of these discontinuities.

As shown in Figure 13 of the journal paper, the distance d_ω and d_Ω are almost identical among different propagation times for orbit 1 and their values are large, i.e. larger than the initial semi-major axis of this orbit. This contradicts the results of Figure 6 of the journal paper. These NIPC approximations were therefore

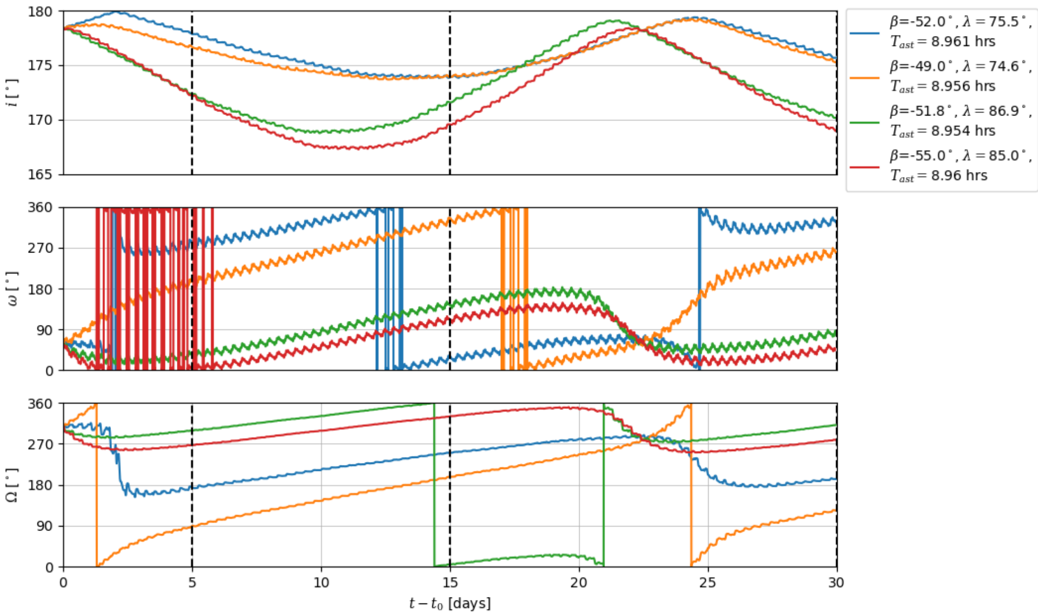

Figure D.3: Time history of ω and Ω for four cases near the discontinuities in Figure 14 of the journal paper

analysed closer, as depicted in Figure 14 of the journal paper. Here, the MC ensemble and corresponding NIPC approximations are shown as a function of two of the three uncertain parameters. T_ast was left for visualisations purposes and because it was found to have significantly less influence on the orbit than β and λ. The response-surfaces of both ω and Ω show clear discontinuities in part of the uncertainty domain. Contrary to the cases of the previous subsections, these discontinuities can not be filtered. The reason is that here the discontinuities occur only in part of the uncertain domain of one of the uncertain parameters and both variables attain values in the full range from 0° to 360°. Trying to filter these discontinuities by shifting parts of the surface by 360°, will simply shift the discontinuity to another part of the uncertain domain. In the following, this type of discontinuity will be referred to as the 'torn discontinuity', because the response looks like a plane with a tear in it.

It is remarkable that the torn discontinuities seem to arise when the inclination approaches 180°, which could be an indication that these discontinuities are observed because the trajectories approach the singularity in the Kepler elements for equatorial orbits, where Ω is undefined. As shown by the time history of i, ω and Ω in Figure D.3, this behaviour occurs because some trajectories jump from 360° to 0°, or vice versa, while others do not or at different instances in time. Consider ω for the blue and orange cases near $t - t_0 = 15$ days. The blue case jumps from 360° to 0° just before, while the orange case jumps just after this 15 day period. As shown by the red and green cases, the uncertain domain is sufficiently broad to also contain cases which do not make this jump near 15 days. Now consider Ω. Here it is the green case that makes the jump from 360° to 0° just before 15 days. While the blue and red cases do not make the jump, the orange case already makes it very early at around 2 days. Subsequently, its Ω value grows significantly to approach the blue cases' value again. Similar characteristics are observed for the 5 days and 30 day points, thereby indicating that in each of these cases these discontinuities are encountered for the same reasons. It seems that by choosing the propagation time around 22.5 days, the discontinuities may not be encountered. However, considering a full MC ensemble, it is expected that they will occur elsewhere in the uncertain domain. This is further supported by considering the behaviour of the red case below 5 days, where it shows many jumps. This sample is very close to the edge of the discontinuity for those time instance, for some being one side, for others on the other side of it. This leads to the conclusion that the location of the discontinuity in the uncertain domain is not fixed, but changes with time.

While the jumps sometimes happen when the inclination is closest to 180°, this is not strictly the case. For example, the inclination is below 175° when the blue and orange cases make the jump near 15 days. More importantly, it is observed that ω and Ω do undergo larger changes when the inclination is closest to

Table D.1: Correlations between ω, Ω and θ for various cases

	Orbit 2		**Orbit 3**	
$t - t_0$	$\rho_{\omega,\Omega}$	$\rho_{\omega,\theta}$	$\rho_{\omega,\Omega}$	$\rho_{\omega,\theta}$
5 days	-0.85	-0.98	-0.91	-0.97
15 days	-0.85	-0.98	-0.98	-1.00
30 days	-0.93	0.62	0.97	-0.9

180°. Where this immediately leads to a jump for the cases where ω or Ω are close to 0° or 360°, it does not when they lie more towards the middle of their domains. Nonetheless, this is the reason that both ω and Ω encounter a larger range of values and is therefore also the reason that the jumps are encountered. Thus, the observed discontinuities are a result of the orbit being retrograde equatorial, thereby approaching the singularity in Ω and yielding large variations in both ω and Ω.

As also shown in Figure 13 of the journal paper, the distances d_ω and d_θ show unexpectedly large values for orbit 2 and 3 after 15 days, compared to 30 days. It was explained in the journal paper that this is a result of the orbits approaching the singularity in the Kepler elements of a circular orbit. It was also explained that, because of strong correlations between ω, Ω and θ, this does not necessarily mean that the actual size of the MC ensemble, in Cartesian space, is larger. As summarised in Table D.1, strong, mostly negative, correlations were indeed encountered. Thus, a variation in one element is then accompanied by a variation in another, which can (partially) cancel the corresponding change in position. This is also the case for cases where the eccentricity is not close to zero, such as orbit 2 after 30 days (Figure 13b of the journal paper).

E

Sensitivities for different initial states and the interaction with the irregular gravity field

Section 6 of the journal paper elaborated on the stable and unstable regions in the initial state-space against rotational state uncertainties. The maximum variance among the Cartesian position elements and d_a and d_i were presented for orbits at 2500 m in Figure 18 of the journal paper. The dispersion of these uncertainties on the other Kepler elements was briefly touched upon as well, but without a detailed presentation of these results. These results are given here, in Figure E.1. It shows, that the same unstable semi-elliptical regions are found in all elements. It is also found that the maximum values of d_θ are largest. Thus, when unstable, this most pronounced in θ. The largest values of d_ω, d_Ω and d_θ are outliers and may be a result of discontinuities that were not filtered properly. In addition, these quantities show large values for equatorial orbits, which is due to the larger variation in them close to the Kepler singularities. These are thus not necessarily to be seen as more unstable regions.

Considering the stable regions, e.g. retrograde orbits, it is observed that the angular Kepler elements have larger magnitudes, in the order of 10 m, than a and e, which are in the order of 0.1-1.0 m. Thus, where unstable orbits are most unstable in θ, stable orbits are most stable in a and e.

The difference in sensitivity for different initial states, as shown in Figures 18 and 19 of the journal paper and in Figure E.1, showed that the asteroid's non-linear dynamical environment can cause unexpected results compared to theory. In an attempt to find the cause(s) for this, an analysis of the second order Sobol' indices of interactions between rotational state parameters β, λ and T_{ast} and degree 2 SH coefficients was performed, as presented in section 6.5 of the journal paper. It did not reveal any interaction terms that contributed systematically more than others. The cases 1 and 3 (referring to the highlights in Figure 18a of the journal paper) were analysed for 0.5, 0.8 and 1 day, rather than 5 days. This reduction in propagation time was required to obtain sufficient accuracy in the NIPC approximation with a 3rd order polynomial for case 3. As shown in Table E.1, these periods still show, however, the same difference in dispersion and non-linearity as in Figure 18a. Some additional remarks on the results of Figure 21 of the journal paper are made.

Firstly, it is clearly observed by the difference in the orders of magnitude, that the interactions are much

Table E.1: Standard deviations and non-linearity indices for case 1 and 3 for different propagation times (S_{p+1} is also listed for the Cartesian element with the largest standard deviation)

Case	i_0 [°]	Ω_0 [°]	$t - t_0$ [days]	max(σ_x, σ_y, σ_z) [m]	max($S_{p+1,x}$, $S_{p+1,y}$, $S_{p+1,z}$) [-]
1	179	52	0.5	96	0.021
			0.8	146	0.054
			1.0	194	0.24
3	43	144	0.5	195	4.4
			0.8	967	966
			1.0	1119	19226

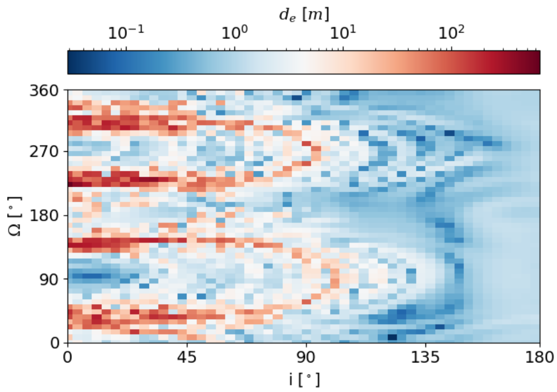

(a) Variation in eccentricity

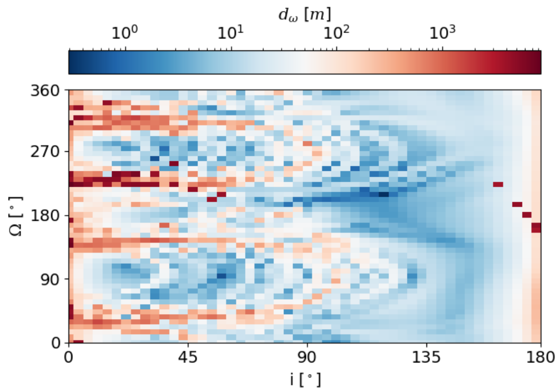

(b) Variation in argument of periapsis

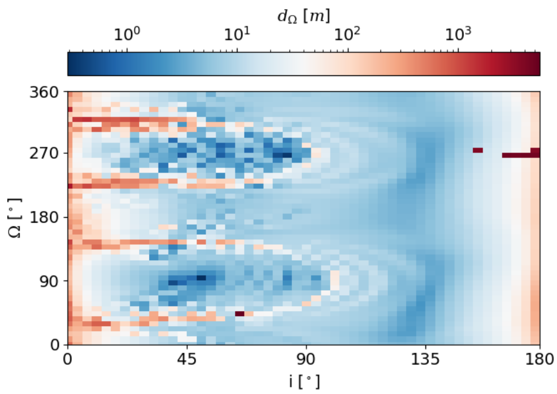

(c) Variation in right ascension of the ascending node

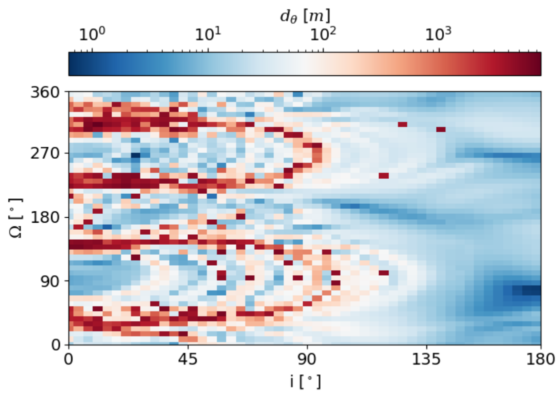

(d) Variation in true anomaly

Figure E.1: The effect of initial orbital geometry on the trajectory dispersion after 5 days due to rotational state uncertainty (β, λ and T_{ast} with post early-characterisation uncertainties)

more effective for case 3, than for case 1. Similarly, the range of values of the shown Sobol' indices is larger for case 1. This shows that for case 3, which undergoes larger dispersions and encounters higher non-linearities, all interactions have become more influential. Nonetheless, the observed orders of magnitude indicate that for both cases the first order Sobol indices and also some interactions between two SH coefficients are significant, thus making the contribution by the shown interactions relatively small.

Secondly, it is noted, that the interactions of T_{ast} with the SH coefficients are low, especially for case 1. This is in line with results that were obtained in the analysis of section 6.1 (Figure 8) of the journal paper, which showed that the rotation period T_{ast} has less influence on the trajectories than the rotation pole orientation parameters β and λ. This can be explained by the working principle of the rotation period uncertainty. This parameter does not alter the initial orientation of the asteroid with respect to the CubeSat, but merely builds up a phase lag over time. It thus requires some time during the propagation to build up its effect, so that the asteroid has a significantly different orientation than in the nominal case, which happens only after a sufficiently long time. As such, its relative contribution increases with time as well. It is remarkable to see that for case 1 the periods up to 1 day are not sufficient for that, but that for case 3, with the large non-linearity, these interactions attain similar magnitudes as those for the rotation pole orientation.

Although it cannot be deduced what the true cause(s) of the semi-elliptical regions in Figure 18 of the journal paper is, it seems that throughout the trajectories, different contributions become significant and can also become less influential later on. This is most likely to depend on what gravitational 'bulges', as caused by the different SH coefficient, the trajectories fly by closely at different times throughout the propagations. For example, trajectories that fly through the extension of the asteroid's x-axis regularly, will likely be more affected by the $\bar{C}_{22}$ term and its interactions, than those which do not. Moreover, a detailed analysis of the complete time history of the nominal orbits and the deviations from it due to the uncertainties must be performed to find the gravitational influences that are encountered at all times in the propagation. Linking these to the times at which large dispersions in the trajectories are observed can reveal which parameters cause the semi-elliptical regions in the Figure 18 of the journal paper.

It is finally noted, that the above recommended research can be aided with additional analyses including smaller uncertainties in the SH uncertainties. Currently there could be differences in the trajectory deviations corresponding to Figure 18 of the journal paper, only including rotational state uncertainties, and those analysed in this chapter, which also include significant SH coefficient uncertainties. As the trajectory deviations are different, the Sobol' indices may be, too. Ideally, these Sobol' indices would be analysed without SH coefficient uncertainties, but that is not possible, due to the definition of Sobol' indices. Therefore it could be required to use smaller uncertain magnitudes so that the trajectory deviations remain sufficiently similar and the right relative contributions are found. However, here a difficulty lies in finding the right uncertain magnitudes to guarantee this validity, and an analysis of the time history of the trajectories would be required for verification as well.

Bibliography

[1] Citi GPS: Global Perspectives and Solutions. *Space: The Dawn of a New Age*. Tech. rep. 2022. URL: www.citi.com/citigps.

[2] European Space Agency. *Compendium of Earth Observation contributions to the SDG Targets and Indicators*. 2020. DOI: 10.3389/fenvs.2022.788843.

[3] D. Hauser et al. *Satellite Remote Sensing of Surface Winds, Waves, and Currents: Where are we Now?* 2023. DOI: 10.1007/s10712-023-09771-2.

[4] A. Dolgopolov et al. "Analysis of the commercial satellite industry". In: *AIAA Space and Astronautics Forum and Exposition* (2018). DOI: 10.2514/6.2015-4435.

[5] H. W. Jones. "The Recent Large Reduction in Space Launch Cost". In: *48th International Conference on Environmental Systems*. 81. 2018.

[6] A. Shao, E. A. Koltz, and J. R. Wertz. "Quantifying the cost reduction potential for earth observation satellites". In: *12th Reinventing Space Conference* 40 (2014). DOI: 10.2514/6.2014-4260.

[7] E. Heggy et al. "Radar probing of Jovian icy moons : Understanding subsurface water and structure detectability in the JUICE and Europa missions". In: *Icarus* 285 (2017), pp. 237–251. DOI: 10.1016/j.icarus.2016.11.039.

[8] J. Rigby et al. "The Science Performance of JWST as Characterized in Commissioning". In: 135 (2023). DOI: 10.1088/1538-3873/acb293.

[9] D. Hestroffer et al. "Small Solar System Bodies as granular media". In: *Astronomy and Astrophysics Review* 27.1 (2019). ISSN: 09354956. DOI: 10.1007/s00159-019-0117-5.

[10] W. F. Bottke et al. "An Overview of the Asteroids:" in: *Asteroids III* (2002), pp. 3–15. DOI: 10.2307/j.ctv1v7zdn4.7.

[11] F. E. Demeo and B. Carry. "Solar System evolution from compositional mapping of the asteroid belt". In: *Nature* 505 (2014), pp. 629–634. DOI: 10.1038/nature12908.

[12] A. Morbidelli et al. "Chaotic capture of Jupiter's Trojan asteroids in the early Solar System". In: *Nature* 435.7041 (2005), pp. 462–465. ISSN: 00280836. DOI: 10.1038/nature03540.

[13] T. Hoffman et al. "Near-Earth Object Surveyor Overview". In: *IEEE Aerospace Conference Proceedings* (2022), pp. 1–16. DOI: 10.1109/AERO53065.2022.9843508.

[14] A. S. Rivkin and A. F. Cheng. "Planetary defense with the Double Asteroid Redirection Test (DART) mission and prospects". In: *Nature Communications* 14.1003 (2023). DOI: 10.1038/s41467-022-35561-2.

[15] T. Swindle et al. "Small bodies exploration in the next 35 years." In: *Lunar and Planetary Institute Contributions - Planetary Science Vision 2050 Workshop* 1989 (2017).

[16] M. A. Barucci, E. Dotto, and A. C. Levasseur-Regourd. "Space missions to small bodies: Asteroids and cometary nuclei". In: *Astronomy and Astrophysics Review* 19.48 (2011). DOI: 10.1007/s00159-011-0048-2.

[17] J. K. Miller et al. "Determination of Shape, Gravity, and Rotational State of Asteroid 433 Eros". In: *Icarus* 155 (Jan. 2002), pp. 3–17. DOI: 10.1006/ICAR.2001.6753.

[18] C. Lhotka et al. "Gravity field and solar component of the precession rate and nutation coefficients of Comet 67P/Churyumov–Gerasimenko". In: *Monthly Notices of the Royal Astronomical Society* 455.4 (Feb. 2016), pp. 3588–3596. DOI: 10.1093/MNRAS/STV2521.

[19] D. S. Lauretta et al. "OSIRIS-REx: Sample Return from Asteroid (101955) Bennu". In: *Space Science Reviews* 212 (2017), pp. 925–984. DOI: 10.1007/s11214-017-0405-1.

[20] A. F. Cheng et al. "AIDA DART asteroid deflection test: Planetary defense and science objectives". In: *Planetary and Space Science* 157 (2018), pp. 104–115. DOI: 10.1016/j.pss.2018.02.015.

[21] C. J. Benson et al. “Spin state evolution of (99942) Apophis during its 2029 Earth encounter”. In: *Icarus* 390.115324 (2023). DOI: 10.1016/j.icarus.2022.115324.

[22] G. Madeira, S. Charnoz, and R. Hyodo. “Dynamical origin of Dimorphos from fast spinning Didymos”. In: *Icarus* 394.115428 (2023). DOI: 10.1016/j.icarus.2023.115428.

[23] M. T. Zuber et al. “The Psyche Gravity Investigation”. In: *Space Science Reviews* 218.57 (2022). DOI: 10.1007/s11214-022-00905-3.

[24] D. J. Scheeres. *Orbital Motion in Strongly Perturbed Environments.* 2012. DOI: 10.1007/978-3-642-03256-1.

[25] S. Takahashi and D. J. Scheeres. “Higher-Order Corrections for Frozen Terminator Orbit Design”. In: *Journal of Guidance, Control, and Dynamics* 43.9 (2020), pp. 1642–1655.

[26] J. Feng and X. Hou. “The semi-analytical analysis of orbital evolution around an asteroid under the effects of the C20 term, the solar radiation pressure and the asteroid’s orbital eccentricity”. In: *Advances in Space Research* 62.9 (Nov. 2018), pp. 2649–2664. DOI: 10.1016/J.ASR.2018.07.028.

[27] J. Feng et al. “Modeling and analysis of periodic orbits around a contact binary asteroid”. In: *Astrophysics and Space Science* 357.124 (June 2015). DOI: 10.1007/S10509-015-2353-0/TABLES/3.

[28] J. Feng et al. “Sensitivity analysis of the orbital motion around 469219 Kamo’oalewa (2016 HO3) to uncertainties on asteroid mass and solar radiation pressure”. In: *Advances in Space Research* 69.3 (Feb. 2022), pp. 1602–1618. DOI: 10.1016/J.ASR.2021.11.035.

[29] J. C. Melman, E. Mooij, and R. Noomen. “State propagation in an uncertain asteroid gravity field”. In: *Acta Astronautica* 91 (Oct. 2013), pp. 8–19. DOI: 10.1016/J.ACTAASTRO.2013.04.027.

[30] J. Feng et al. “Dynamical structure of the motion around asteroids with uncertain gravity and solar radiation pressure”. In: *Acta Astronautica* 186 (2021), pp. 135–147. DOI: 10.1016/j.actaastro.2021.05.023.

[31] I. Fodde, J. Feng, and M. Vasile. “Uncertainty maps for motion around binary asteroids”. In: *Celestial Mechanics and Dynamical Astronomy* 134.41 (2022). DOI: 10.1007/s10569-022-10096-2.

[32] P. Maybeck. *Stochastics Models, Estimation and Control.* Academic Press, New York, 1982.

[33] R. Armellin et al. “Asteroid close encounters characterization using differential algebra: the case of Apophis”. In: *Celestial Mechanics and Dynamical Astronomy 2010 107:4* 107 (June 2010), pp. 451–470. DOI: 10.1007/S10569-010-9283-5.

[34] S. Julier, J. Uhlmann, and H. Durrant-Whyte. “A new method for the nonlinear transformation of means and covariances in filters and estimators”. In: *IEEE Transactions on Automatic Control* 45.3 (2000), pp. 477–482. DOI: 10.1109/TAC.2002.800742.

[35] R. S. Park and D. J. Scheeres. “Nonlinear Mapping of Gaussian Statistics: Theory and Applications to Spacecraft Trajectory Design”. In: *Journal of Guidance, Control, and Dynamics* 29.6 (May 2006), pp. 1367–1375. DOI: 10.2514/1.20177.

[36] N. Wiener. “The Homogeneous Chaos”. In: *American Journal of Mathematics* 60.4 (Oct. 1938), p. 897. DOI: 10.2307/2371268.

[37] S. P. Naidu et al. “Radar imaging and physical characterization of near-Earth Asteroid (162421) 2000 ET70”. In: *Icarus* 226.1 (2013), pp. 323–335. DOI: 10.1016/j.icarus.2013.05.025.

[38] F. Ferrari et al. “Trajectory Options for Hera’s Milani CubeSat Around (65803) Didymos”. In: *Journal of the Astronautical Sciences* 68 (2021), pp. 973–994. DOI: 10.1007/s40295-021-00282-z.

[39] A. Poghosyan and A. Golkar. “CubeSat evolution: Analyzing CubeSat capabilities for conducting science missions”. In: *Progress in Aerospace Sciences* 88 (Jan. 2017), pp. 59–83. DOI: 10.1016/J.PAEROSCI.2016.11.002.

[40] A. Kaluthantrige et al. “Centroid regression using CNN-based Image Processing Algorithm with application to a binary asteroid system”. In: *Congress on Evolutionary Computation.* IEEE, 2022.

[41] G. Balmino. “Gravitational Potential Harmonics from the Shape of an Homogenous Body”. In: *Celestial Mechanics & Dynamical Astronomy* 60.3 (1994), pp. 331–364. DOI: 10.1007/BF00691901.

[42] S. Le Maistre, A. Rivoldini, and P. Rosenblatt. “Signature of Phobos’ interior structure in its gravity field and libration”. In: *Icarus* 321.June 2018 (2019), pp. 272–290. ISSN: 10902643. DOI: 10.1016/j.icarus.2018.11.022. URL: https://doi.org/10.1016/j.icarus.2018.11.022.

[43] S. Hosder, R. W. Walters, and M. Balch. “Efficient sampling for non-intrusive polynomial chaos applications with multiple uncertain input variables”. In: *15th Structures, Structural Dynamics and Materials Conference* (2007). DOI: 10.2514/6.2007-1939.

[44] J. Feinberg and H. P. Langtangen. “Chaospy: An open source tool for designing methods of uncertainty quantification”. In: *Journal of Computational Science* 11 (2015), pp. 46–57. ISSN: 18777503. DOI: 10.1016/j.jocs.2015.08.008.